AN ELECTROCHEMICAL IMPEDANCE SPECTROSCOPY AND PSEUDO STEADY STATE VOLTAMMETRIC STUDY OF THE CHLORIDE-SUPPRESSOR COMPLEX FORMED ON THE COPPER SURFACE IN PLATING BATHS THAT EXHIBIT SUPERFILLING USED IN THE DUAL DAMASCENE PROCESS DURING THE COPPER METALLIZATION OF SEMICONDUCTORS

by

John Gardner Long III

A dissertation submitted to Johns Hopkins University in conformity
with the requirements for the degree of Doctor of Philosophy

Baltimore, Maryland
March 2015

Abstract

Copper has become a key material in semiconductors due to its use as the interconnect material in silicon-based integrated circuits. Electrochemical deposition has shown itself to be a very capable technique to deposit copper in small features without leaving voids or holes. However, the electrochemistry of the additives used in the plating bath are less-well understood than they should be.

In this work, the behavior of the suppressor is investigated, and shown to have a well-defined potential at which it ceases suppressing copper deposition. Electrochemical impedance spectroscopy is used in conjunction with cyclic voltammetric measurements to show this cessation of suppression is concurrent with the desorption of a complex formed by the suppressor from the copper surface.

Pseudo steady-state voltammetry is shown to be a superior technique for determining the critical potential at which the complex desorbs due to its increased sensitivity and lack of requirement for significant analysis of impedance data. This desorption reaction is studied over a range of different bath chemistries and the concentration dependence is determined for various solution additives. From these dependencies, a model is constructed for the likely composition of the suppressor complex that is adsorbed to the copper surface during deposition.

In addition, rotating ring-disk experiments are conducted to investigate the role of copper(I) in the presence of a common solution accelerator, SPS. SPS is shown to increase the concentration of the cuprous species, an increase that is shown to be countered by the presence of dissolved oxygen in the solution. This result provides additional evidence for the role in cuprous ions in copper plating.

Advisor: Professor Peter C. Searson

Reader: Professor Robert C. Cammarata

Dedication

This work is dedicated to Marge Weaver, whom I consider the most effective departmental administrator in the history of Johns Hopkins University. Marge was there when I began my studies as an undergraduate in the Materials Science & Engineering Department more than twenty years ago, and proved particularly adept over the intervening years in keeping me in the good graces of the University and the Whiting School of Engineering. I'm not sure if I hold the Johns Hopkins University record for longest recorded time from start to finish of a PhD, but I can't imagine there are more than a handful of students who were able to dawdle more than I.

Throughout all this time, including more than eight years in the Marine Corps and my year and a half in Oxford, Marge fought the battle with the University Administration of keeping me in some sort of student status. I don't know how many favors she called in, administrators she bribed or provosts she blackmailed, but by hook or by crook, she kept them from dis-enrolling me. At one point, I promised her that I would be done before she retired. It was a promise I was ultimately unable to keep, as she rode off to a well-deserved retirement a few months ago.

Without her Herculean efforts over the years on my behalf, I would not be in the position I am now: finishing my PhD. For that she has my eternal thanks and gratitude.

Marge, Thank You.

Acknowledgements

This work took slightly longer to produce than I (or, I think, anyone) had originally intended. I want to thank Professor Peter Searson for his seemingly infinite patience in advising me and his willingness to support its conclusion many years after he should have given up on it. To Drs. Gerko Oskam and Philippe Vereecken—two exceedingly talented researchers who were saddled with the unenviable task of attempting to teach me all they knew about electrochemistry—I offer my heartfelt thanks. Having started in the Searson Lab as a very ignorant 19-year old, I must have forced them to suffer through more than a million questions from me during our time working together.

To my fellow graduate students, and indeed all the members of Johns Hopkins who helped me over the years, thank you. Your expertise in fields ranging from Chemistry to Physics, Metallurgy to Electrical Engineering (and occasionally Materials Science) compensated for my ignorance on multiple occasions and was a significant factor in contributing to this work.

The same can be said for all those at IBM who ensured I had the opportunity to further my studies and conduct meaningful, relevant research. Especially the late Dr. Panos Andricacos, who remains an inspiration to all who work in this field.

And of course my parents, John and Virginia, without whose never-ending support I would not have been able to complete this journey.

This work is filled with many good ideas, shrewd analysis, and insightful conclusions; a few mistakes are sprinkled in for good measure. It should come as no surprise that the majority of the good stuff came from my colleagues and collaborators; the errors are of course, all mine.

Table of Contents

List of Tables

List of Figures

0.22 V (vs. SCE). Rotation rates of 1000 (□) and 0 (○) rpm are shown. The fit of a simple Randles circuit is shown (**solid magenta line**), as is a linear extrapolation of the impedance response at low frequencies (**solid blue line**). (Pg 65)

Figure 4.1: Current-potential curves in MA solution containing 25 mL L^{-1} suppressor and chloride ion concentrations of 50 (**black**), 30 (**red**), 15 (**blue**), 10 (**green**), and 5 (**magenta**) ppm. Scan rate = 0.5 mV s^{-1}. (Pg 68)

Figure 4.2a: Re-plot of Figure 4.1 with the potential corrected for the *IR*-drop. Vereecken potentials were determined by using the negative most potential reached, as indicated on the chart. Curves are for the MA solution containing 25 mL L^{-1} suppressor and chloride ion concentrations of 50 (**black**), 30 (**red**), 15 (**blue**), 10 (**green**), and 5 (**magenta**) ppm. Scan rate = 0.5 mV s^{-1}. (Pg 69)

Figure 4.2b: Zoomed in portion of Figure 4.2a to give a better view of the determined of the Vereecken potentials for the lower chloride ion concentrations. Curves are for the MA solution containing 25 mL L^{-1} suppressor and chloride ion concentrations of 50 (**black**), 30 (**red**), 15 (**blue**), 10 (**green**), and 5 (**magenta**) ppm. Scan rate = 0.5 mV s^{-1}. (Pg 69)

Figure 4.3: Plot of the Vereecken potentials as a function of chloride ion concentration for the HA (○●), MA (□■) and LA solutions (△▲). The values were obtained from EIS (solid markers) and PSSV (open markers) measurements. (Pg 70)

Figure 4.4: Plot of the Vereecken potentials as a function of suppressor concentration in the LA solution for chloride ion concentrations of 50 (●), 30 (■), 15 (▲), 10 (▼), 5 (◄), 3 (○), 1.5 (□), and 1 (△) ppm. The solid lines are the least squares fits for those concentrations; the dashed lines only show the trend for that concentration by connecting adjacent points. (Pg 71)

Chapter 1

Not long after the demonstration of the first semiconductor-based transistor (Figure 1.1) by John Bardeen, Walter Brattain and William Shockley at Bell Labs [1-3], Gordon Moore, one of the founders of Intel, famously quipped that the number of transistors on a chip quadrupled every three years (Figure 1.2), a remark that has popularly come to be known as Moore's Law. Other than a slight decrease to a doubling in transistor density every 2 years, this observation has held, placing heavy demands on scientists and engineers to constantly develop new materials and processing techniques to ensure that each successive generation of chips remained on this path.

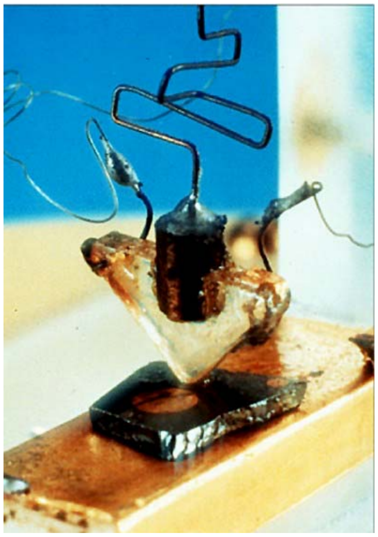

Figure 1.1: The world's first transistor.

One of the major transitions that the semiconductor industry has experienced in the last decade is the shift in on-chip metallization from aluminum to copper. Copper has a number of advantages over aluminum, among them a greater resistance to electromigration, higher conductivity (1.67 Ω cm for Cu vs. 3.0 Ω cm for Al), and greater scalability [4-6]; most importantly, it has been shown to have an electromigration lifetime up to 100 times greater than Al at similar current densities [5, 7]. But the introduction of copper was hindered by the lack of a suitable diffusion barrier. Copper readily diffuses into silicon and silicon dioxide lattices, forming copper silicides which destroy the

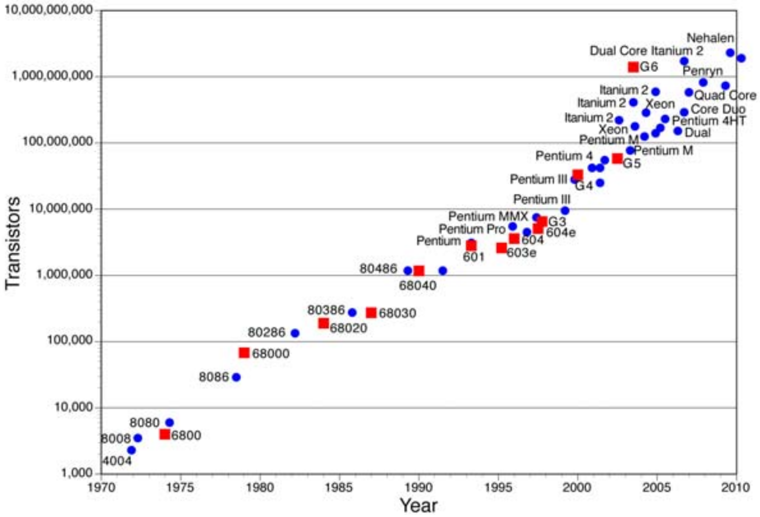

Figure 1.2: Number of transistors on typical semiconductors over time.

semiconducting properties of the silicon [4, 5]; it is therefore necessary to maintain a physical barrier between the copper and silicon.

For a material to serve as an effective diffusion barrier, it must be immiscible with copper and must prevent copper from diffusing along grain boundaries. The material must also maintain this separation at the elevated temperatures encountered during wafer processing. Recently, a number of refractory materials were shown to be suitable candidates, among them Ta, Ti, W, Ru, Ir and their nitrides and carbides [4, 8-11]. Furthermore, unlike aluminum, copper does not form an impermeable native oxide. This makes copper more prone to corrosion, and can lead to adhesion problems with the diffusion barrier. However, this gives the unique advantage in that very low contact resistances can be achieved.

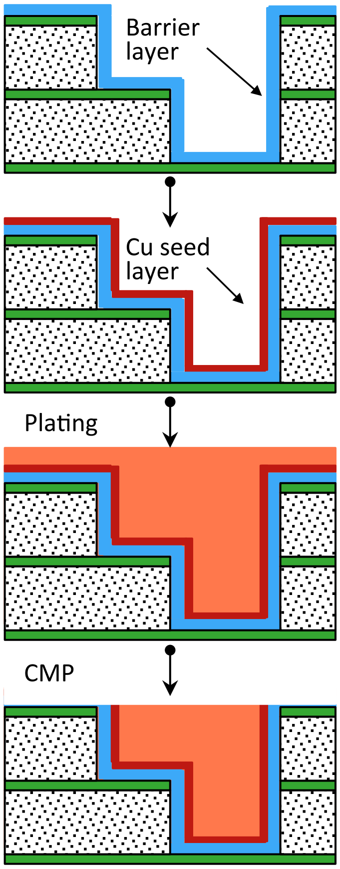

Figure 1.3: Steps for copper metallization. (1) Deposit barrier layer, (2) Deposit copper seed layer, (3) Electrochemically fill trench, (4) Remove excess deposit by CMP.

With the development of a suitable diffusion barrier, and its incorporation into the wafer manufacturing process, vacuum deposited Al gave way to electrochemically deposited Cu. It was shown [4, 5] that not only would it be possible to deposit copper electrochemically but that electrochemical deposition (ECD) is more advantageous than the physical vapor deposition (PVD) process it replaces; it does not require expensive vacuum systems, it has a high deposition rate, and it requires fewer processing steps. In addition, electrodeposited copper has been shown to experience room temperature annealing, whereby the grain size continues to increase for a period of 9 - 100 h after deposition, leading to a 25% decrease in sheet resistance [7, 12, 13]. Also, the lower percentage of (111) grains relative to (100) grains of electrodeposited copper make these films less prone to electromigration [14, 15]. All of these factors contributed to the introduction of copper plating to the wafer manufacturing process.

Copper was, and is currently, deposited electrochemically by what has become known as the dual damascene process [5, 6]. Trenches and vias are patterned using standard lithographic techniques before the addition of a copper seed layer by chemical vapor deposition (CVD) as shown in Figure 1.3. The seed layer has two purposes: it eliminates the difficult issue of the nucleation and growth of the metal on the barrier layer [16-23] and it helps compensate for the terminal effect, a non-uniformity in the potential drop across the surface of the wafer due to an IR-drop. Copper deposition on barrier layers typically proceeds through Volmer-Weber island growth, followed by coalescence. The thickness of the film at coalescence is directly dependent on the nucleus density. To form a film of thickness comparable to the feature sizes requires a very high nucleation density, which has proven difficult with standard electrochemical methods [24]. Deposition of copper on copper has proven far more effective.

During plating in a typical industrial cell, the working electrode is sufficiently thin that the potential at the surface of the wafer will vary depending on where the point is located. The variation in applied potential leads to a plating rate that is highest near the edge of the wafer where the electrical contact is made and that decreases with increasing distance from the contact. This IR-drop arises because the diffusion barrier is so thin; the CVD Cu increases the combined thickness of the conductor (the diffusion barrier plus seed layer) thereby increasing its conductivity and decreasing the IR-drop.

The wafer with the seed layer is placed in the plating solution and copper is deposited over the entire seed layer. The additives in the copper plating solution give rise to bottom-up filling, or “superfilling”, which ensures that the trenches are entirely filled and defect free. After plating, the excess deposit is removed by chemical mechanical polishing (CMP), and further processing steps ensue. Using this technique, multiple layers can be built in the structure.

The key to the plating process is to ensure that the trenches and vias are completely filled. In simple terms, this is achieved when the plating rate at the bottom of the trench is higher than on the sidewalls or at the top; the system must give rise to differential plating rates. Figure 1.4 shows different possible outcomes as a result of plating. In the case when the plating rates are all similar, the deposit will form an undesirable seam down the middle of the trench, degrading device performance. In the more extreme case in which the plating rate at the top of the trench exceeds that at the bottom, the deposit will tend to pinch off at the top, leaving a void in the trench, significantly impacting the current carrying ability of the line. Both of these results are undesirable. Device manufactures would like a system that ensures that trench filling is complete. Current plating baths achieve this, as they give rise to a phenomenon known as superfilling. Superfilling is the situation in which the trench is filled from the bottom up; plating rates on the top and sidewalls of the trench are much lower than at the bottom. Superfilling leads to a characteristic bump formation directly over the trench, the result of the acceleration of deposition in the trench.

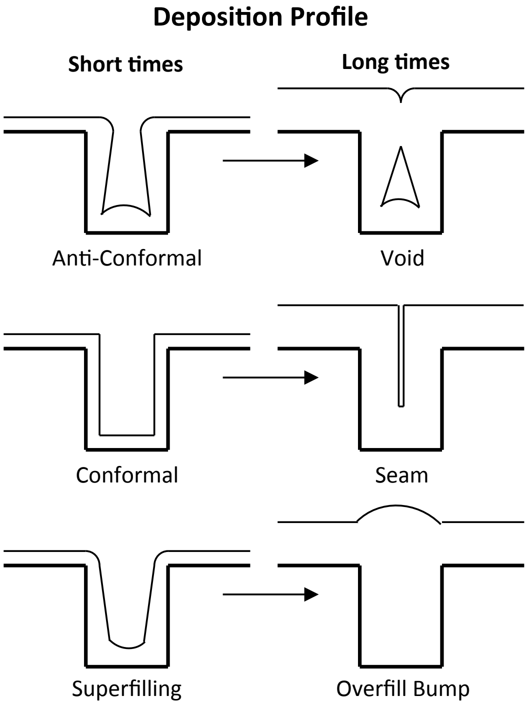

Figure 1.4: Various deposition profiles for the filling of a trench or via.

The copper plating solution currently employed by the semiconductor industry consists of an acidified copper sulfate solution containing small amounts of organic additives, though other solutions have shown promise, e.g. citrate based ones [25]. It is these additives that are responsible for the superfilling effect. Typically, the additives in the solution are chloride ions and three organic additives generally referred to by their function in the solution, a suppressor, a leveler, and an accelerator, though other combinations have been investigated [26]. As its name would imply, the leveler, typically a nitrogen containing aromatic, e.g. Janus Green B (JGB), 1*H*-Benzotriazole (BTA), or thiourea, helps to ensure that the deposit is of uniform thickness over the entire wafer, specifically in the field region, the name used to refer to the top area of the wafer between the trenches and vias [27]. Somewhat predictably, the suppressor tends to suppress, or inhibit, the deposition of copper, a property that is usually only seen in the presence of chloride ions. The suppressor is typically a large, glycol-like molecule, although the exact composition and structure are proprietary and vary by manufacturer. Polyethylene glycol (PEG) and polypropylene glycol (PPG) are known to behave in a similar manner and are commonly employed in studies published in the literature. The final additive is the accelerator, which has the effect of accelerating copper deposition in the plating bath. It is typically a sulfur containing (mercapto), short chain alkane. The closely related 3-mercapto-1-propanesulfonate (MPSA) and bis (3-sulfopropyl) disulfide (SPS) are commonly employed in plating baths for this purpose. It is important to note that the term accelerator only applies to this additive when used in conjunction with the other additives of this plating system [28, 29]. When only MPSA or SPS are added to an acidified copper sulfate plating solution, no significant increase in plating rate is observed relative to a solution without the additive (see Figure 2.1). However, when added to a solution whose plating rate is suppressed, the accelerator leads to a significant increase in plating rate (see Figure 2.2).

Superfilling has been demonstrated in solutions in the absence of a leveler. Because of this, it is likely that the superfilling mechanism depends only weakly, if at all, on the leveler. It is the competition between acceleration and suppression at various points along the trench profile that gives rise to the differential plating rates that cause superfilling. When a copper surface is brought into contact with a solution containing the accelerator and the suppressor, the accelerator and the suppressor (through a reaction mediated by chloride ions) will adsorb to the surface [30]. To better understand the mechanism, it is helpful to look at the two in isolation.

When the copper surface comes into contact with a solution containing only the accelerator, the SPS will chemisorb, forming a thiolate bond with the copper surface. It is also known that SPS can dissociate and forms an equilibrium with MPSA [31]:

$$\mathrm{SPS} + 2\mathrm{H}^{+} + 2e^{-} \leftrightarrow 2\mathrm{MPSA} \tag{1.1}$$

This process can be catalyzed by copper ions in solution [32]. For copper surfaces that have been in contact with solutions containing SPS, *ex situ* X-ray Photoelectron Spectroscopy (XPS) shows the sulfur to be present in the form of a thiolate bond to the copper surface; there is no evidence of adsorption in the dithiol state. Thus the SPS dissociatively adsorbs forming two MPSA molecules. This is further evidenced by the observation that solutions containing SPS behave nearly identically to those containing MPSA at twice the concentration [33-35]. The thiolate bond formed from this process is relatively strong, but the overall adsorption proceeds slowly.

The adsorption process in a solution containing the suppressor is slightly more complex. It has been shown that the suppressor only adsorbs strongly to the copper surface in the presence of chloride ions. In the absence of chloride ions, the suppressor adsorbs only weakly, and there is only mild inhibition of copper deposition [30]. The exact nature of this surface complex is not known, although a number of hypotheses have been put forward to explain it. The most likely mechanism is that the suppressor forms a complex with the chloride, and it is the chloride that is able to adsorb to the copper through the formation of a surface complex with the copper; it is this suppressor-chloride complex that inhibits deposition [32, 36, 37]. For this work, in the presence of chloride, mention of suppressor adsorption will imply the adsorption of this complex. In contrast to the accelerator, adsorption of the suppressor complex is quite rapid [30], although the complex seems to be less strongly adsorbed than the accelerator.

The difference in binding energy and adsorption kinetics of the accelerator and the suppressor complex gives rise to a strong transitory effect [30]. When a copper surface is initially brought into contact with a solution containing both suppressor and accelerator, it will have a high coverage of the suppressor-chloride complex, with very little accelerator [38]. However, over time this complex is slowly displaced by the accelerator. This mechanism will occur both under plating conditions and in the absence of an applied potential.

An important property of these additives is that they remain at the metal/electrolyte interface, even during growth of the metal surface, i.e. plating. In this respect, they “float” on the copper surface. It is also interesting to note that, unlike leveler dominated systems [32, 39, 40], almost none of the additives seem to be incorporated into the deposit [6, 41, 42]. Secondary Ion Mass Spectroscopy (SIMS) of deposited copper shows it to contain only trace amounts of the atoms that compose the additives [43]. The low impurity level is a significant advantage as it gives rise to higher conductivity copper, improving device performance.

During plating, the relative surface concentrations of the suppressor and accelerator will determine the plating rate at that location [30]. As the accelerator replaces the suppressor, the copper deposition rate will increase locally. Areas of the surface that are high in accelerator concentration will have higher plating rates than those that are covered predominantly by the suppressor. Typically, a plating current of 10 - 15 mA cm^{-1} is used. At this rate, the suppressor complex remains adsorbed to the surface [36, 37].

For deposition on a planar substrate, no change in surface concentration due to a change in surface area will occur. Therefore the study of these multi-component baths on flat wafers may give misleading results as to how they will interact in trenches and vias. For reasons discussed below, deposits on initially planar substrates from baths that contain these additives will tend to be smooth and of uniform height. However, deposition into trenches and vias gives rise to some interesting phenomena. As can be seen from Figure 1.5, the surface area of a trench exposed to the plating solution is drastically reduced during filling. Because the plating additives remain on the surface, the decrease in surface area as a result of plating will lead directly to an increase in the adsorbate concentration. If the surface was initially near the point of saturation, the decrease in area will cause a supersaturation at the surface, leading to desorption of some of the additives. In this desorption process, the most weakly bound additive to the surface will be desorbed.

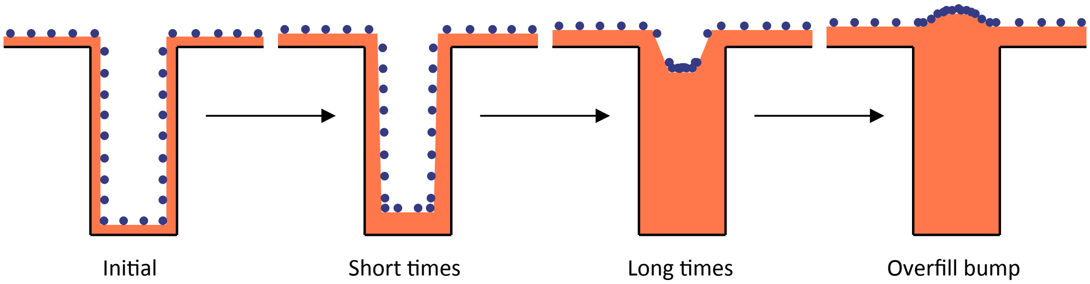

Figure 1.5: Curvature Enhanced Accelerator Coverage Model of trench filling.

The thiolate bond formed by the accelerator is much stronger than the physisorbed suppressor complex, and it will tend to remain on the surface, displacing the suppressor. These areas will tend to have a higher concentration of accelerator (and lower suppressor concentration) compared to other areas of the surface. This relative increase in accelerator surface concentration will lead to enhanced local acceleration of copper deposition. It is evident that the decrease in surface area as a result of film growth will be most pronounced at areas of the surface that are concave, i.e. the bottom corners of the trench. This model of superfilling has been termed the "curvature-enhanced accelerator coverage" mechanism (CEAC) and is well documented in the literature [44-49].

It is also interesting to note that the deposition rate at convex surfaces, i.e. the tops of the trenches, will be appreciably slower than that of a planar surface. In this case, an increase in volume of the deposit will lead to an increase in surface area. Since adsorption of the suppressor is more rapid than that of the accelerator, the surface concentration of accelerator will actually decrease as more suppressor adsorbs. This effect has the benefit of rapidly slowing deposition on the trench corners, helping to prevent pinch-off during deposition.

The development of plating baths that exhibit superfilling has concentrated on determining the optimal concentrations of the additives, as well as mathematical modeling of the process for the same aim. Smaller feature sizes, i.e. smaller trench widths and higher aspect ratios will require that the plating solution be optimized to an even greater extent than it currently is. Without further refinement, higher aspect ratios will cause a larger "overburden" bump to form after filling of the trench; the higher ratio of trench surface area to width will lead to a very high accelerator concentration on the copper surface above the filled trench. This large excess of accelerator increases the plating rate, leading to the formation of a large bump, which must be removed by CMP. The current CMP process used to remove the excess deposit will be unable to cope with these larger bumps. Although related to superfilling, current predictions are that this problem will be solved through enhanced use of the leveler, whose primary purpose in a three-additive bath is to minimize bump formation [32]. However, the semiconductor industry also faces additional challenges in the drive towards next-generation chip technologies with which the current generation of plating processes cannot cope [22, 50]. Further refinement of the electrochemical deposition process will be needed.

In their continual quest for ever-increasing device performance, chip designers continually rely on smaller feature sizes to achieve their aims. However, continued decrease in feature size will necessitate the elimination of the copper CVD seed layer currently used. As the trench width approaches the thickness of the seed layer, it will become increasing difficult, eventually impossible, to effectively put down a uniform seed layer of copper over the entire wafer surface. Elimination of the seed layer will have the added benefit of reducing the number of processing steps in the manufacturing process (specifically a high cost vacuum step), leading to cost and time savings. But the elimination of the seed layer brings to the fore the difficulty of plating directly on the liner material, ensuring both a continuous film and a rapid transition to the kinetics that give rise to superfilling, as well as a satisfactory solution to the problem of the terminal effect.

The shift to larger diameter wafers will also pose problems for the electroplating process. The larger wafer diameter will greatly enhance the problem of the terminal effect. As mentioned above, the terminal effect arises from the potential drop due to current flow through the cell, commonly referred to as IR-drop. The liner has a relatively high sheet resistance, so current flow to the center will have a higher IR-drop than current flow to the edge. Normally, the anode is parallel to the wafer surface, so the IR-drop across the solution will be the same. Because of the varying IR-drop across the wafer, the overpotential at various points along the surface will not be constant, i.e. the wafer will be a non-equipotential surface. Different overpotentials will give rise to different plating rates. This will make determining a plating regime for the wafer difficult.

One solution to this problem is to decrease the conductivity of the solution; this will lead to a greater IR-drop across the solution. Deposition is typically galvanostatic, and the increased resistance will lead to a higher applied potential. Because a greater share of the potential will be dropped over the solution, the relative difference in surface potentials across the liner will decrease. This method cannot completely eliminate the terminal effect, but can reduce it to manageable proportions. Decreasing solution conductivity is commonly accomplished by lowering the acid concentration of the bath and increasing the copper concentration. However, this may not be an option if changing the pH of the solution adversely affects its superfilling properties. Typically, a desirable copper deposit can only be achieved using solutions with a pH below 4, so the benefit of this technique to solve the problem of the terminal effect may be limited. The Pourbaix diagram for aqueous copper complexes (Figure 1.6) shows that metallic copper is stable when the pH is below 4 [51]. Above this point, copper oxides are more likely to form. Therefore plating solutions with pH > 4 will have difficulty producing the pure metallic copper deposit required for integrated circuits.

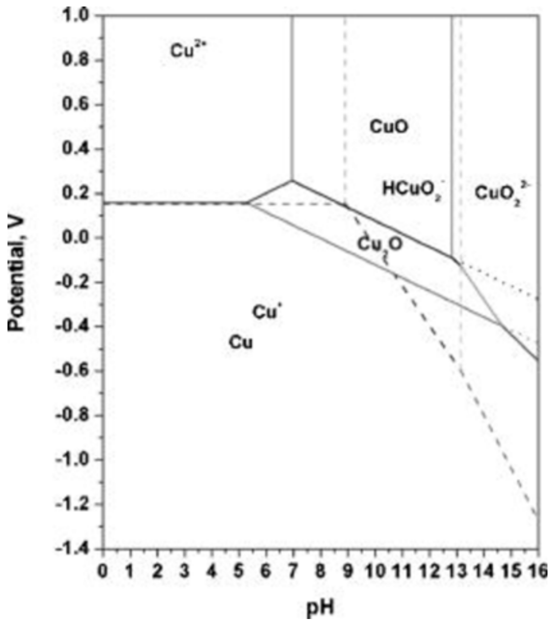

Figure 1.6: Pourbaix diagram of the aqueous copper system.

The problems of both the terminal effect and the difficulty of plating on the liner may have the same solution. Electrical contact to the wafer is made by a ring along the outside edge. Because of the high sheet resistance of the liner, in the absence of the copper seed layer, the *IR*-drop across the solution/wafer interface will be lowest along the edge near the contact. In a properly calibrated system, this potential at the outside edge of the wafer may be sufficiently negative to reduce copper and form a deposit. As the copper deposit is formed, the suppressor complex immediately adsorbs to it, preventing continued vertical growth. But the copper film will be able to conduct the deposition current to the edge of the growing copper, where the greatest potential drop with the solution will exist, as shown in Figure 1.7. Because the suppressor complex does not adsorb to the liner material, copper deposition onto the liner is not suppressed like it is onto the newly deposited copper. Further copper deposition will take place onto the liner at this point, and will continue all the way to the center of the wafer. Figure 1.8 shows a top down view of the copper deposit as it grows from the edge of the wafer inwards to the center. In this manner, a copper "seed" layer can be electrochemically formed directly on the liner.

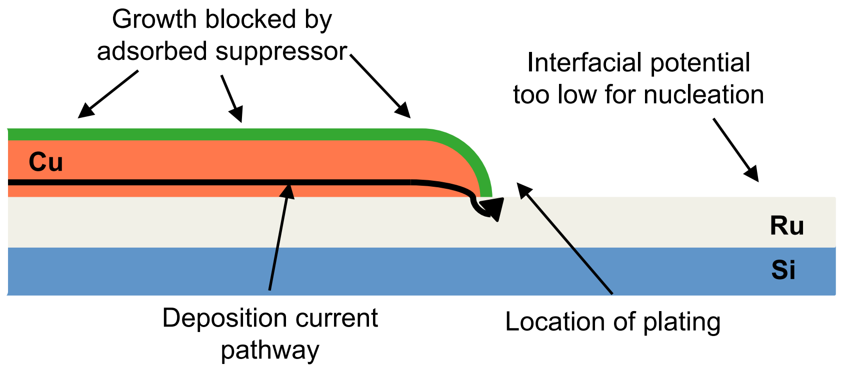

Figure 1.7: Cross sectional view of copper deposition directly onto the liner. The newly formed Cu film provides a path for the deposition current so deposition continues to occur onto the liner at the edge of the copper film.

For this process to work, a few requirements are necessary. The potential applied to the system must be large enough to reduce copper at the growing copper film interface, but not so large that the copper film grows vertically too quickly. Luckily, this problem can be solved with an effectively strong suppressor. It must adsorb rapidly on copper, inhibiting deposition, but not adsorb on the liner material, so that deposition can proceed rapidly across the liner material. A more thorough understanding of the mechanism of suppression will allow engineers to design metallization processes on increasingly smaller scales, furthering the continuation of Moore’s Law.

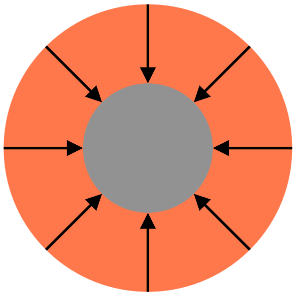

Figure 1.8: Top-down view of wafer plating showing the deposition proceeding from the wafer edge inward toward the center.

Study of the suppressor molecule is important for a number of reasons. Future increases in the effectiveness of superfilling will come either from the use of additives that display better intrinsic properties or a more accurate tailoring of the solution composition employed for plating. Currently, SPS is the best-known accelerator. Though there have been efforts to find a more powerful accelerator than SPS [52], these efforts have yet to bear fruit. It is more likely then, that advances in superfilling will come from a better understanding of the suppressor. Both a qualitative as well as quantitative understanding of the mechanism of suppression are needed. It is hoped that this can lead to not only a better suppressor but a greater ability of computer models (such as CEAC) to accurately predict the fill mechanism. More accurate computer modeling can be used to predict the optimal bath composition for smaller feature sizes.

Chapter 2

The electrodeposition of metals was for many years regarded as more art than science. Prior to the development of high resolution imaging techniques, electrochemists were limited to characterizing deposits on the basis of their macroscopic properties. And for as long as researchers have been electrodepositing metals, they have been using additives in their solutions in an effort to control the properties of the plated films. Although the actual mechanism by which plating additives functioned was usually not known [53], they were usually denoted by the effect they caused on the deposit. In this manner, additives are categorized as brighteners, rougheners, polarizers, depolarizers, inhibitors, accelerators, suppressors, and levelers [54]. Additives have also been developed to increase (or decrease) throwing power, enhance anode dissolution, provide a smooth deposit or refine grain size [55-57]. Many times, numerous terms refer to similar processes, and additives deemed to be of one type actually produce their effects through a different mechanism.

HISTORICAL ADDITIVE NOMENCLATURE

Only recently, after nearly two hundred years, have scientists begun to rigorously explain the deposition process. Brighteners, which increase the reflectivity of the deposit, making them appear more shiny, have been shown to produce this effect by acting as a grain refiner, not surprisingly another name by which they are commonly known [58]. They have also been shown to act as levelers, decreasing the microscopic roughness of the surfaces, leading to a bright and polished look and hence, the frequent reference to them as levelers. Typically the field in which one works will dictate the terms used. Electrochemists who are interested in the qualitative appearance of the deposit will be more likely to describe the additive as a brightener, the property of the deposit in which they are interested in. Those who study the microscopic or atomic surface of the deposit are more likely to use the term leveler.

Additives that act to retard the deposition process have a varied nomenclature, including inhibitor, suppressor and polarizer [6]. In potentiostatic, or potential controlled deposition, a specific potential is applied, resulting in a deposition current that is a function of the system under investigation. The term polarizer is frequently employed, as the additive has the result of necessitating a larger applied potential (i.e. more polarization) to achieve the same current. When controlling the potential, the additive results in a lower current and slower plating rate at a given potential, hence the verbiage of suppressor or inhibitor.

It is easy to see the converse of suppressors in the nomenclature for accelerators. When discussing galvanoplating, the term depolarizer is typically employed, as the additive has the effect of requiring a lower applied potential to achieve the desired plating current. In potential controlled experiments, the accelerator will lead to a greater current and higher plating rate at a given potential. Once again, they way one approaches the matter of interest leads to a description of the effect based on the observed effect. While it is true that the varied naming conventions of plating additives have led to a slew of different names, it is important to note that many of them have a similar meaning.

Another common label for an electroplating additive is a surfactant, or wetting agent. Additives of this nature are frequently used, just as their name implies, to lower the surface tension of the solution and allow for greater wetting of the electrodes. While there are additives whose only purpose is to act as a wetting agent, many of the additives used for other purposes have the secondary effect of acting as a surfactant. This has sometimes led to an accelerator or suppressor being referred to as a surfactant in the literature. Frequently, in the discussion of superfilling in the copper system, the glycol-like molecule is referred to simply as a surfactant [49]. This belied the limited understanding researchers had of the system at the time, as they did not appreciate the role played by the molecule in superfilling or the complex nature of the interaction between the additives that gives rise to superfilling. To prevent undue confusion, this terminology will be avoided herein, except when specifically referring to a secondary effect of one of the additives.

Though dual damascene plating is frequently performed under conditions of current control, this work will refer to the two main additives of interest as a suppressor and an accelerator, in keeping with the potential-controlled nature of many of the experiments, and the conventions used in the literature on copper metallization. Additionally, a third additive of interest will be referred to as the leveler, in keeping with it's primary role in the system. While the suppressor and the leveler both strongly inhibit deposition, they do so by very different means, and consequently, produce different effects. Their nomenclature will be based on their overall effect on the plating system. A final additive, chloride, had different effects that strongly depend on the presence or absence of other additives. To prevent any unnecessary confusion, it will simply be referred to as chloride.

COPPER CHEMISTRY AND DEPOSITION

A thorough understanding of the electrochemical deposition of copper requires an appreciation of the chemistry of copper ions in aqueous solutions. In these solutions, copper has two significant valence states, Cu(I) and Cu(II). While trivalent copper species, Cu(III), do form, they can be neglected in this discussion due to their extreme instability under conditions experienced in typical copper plating [59, 60].

The ionic species of copper found in aqueous solutions are the cuprous and cupric ions, Cu^{+} and Cu^{2+}, respectively. If copper metal is also present, the following equilibrium holds:

$$\mathrm{Cu} + \mathrm{Cu}^{2+} \leftrightarrow 2\mathrm{Cu}^{+} \qquad \{2.1\}$$

In acidified copper sulfate solutions, reaction {2.1} has an equilibrium constant of K_{Cu} = 5.6 x 10^{-7} ± 0.4 x 10^{-7} [61, 62], where K_{Cu} is defined as:

$$K_{\mathrm{Cu}} = \frac{\{\mathrm{Cu}^{+}\}^{2}}{\{\mathrm{Cu}^{2+}\}\{\mathrm{Cu}\}} \qquad (2.1)$$

The activity of a metal is defined as 1, therefore equation (2.1) reduces to:

$$K_{\mathrm{Cu}} = \{\mathrm{Cu}^{+}\}^{2} / \{\mathrm{Cu}^{2+}\} \qquad (2.2)$$

For the electrodeposition of copper, there are three important reactions [63-65]:

$$\mathrm{Cu}^{+} + e^{-} \rightarrow \mathrm{Cu} \qquad U^{0}_{\mathrm{Cu}^{+}/\mathrm{Cu}} = 0.521\mathrm{V}\ (\mathrm{SHE}) \qquad \{2.2\}$$

$$\mathrm{Cu}^{2+} + 2e^{-} \rightarrow \mathrm{Cu} \qquad U^{0}_{\mathrm{Cu}^{2+}/\mathrm{Cu}} = 0.337\mathrm{V}\ (\mathrm{SHE}) \qquad \{2.3\}$$

$$\mathrm{Cu}^{2+} + e^{-} \rightarrow \mathrm{Cu}^{+} \qquad U^{0}_{\mathrm{Cu}^{2+}/\mathrm{Cu}^{+}} = 0.153\mathrm{V}\ (\mathrm{SHE}) \qquad \{2.4\}$$

Cupric ions can combine with metallic copper to form two cuprous species, as shown in reaction {2.1}, the comproportionation reaction. The equilibrium concentration of cuprous ions will be governed by equation (2.2). This equilibrium can be disturbed by the presence of dissolved oxygen in the solution. Oxygen can react with cuprous ions, oxidizing them to cupric ions:

$$4H^{+} + 4Cu^{+} + O_2 \rightarrow 4Cu^{2+} + 2H_2O \qquad \{2.5\}$$

This reaction will prevent the solution from reaching an equilibrium, and lead to the slow dissolution of metallic copper in the solution. It is most likely this dissolved oxygen that has led to reported values for the equilibrium potential of reaction {2.3} to have differences of several millivolts [65], however the possibility remains that these differences arise from different crystal faces of the Cu surface [66-70].

In copper sulfate solutions, copper ions do not complex strongly and exist primarily in the Cu^{2+} valence state. In the absence of an applied potential, equation (2.2) predicts an equilibrium concentration of cuprous ions in the range of 0.4 mM to 0.6 mM for typical plating baths (0.25 M to 0.5 M $CuSO_4$) used in semiconductor metallization. However, this equilibrium is only valid if the solution does not contain dissolved oxygen. As stated above, oxygen in solution will continually oxidize cuprous ions to cupric ions, lowering the cuprous ion concentration to negligible levels and preventing the system from reaching equilibrium.

The electrochemical reduction of copper proceeds by the stepwise reduction of cupric ions to cuprous ions and then cuprous ions to metallic copper; reaction {2.4} followed by reaction {2.2}. The first step, cupric to cuprous is rate limiting [71-73]. The relative rate of reaction {2.2} compared to reaction {2.4} insures that the cuprous ion concentration at the surface is very small in the absence of complexing agents [74].

Many authors have investigated the Potential of Zero Charge (PZC) for the copper surface in various aqueous solutions [65]. The PZC is strongly dependent on the orientation of the crystal face exposed to the solution [75, 76]. Copper has a face-centered cubic structure (FCC), leading to numerous stable crystal faces that can be exposed to solution. If the material being investigated is not a single crystal, the interface with the solution will have domains with different orientations, and the macroscopically measured PZC will be an average of the microscopic domains. Due to the inherent difficulties of measuring a PZC for metal surfaces, a range of values have been reported. In the absence of specific adsorption, the value is 0.08 V ± 15 mV (vs. SHE) [77]. For sulfate solutions with concentrations similar to this work, where the sulfate anion is known to specifically adsorb to the copper surface, a value of 0.04 V (vs. SHE) has been reported [78].

BUTLER-VOLMER EQUATION FOR COPPER ION REDUCTION

Before discussing the details of copper deposition as it relates to the dual damascene process, it is helpful to understand the basics of copper electroreduction. For an electrochemical cell at equilibrium, the potential at the working electrode will reach a steady-state value. The generalized electrochemical reaction involving the oxidized (Ox) and reduced (Red) forms of a species can be written as:

$$\mathrm{Ox} + ne^{-} \rightarrow \mathrm{Red} \qquad \{2.6\}$$

where n is the number of electrons required to reduce Ox to Red. For equation {2.6}, the equilibrium potential, U_{eq}, is related to the activities of Ox and Red, and is given by the Nernst Equation:

$$U_{\mathrm{eq}} = U^{0} + \frac{RT}{nF}\ln\frac{\{\mathrm{Ox}\}}{\{\mathrm{Red}\}} \qquad (2.3)$$

Where U^0 is the standard potential of the reaction, R is the molar gas constant (8.314 J mol^{-1} K^{-1}), T is the absolute temperature in degrees Kelvin, and F is Faraday's constant (94,485 C mol^{-1}). For the reduction of cupric ions to metallic copper, the activity of the metallic copper is defined as 1.0, and the Nernst equation can be written as:

$$U_{\mathrm{eq}} = 0.337 + \frac{RT}{2F}\ln\{\mathrm{Cu}^{2+}\} \qquad (2.4)$$

Applying a potential that is different than the equilibrium potential will lead to a change in the concentration of the electrochemically active species, i.e. a current will flow. The difference between the applied potential and the equilibrium potential is known as an overpotential, η, and is defined as:

$$\eta = U - U_{\text{eq}} \tag{2.5}$$

The current that results from this applied potential is described by the Butler-Volmer equation:

$$I = -I_0 \left[e^{\left(\frac{-\alpha nF}{RT}\eta\right)} - e^{\left(\frac{(1-\alpha)nF}{RT}\eta\right)} \right] \tag{2.6}$$

Where I_0 is the exchange current, and α is the charge transfer coefficient. Although there is no net current flowing at the equilibrium potential, there is still charge transfer occurring in both directions. At equilibrium, the anodic and cathodic currents are equal; their magnitude is given by the exchange current, I_0. For a simple one-electron process with a symmetrical energy barrier, the anodic and cathodic charge transfer coefficients (α_A and α_C, respectively) are usually taken to be equal to 0.5. For a non-symmetrical energy barrier, this is not necessarily the case.

Two limiting cases of the Butler-Volmer equation are of particular importance. The first is the case for a large applied overpotential, η. In these cases, one of the exponential terms approaches zero while the other gets relatively large. For the case of an applied potential negative of U_{eq}, the resulting cathodic current can be represented by:

$$I = -I_0 e^{\left(\frac{-\alpha nF}{RT}\eta\right)} \tag{2.7}$$

Taking the logarithm of each side leads to a form of the Tafel equation:

$$\log I = \log I_0 - \frac{\alpha nF}{2.3RT}\eta \tag{2.8}$$

When plotted on a semi logarithmic plot, the current is linear with the overpotential, and has an intercept of I_0 at U_{eq}. The slope of the curve is :

$$-\frac{\alpha nF}{2.3RT} \tag{2.9}$$

The charge transfer coefficient, α, can be determined from this slope. A similar treatment holds for the anodic branch. Note that the intercept at η = 0 for both the anodic and cathodic branches gives the same I_0, even though $\alpha_A \neq \alpha_C$.

At small overpotentials, both the anodic and cathodic currents must be taken into account. For small η, the relationship $e^x \approx 1 + x$ can be used to reduce equation (2.6) to:

$$I = I_0 \frac{nF}{RT}\eta \tag{2.10}$$

Equation (2.10) shows that the current response is linear with applied potential for small η. A useful concept, the charge transfer resistance, R_{ct}, can be defined as:

$$R_{\text{ct}} = \frac{\partial \eta}{\partial I} \tag{2.11}$$

Appling equation (2.11) to equation (2.10) gives a charge transfer resistance for small η of:

$$R_{\text{ct}} = \frac{RT}{nFI_0} \tag{2.12}$$

R_{ct} can be interpreted as how facile the reaction is. For small R_{ct}, the system will have a large I_0, and small deviations from U_{eq} will rapidly lead to high currents. Conversely, a large R_{ct} implies a small I_0, and it takes a large perturbation in the potential from U_{eq} to get significant current to flow through the cell.

CHLORIDE

Chloride ions have long been added to copper plating baths in concentrations of 10 to 100 ppm (about 0.5 to 5.0 mM Cl^-). At these concentrations, chloride is able to affect the properties of the deposit. It is frequently used to reduce the internal stress of the deposit and to adjust surface properties like microhardness or ductility [79]. In acidified copper sulfate plating baths, small quantities of chloride improve surface brightness [80, 81] and reduce the grain size of the copper deposit [82].

Chloride is present in small concentrations (0.5 - 3.0 mM) in plating baths that exhibit superfilling [6, 32, 45, 46, 52, 83-86]. It is usually added to the solution as HCl or NaCl, both of which strongly dissociate in aqueous solution, and have a negligible effect on the pH and plating properties of the bath. The chloride is present as an ion, and is not reduced or oxidized at potentials used in this study. Consequently, the terms chloride and chloride ions will be used interchangeably throughout this work. Because of its ubiquitous presence in superfilling baths, it is important to understand how the addition of chloride affects a copper sulfate solution.

Chloride ions strongly complex with copper [87], both in solution and on the surface, through the following reactions:

$$\mathrm{Cu} + \mathrm{Cu}^{2+} + 2\mathrm{Cl}^{-} \leftrightarrow 2\mathrm{CuCl}_{\mathrm{ads}} \qquad \{2.7\}$$

$$\mathrm{Cu}^{+} + \mathrm{Cl}^{-} \leftrightarrow \mathrm{CuCl}_{\mathrm{ads}} \qquad \{2.8\}$$

$$\mathrm{CuCl}_{\mathrm{ads}} + \mathrm{Cl}^{-} \leftrightarrow \mathrm{CuCl}_2^{-} \qquad \{2.9\}$$

$$\mathrm{Cu}^{+} + n\mathrm{Cl}^{-} \leftrightarrow \mathrm{CuCl}_n^{(1-n)} \qquad \{2.10\}$$

$$\mathrm{Cu}^{2+} + n\mathrm{Cl}^{-} \leftrightarrow \mathrm{CuCl}_n^{(2-n)} \qquad \{2.11\}$$

Reliable data for the complexation reactions {2.7 - 2.11} do not exist; published values for equilibrium constants span a wide range [88, 89]. CuCl is both soluble in solution and capable of adsorbing on the copper surface. The adsorbed species, $\mathrm{CuCl_{ads}}$, has a stability constant, K_{s0} = 3.3 x 10^{-7} M^2, where K_{s0} is defined as:

$$K_{s0} = \frac{\{\mathrm{Cu}^{+}\}\{\mathrm{Cl}^{-}\}}{\{\mathrm{CuCl}_{\mathrm{ads}}\}} \qquad (2.13)$$

In solutions with low concentrations of chloride, an insoluble film of CuCl is formed on the copper surface [82, 90, 91]. Reaction {2.9} has a stability constant β_2 = 2.4 x 10^5 M^{-2}, where β_2 is defined as:

$$\beta_2 = \frac{\{\mathrm{CuCl}_2^{-}\}}{\{\mathrm{Cu}^{+}\}\{\mathrm{Cl}^{-}\}^2} \qquad (2.14)$$

At higher chloride concentrations, the solution soluble species $\mathrm{CuCl_2^-}$ is also present in measurable quantities; in reactions {2.10} and {2.11}, species do exist for n > 2, however they have such low concentrations that they can be safely ignored in plating baths that exhibit superfilling.

For low concentrations of chloride, an insoluble cuprous chloride film is formed on the surface of the copper. It is formed under open-circuit conditions due to the comproportionation reaction of copper (reaction {2.7}) and from the stepwise reduction of cupric ions to the adsorbed species $\mathrm{CuCl_{ads}}$:

$$\mathrm{Cu^{2+}} + \mathrm{Cl^-} + e^- \leftrightarrow \mathrm{CuCl_{ads}} \qquad U^0_{\mathrm{Cu^{2+}/CuCl_{ads}}} = 0.538\mathrm{V}\ (\mathrm{SHE}) \qquad \{2.12\}$$

The adsorbed $\mathrm{CuCl_{ads}}$ film can be further reduced to metallic copper:

$$\mathrm{CuCl_{ads}} + e^- \leftrightarrow \mathrm{Cu} + \mathrm{Cl^-} \qquad U^0_{\mathrm{CuCl_{ads}/Cu}} = 0.137\mathrm{V}\ (\mathrm{SHE}) \qquad \{2.13\}$$

Between the two equilibrium potentials of reactions {2.12} and {2.13} there exists a range where the $\mathrm{CuCl_{ads}}$ is stable. At potentials more negative of $U^0_{\mathrm{CuCl_{ads}/Cu}}$, the $\mathrm{CuCl_{ads}}$ is reduced further to metallic copper.

To understand the reduction of this film, recall that the equilibrium potential for reaction {2.2} is given by the Nernst equation, equation (2.3). Substituting in gives:

$$U_{\mathrm{eq}} = U^0_{\mathrm{Cu^+/Cu}} + 0.0592 * \log\{\mathrm{Cu^+}\} \qquad (2.15)$$

where the standard potential for reaction {2.2} is 0.521 V (SHE). Because Cu(I) is complexed by the chloride, the expression for $\{\mathrm{Cu^+}\}$ from equation (2.13) can be substituted into equation (2.15), giving:

$$U_{\mathrm{eq}} = U^0_{\mathrm{Cu^+/Cu}} + 0.0592 * \log K_{\mathrm{s0}} - 0.0592 * \log\{\mathrm{Cl^-}\} \qquad (2.16)$$

The equilibrium potential for the electrochemical reduction of CuCl (reaction {2.13}) is given by:

$$U_{\mathrm{eq}} = U^0_{\mathrm{CuCl_{ads}/Cu}} - 0.0592 * \log\{\mathrm{Cl^-}\} \qquad (2.17)$$

By combining equations (2.16) and (2.17), it can be seen that:

$$U^0_{\mathrm{CuCl_{ads}/Cu}} = U^0_{\mathrm{Cu^+/Cu}} + 0.0592 * \log K_{\mathrm{s0}} = 0.137\ \mathrm{V}\ (\mathrm{SHE}) \qquad (2.18)$$

This equilibrium potential for the adsorbate on the copper surface was calculated from the equilibrium potentials for the free metal ions and the solubility product. Note that this calculated value agrees with the given value from reaction {2.13}. This methodology applies to any surface adsorbate where the equilibrium potential is known.

Because of the relatively complex nature of chloride complexation with copper ions, the effect of adding chloride to a copper sulfate plating bath is not straightforward. Researchers have reported chloride to both accelerate and inhibit copper deposition, depending on the conditions. Small quantities of chloride have been shown to accelerate copper deposition at low overpotentials, while slightly inhibiting it at large overpotentials [30, 33, 80, 82, 90, 91].

At low chloride concentrations, chloride's ability to increase the equilibrium concentration of Cu(I) [92] allows the overall reduction of copper to proceed faster [93]. Recall that the rate-limiting step in copper reduction is reaction {2.4}, the reduction of cupric to cuprous ions. The stabilization of the cuprous ions by chloride allows this step to occur more rapidly, which translates into an overall increase in deposition at any given potential.

At higher chloride concentrations, an insoluble film of $CuCl_{ads}$ forms on the surface (reaction {2.8}), inhibiting copper deposition [82, 94]. Copper deposition can be accelerated by further increasing the chloride concentration, which can dissolve the $CuCl_{ads}$ film by forming higher term complexes of cuprous chloride (reactions {2.9} and {2.10}) [82, 94].

Chloride has also been extensively studied for its role at copper anodes [80, 90]. During plating, it is usually desirable to maintain a relatively constant cupric ion concentration. Depletion of the cupric ions during plating at the cathode is compensated for by using a sacrificial copper anode. Copper ions are dissolved into the solution by an electrochemical reaction at the copper anode. However it is important that the oxidation reaction occurring at the anode lead to solution soluble cupric species. Chloride had been shown to enhance this process and prevent passivation of the anode by formation of a copper oxide film.

Chloride has also been shown to affect copper deposition in the presence of other solution additives. For many additives of interest, chloride's effect is a result of the interplay between chloride and the additive. Additives for which this has been reported include thiourea [82], benzotriazole [82, 95] and polyethers [96]. Various explanations for the synergistic effects of chloride and these additives have been postulated [97-100]. Among these are the competitive coadsorption of the chloride and the additive and the formation of various complex complexes between chloride, the additive and copper ions. The effect of chloride in conjunction with polyethers such as PEG or PPG is discussed below.

Although chloride can affect the copper deposit without the addition of further additives, it has become clear that its role in superfilling is in conjunction with other solutions additives, specifically the suppressor [32, 38, 101]. To understand its role more fully, it is helpful to review the various types of suppressors used in electroplating and the mechanisms by which they function.

SUPRESSORS

Solution additives that have the effect of retarding the deposition of a metal are often classified as inhibitors. However this classification masks significant differences in the mechanisms by which they inhibit metal deposition. Of particular importance in superfilling baths are inhibitors that fall loosely into two groups: suppressors and levelers. Although these terms are often used interchangeably in the literature, for the purpose of this work a rigorous nomenclature will be adopted.

An inhibitor will be referred to as a leveler if it is consumed during copper plating. Consumption can occur through many means; some levelers are incorporated into the deposit while others are broken down and have their breakdown products diffuse back into the solution. Unless the consumed leveler is replaced by more leveler from the solution, deposition will no longer be inhibited. In contrast to this, an inhibitor will be classified as a suppressor if it is not consumed during plating. A suppressor will remain at the copper-electrolyte interface and not be incorporated into the deposit during plating. A suppressor does not require continued replenishment from the solution to maintain inhibition.

A leveler's ability to produce a smooth deposit is typically explained by the classical diffusion adsorption theory. Since the leveler is consumed during plating, inhibition will only occur at points on the deposit that are continually re-supplied with the additive. Since the diffusion distance to topological peaks and protrusions will be shorter than to valleys and cavities, these points will receive a greater flux of inhibitor and experience a lower deposition rate. The greater plating rate in valleys and cavities will lead to a smoother deposit.

Some inhibitors of interest for copper deposition are thiourea [54, 102], benzotriazole (BTA) [103] and Janus Green B (JGB). BTA and JGB are more commonly described as levelers, as they are incorporated into the copper deposit during deposition, evidenced by SIMS [39, 40]. BTA has been shown to inhibit copper deposition by slowing the first step of the copper reduction reaction, the cupric to cuprous ion reduction [95].

Of critical importance in the copper plating system used for semiconductor metallization are a class of inhibitors known as suppressors. Suppressors are usually long-chain polyether molecules. The two most discussed suppressors in the literature are PEG and PPG [19, 104, 105], which have been shown to behave similarly. Initially, the role of the suppressor in superfilling was poorly understood, and the polyalkylene glycol was thought only to act as a surfactant, or wetting agent [106]. Recent advances in the understanding of the superfilling process have shown the suppressor's role to be critical [32].

The addition of chloride and PEG to an acidified copper sulfate plating solution has a strong polarizing effect on the deposition [6]. This varies from the addition of either chloride or PEG individually to the system. PEG alone has only a slight inhibiting effect on copper deposition; it is only with the addition of chloride, a known accelerant for copper plating, that the inhibition from PEG is seen.

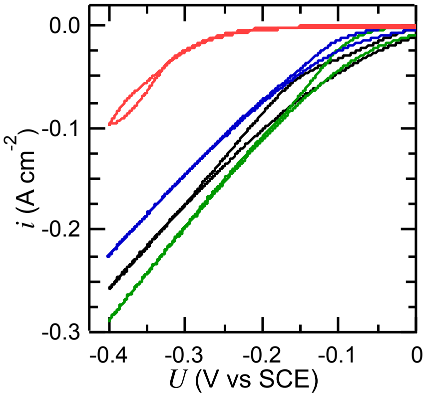

Figure 2.1: Cyclic voltammograms of an acidified copper plating solution with no additives (**black**), chloride (**green**), suppressor (**blue**) and both chloride and suppressor (**red**).

This is can be clearly seen in Figure 2.1, cyclic voltammograms (CVs) of a common copper plating solution used in this work with various additive combinations. The **black** curve shows the response for a base acidified copper sulfate solution with no additives. The **green** curve shows a solution to which chloride has been added. At small overpotentials on the forward scan, the inhibiting effects of the copper chloride surface layer can be seen. At larger overpotentials, the current from the chloride containing solution is slightly greater than that of the base solution, indicating the mild accelerative effects of chloride. Plotted in **blue** is the CV of the base solution with only a suppressor added. Only a slight inhibition is seen. Finally, the **red** curve shows the base solution with both chloride and the suppressor added. A very strong inhibition, present in neither of the solutions with the individual additive, is seen.

The PEG-chloride combination has been shown to inhibit both the deposition and stripping of copper; from this, researchers have concluded that it is a surface active species [107-

109], and higher molecular weights tend to provide better suppression, up to a point [110]. Previous studies have tried to determine the form of the adsorbed species [36, 111]. In the absence of chloride, PEG adsorbs to the copper surface only weakly. A similar effect is seen when plating copper on gold [107]. Neither PEG nor the PEG-chloride complex are able to adsorb on gold, so little inhibition is seen until copper begins to be deposited.

SUPERFILLING

The baths used for copper plating in semiconductor manufacturing contain a number of additives, whose synergistic effect gives rise to superfilling of trenches and vias. To the base acidified copper sulfate bath are added chloride ions, an accelerator (SPS), a suppressor (PEG or PEG-like glycol), and a leveler (nitrogen-containing aromatic, such as JGB). Figure 2.2 shows CVs of various acidified copper sulfate plating solutions. The **black** curve is from a solution that contains no additives. The **red** curve corresponds to a solution that contains chloride and the suppressor. The **blue** curve is a CV of an acidified copper plating solution that contains the full package of additives used in plating, chloride, suppressor, accelerator, and leveler.

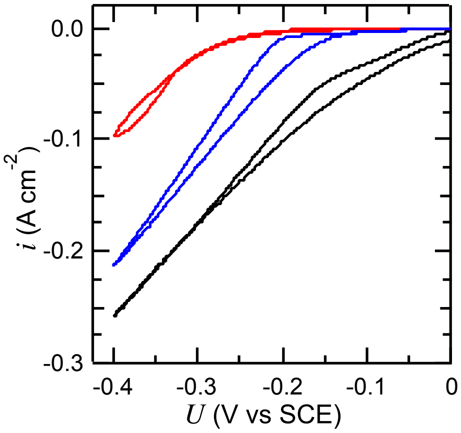

Figure 2.2: Cyclic voltammograms of an acidified copper plating solution with no additives (**black**), chloride and suppressor (**red**), and a full superfilling plating package (**blue**).

The various curves show a significant qualitative difference. However, cyclic voltammetry is a very poor technique to investigate the superfilling properties of a solution package. In fact, most electrochemical techniques are poorly suited to investigate superfilling. To determine if superfilling has taken place requires a cross-sectional microscopy examination of the trenches and vias under investigation. Superfilling is defined to have taken place if the plating rate in the trench exceeds that outside of it, typically leading to the formation of an overfill bump above the trench visible in cross-section [6]. It is the formation of this bump that is the crucial aspect that leads to classifying the deposition process as ‘superfilling’.

Plating baths that exhibited superfilling were employed in manufacturing long before scientists had a clear understanding of how they worked. Prior to their use in the dual damascene plating process, these baths had been used to deposit copper on printed circuit boards [112]. Their subsequent use in chip manufacturing forced scientists and engineers to redouble their efforts to understand and model the process and determine the effects of the various additives. To this end, a number of models were put forward to explain superfilling [6, 30, 39, 106, 113]. In addition, numerous unique methods to fill trenches and vias that did not necessarily take advantage of superfilling have also been explored [39, 106, 114, 115]. Also, a number of baths that were able to fill the trenches were incorrectly labeled as ‘superfilling’ [26, 39, 113, 116].

As previously discussed, additives that retard copper deposition do so through various different mechanisms. One of the early explanations for the bottom up filling demonstrated by damascene plating baths was the classical diffusion-adsorption mechanism [113]. The presence of strong leveling agents in the plating bath led researches to conclude that the different plating rates resulted from an unequal diffusive flux of the inhibitor. The field region was much more exposed to the bulk solution, and hence received more leveler than the surface inside the trenches. This would lead to higher plating rates in the trench, an effect magnified the further one went down the trench.

This model for superfilling had a number of problems. Firstly, rigorous mathematical simulations led to results that differed significantly from experimental trench profiles. The models failed to accurately predict both the induction time that seemed to precede filling and the actual evolution of the trench fill. Secondly, the model failed to predict the ubiquitous overfill bump centered on the trench that occurred experimentally. A number of attempts were made to refine the models to make them more accurately predict the observed experimental results [41], all of which proved to be unsuccessful.

Finally, and most significant, was the demonstration of superfilling in solutions that did not contain the leveler [84]. Only the chloride, suppressor and accelerator were necessary to produce the observed trench filling. It was further shown that trench filling could be achieved in solutions that did not contain the accelerator [86]; if the wafer was dipped in a solution that contained the accelerator, then transferred to a plating solution containing only chloride and the suppressor, trench filling was achieved. This method also produced the overfill bump characteristic of superfilling baths.

Increasing experimental evidence forced researchers to abandon the diffusion based model and explore alternate models to explain the superfilling caused by these plating baths.

CEAC MODEL

Currently, the model that most accurately predicts the evolution of fill profiles in trenches and vias is the curvature enhanced adsorbate coverage (CEAC) acceleration mechanism. West et al. [46] and Moffat et al. [48, 49, 85] independently developed a mathematical description of observed trench filling. This model is based on the surface accumulation of an accelerating species. Following an initial induction period, the trench begins to fill. As it does, there is a rapid decrease in the surface area of the exposed deposit at the bottom of the trench. If the accelerator remains on the surface, this large decrease in area will lead to an increase in surface concentration of the accelerator, leading to increased deposition. This leads to very high plating rates at the bottom of trenches and vias compared to the field region. Due to the very high plating rate at the bottom of the cavity, ‘bottom-up’ filling is observed, as predicted by the model. Following filling of the trench, the concentration of accelerating species directly over the just-filled trench is much higher than the surrounding region, and further deposition leads to a bump above the trench (see figure 1.5). The strength of the CEAC model is that it accurately predicts both the induction time prior to trench filling and the formation of the overfill bump [32].

The CEAC model is not limited to the electroplating of copper. Researchers have demonstrated its validity in an array of various systems. Josell et al. demonstrated superfilling of both the ECD of gold [117] and the CVD of copper [118]. For the CVD copper, adsorbed iodine was the reaction catalyst for the copper carrier gas. As with some copper experiments, there was no excess accelerator in the ‘solution’; the accelerator was pre-placed on the surface and remained there during deposition.

Moffat and co-workers have extensively studied superfilling of Ag in trenches [47, 119-121]. Using patterned wafers with a conformal CVD layer of Ag, they derivitized the Ag surface by dipping it in a solution containing KSeCN, which is known to catalyze Ag deposition. They then transferred the wafer to a solution containing only 0.23 M $KAg(CN)_2$ and 3.4 M KCN. The accelerator, present only at the surface and not in solution, still gave rise to superfilling.

For silver deposition from a cyanide solution, no suppressor was necessary. A suppressor is only needed when deposition in its absence proceeds too rapidly for the accelerator to produce a large difference in plating rates. Note the applicability to the acidified copper sulfate system currently used, where deposition would proceed very rapidly in the absence of a suppressor.

It is useful to look at the overall requirements for trench filling to occur in the CEAC model. First is the requirement that a species can act as an accelerator, increasing the deposition rate based on its presence at the growing deposit interface; how it increases deposition is not important. In the electrochemical deposition of Ag and the CVD of Cu, the accelerator speeds the removal of the ligands; in the electrochemical deposition of Cu, it decreases the effectiveness of the suppressor (see below). Additionally, an increased surface density of the accelerator needs to lead to a greater deposition rate.

Secondly, the accelerator needs to remain on the surface of the growing deposit, regardless of whether it is present in the solution or not. This ability to ‘float’ on top of the growing deposit is what directly gives rise to increased deposition rates as the surface area decreases; concave surfaces and trenches and vias experience a rapid drop in surface area, and hence a large increase in deposition rate due to the accumulation of the accelerator. If the accelerator were to desorb or be incorporated into the deposit, the effect would not be as strong. It has been reported that the accelerator can be deactivated, reducing the superfilling effect [122].

While the CEAC model assumes that the accelerator is only present at the surface of the growing deposit [123], recent evidence indicates that the composition of the solution very near to the surface also needs to be taken into account [32]. This work claims that the accelerator is able to produce acceleration not only while adsorbed on the surface, but by complexing with species very near to the surface.

SUPERFILLING IN ACIDIFIED COPPER SULFATE BATHS

Superfilling was first demonstrated in the acidified copper sulfate baths used in the dual damascene process of semiconductor metallization. It has also been shown to work in the filling of through-silicon-vias (TSVs) [124-126]. As previously mentioned, these baths contained four additives, an accelerator, a suppressor, a leveler and chloride. It is now easy to understand how this specific additive chemistry gave rise to the observed superfilling. The leveler can safely be ignored, as plating baths without it still gave rise to superfilling.

It is the interplay of the accelerator and the suppressor that is of interest when trying to explain superfilling. Experiments with solutions containing only an accelerator (either MPSA or SPS, which behave similarly in solution [127]) do not show any significant acceleration over solutions that do not contain it. In fact, at some concentrations and potentials, addition of just the accelerator to an acidified copper sulfate plating bath will lead to a lower current, i.e. the accelerator is an inhibitor. It is only in the presence of the suppressor (and chloride) that the accelerator acts as a strong accelerator.

From these results it should be obvious the method of acceleration has something to do with the accelerator interfering with the suppressor. To understand how that occurs, it is important to understand the mechanism by which the suppressor operates. In the presence of chloride, the suppressor molecule adsorbs to the surface of the copper. It most likely suppresses copper deposition by physically blocking copper ions from reaching the surface, or significantly slowing their diffusion to the surface by forcing them to migrate through the lattice of the molecule before being reduced at the surface. Adsorption of the accelerator to the copper surface displaces the suppressor, locally eliminating suppression of deposition, i.e. accelerating it [128]. As the deposit expands and the surface area decreases, the accelerator is able to remain on the surface and its surface concentration increases, meeting the criteria of the CEAC Model [129]. Studies show that very little sulfur is incorporated into the deposit [130].

The means by which SPS accelerates copper deposition is not currently clear. One possible method is the simple physical displacement of the suppressor complex. The thiolate bond Cu-S formed is stronger than the Cu-Cl-PEG complex, and the accelerator may simply shove the suppressor out of the way and allow Cu^{2+} ions access to the surface where they can be reduced. It is also possible that the accelerator is able to complex with the hydrated Cu^{2+} ion, whereby the sulfonic group is able to dehydrate the Cu^{2+}. By transforming from the *trans* to the *gauche* configuration, the Cu^{2+} can be brought close to the surface where it can be reduced to metallic copper [131]. This process works for both SPS and MPSA, in addition to 3,3-thiobis(1-propanesulfonic acid) (TBPS). All three molecules contain a sulfur head-group that adsorbs strongly on coinage metals attached to a sulfonic group separated by a three-carbon chain. This mechanism is consistent with results that show cationic species can deactivate the SPS-induced acceleration [132].

However, Schultz et al. found no evidence of a Cu-S bond, and instead proscribe the acceleration to a Cu(I) complex formed between the adsorbed chloride and the sulfonate moiety [133]. Molecular dynamics simulations showed similar results, but did not take into account the thiolate bond in the modeling [134]. There is further evidence that complexation of the solution additives with Cu^{+} is an important factor for acceleration [32].

METAL/ORGANIC FILMS

To understand the effect of the additives in solution, it is helpful to understand the research of a related branch of chemistry: Self-Assembled Monolayers (SAMs). A SAM results from the adsorption of a foreign substance on a surface followed by spontaneous ordering of the adsorbate. Since their initial characterization [135], many different types have been reported by researchers [136, 137], though the most common consist of organic films on metal substrates.

Of particular interest are thiol SAMs formed on metal surfaces. SAMs have been found to form particularly well on the coinage metals: Au [135, 138-141], Ag [138, 140-144], and Cu [138, 140, 141, 143, 145-148]; they have also been reported on Pt [136, 140, 149-153], Pd [150], and Hg [154]. The simplest of these consist of an alkane chain with a sulfur head-group, $HS(CH_2)_nCH_3$, where n is the number of CH_2 groups. Values of n ranging from 1 to 30 have been reported [138, 155, 156]. While short-chain thiols ($n \leq 8$) readily adsorb, their chains are too short to self-assemble into an adsorbed monolayer [156].

SAMs are formed by immersing the metal film of interest into a solvent with a dilute (0.1 - 5 mM) amount of the thiol. Although water can be used as a solvent, the low solubility of most alkanes (especially those with longer chains) in polar solvents such as water makes ethanol or hexane a more common solvent. Immersion times can be as short as a few minutes, though the best films seem to arise after a longer immersion (12 - 24 h) [137, 138].

SAM formation proceeds through two steps, a fast Langmuir-type adsorption followed by a much slower second step associated with the arrangement of the chains into an ordered structure [155, 157, 158]. When thiol molecules in solution come into contact with the metal surface, e.g. Au, the S atom can be reduced to form a thiolate bond, Au-S, [138, 140, 159]. The formation of the thiolate bond through the chemisorption of the thiol to the surface makes it very difficult to remove the moiety from the surface, and leads to very robust monolayers. So robust, in fact, that thiol SAMs can be exposed to air for extended durations without adversely affecting their properties.

On a Au(111) surface, the sulfur head-groups form a highly ordered lattice, which has been identified using Atomic Force Microscopy (AFM) and Scanning Tunneling Microscopy (STM) as the $(\sqrt{3} \times \sqrt{3})R30^\circ$ commensurate overlayer structure [138, 141, 160]. While the sulfur head-groups are held firmly in place, the chains are free to move about, interacting with their neighbors through Van der Waals forces. In minimizing their interaction energy, they form a close-packed structure with a well-defined separation distance from each other. The improvement of the blocking properties of SAMs with extended immersion times is due to the growth of the domain size of aligned tails.

In addition, they have a very distinct tilt and twist off their center-line axis. Transmission Electron Microscopy (TEM) and low-energy electron diffraction (LEED) were used to study these orientations. For the Au(111) surface, a C_{22} monolayer was found to consist of an all-trans zigzag chain canted ~34° from the surface normal and rotated by ~55° [141, 161].

The stability of the thiolate bond makes desorption of the films difficult; it requires that the sulfur be oxidized to a sulfonate moiety. Sulfonate, while still on the metal surface, is only physisorbed, and can be easily removed. Prolonged exposure to an oxidizing agent will degrade the SAM and hasten its removal from the surface. X-Ray Photoelectron Spectroscopy (XPS) has been used to clearly demonstrate the different oxidation states of the sulfur [138, 141, 146, 147]. Adsorbed thiolates can also be desorbed electrochemically, through the oxidation of the thiolate bond. This method has been used to deactivate the accelerator in copper plating solutions used for through silicon via filling [162].

Due to the close packing of the chains, thiol monolayers form a very good blocking layer. In air, the Au-S interface is protected from oxidation by the inability of oxygen in the atmosphere to penetrate the chains and reach the surface. This effect is more pronounced with increasing chain length, and longer chain thiol SAMs have been shown to be stable in air for much longer than short-chain thiol SAMs [146]. This blocking ability also extends to SAMs in contact with solution. Well-formed SAMs can prevent the wetting of a metal surface [135, 138, 141, 163], as has been demonstrated by contact angle measurements [135, 138, 164].

Metal surfaces covered with thiol SAMs have proven to be highly useful in electrochemical studies, as they allow researchers to create chemically and structurally well-defined and controlled electrochemical interfaces. The close-packed nature of the films prevents species in solution as well as the solvent molecules from approaching the surface. And due to the well-understood formation of thiol SAMs, the separation distance between the metal surface and the solution can be controlled to a high degree of accuracy [165, 166]. This has allowed researchers to conduct some unique experiments [167-172], as will be discussed below.

DOUBLE LAYER CAPACITANCE OF METAL / ELECTROLYTE INTERFACE

Electrodes in solution can have two types of processes take place at the electrode-solution interface. The first are faradaic processes, in which some reaction takes place in conjunction with charge transfer. The other are non-faradaic reactions, in which no charge-transfer takes place. Reactions such as desorption and adsorption can and do take place, and can give rise to an overall current through the cell, even though no charge is actually crossing the electrode-solution interface.

The ideal polarizable electrode is one in which no charge transfer can occur across the metal-solution interface, regardless of the potential imposed by an external voltage source. An interface across which charge cannot flow is a capacitor, and the metal-solution interfaces have been shown to behave experimentally like one. There are charges on either side of the solution, which are able to move around with varying levels of freeness. It is helpful to consider where, in relation to the interface, charges may be present. For a metal electrode with high conductivity, all charge will be present at the surface, since it is unable to support an electric field. For charged species in the electrolyte, the charge distribution is more complex.

The most basic model is that proposed by Helmholtz, who postulated that all balancing charge in the electrolyte would be located at the interface, essentially as an adsorbed monolayer [173, 174]. Solvated ions can only approach as close as the H_2O ligands will allow them; this plane is known as the Outer Helmholtz Plane (OHP). In this model, it is assumed that there is no other balancing charge as the distance from the interface increases. This model treats the double layer (DL) capacitance, C_{dl}, as if it were a parallel plate capacitor, and is independent of the applied potential. Expressed in terms of a parallel plate capacitor, it can be written as

$$C_{\mathrm{dl}} = \frac{\varepsilon\varepsilon_0}{d} \tag{2.19}$$

Here, the distance between the plates, d, is given in cm, and the permittivity of free space, ε_0 = 8.85419 x 10^{-14} F cm^{-1}. The dielectric constant, ε, is dimensionless. This distance, d, is usually taken to be 2-3 Å, the length of the OHP. Water has a dielectric constant, ε = 78.3 at 298 K, and using these values to calculate a double layer capacitance leads to values that differ greatly from experimentally measured values. This is because water is a polar molecule, which leads to an effective dielectric constant that is much lower than the bulk value. Typical values for C_{dl} are 10 - 20 µF cm^{-2}. The Helmholtz model works very well for solutions with a high ionic strength.

A second model of the double layer allows for the motion of the ions in the solution, and does not require that all the balancing charge be located at the surface. Treating ions in solution as point charges, this model incorporates a diffuse double layer, with the greatest concentration of excess charge near the interface, and a concentration drop off in the direction normal to the surface. Independently proposed by two researchers [175-177], the Gouy-Chapman Theory bares their names. This model predicts a small capacitance (~10 - 20 μF cm^{-2}) at the potential of zero charge (PZC), U_Z, and an exponential increase in the capacitance as the applied potential moves from the PZC, in direct contrast to the Helmholtz model, which predicts an interfacial capacitance that is independent of applied potential. The Gouy-Chapman model also suffers from the limitation that it predicts a much larger increase in the capacitance than experimental measurements. This model works very well for solutions with low ionic strength.

The failing of the Gouy-Chapman theory is that it treats the charges in solution as point charges that have no limitation on their ability to approach the metal / electrolyte interface. This is what leads to the exponential increase in capacitance as the applied potential moves away from the PZC. This assumption is only valid in solutions of low ionic strength. A third theory was proposed that corrected for the failings of the previous two.

Stern's model took into account the fact that ions in solution are unable to approach arbitrarily close to the interface [178]. Unsolvated ions, or those that experience specific adsorption, cannot approach any closer than the radius of the ion. Those solvated can approach no closer to the surface than their ligands allow. The former is referred to as the Inner Helmholtz Plane (IHP) and the latter the OHP, mentioned above. Stern's modification is known as the Gouy-Chapman-Stern Model (GCS), and is essentially a combination of the Helmholtz and Gouy-Chapman models.

Mathematically, the GCS Model predicts that C_{dl} is composed of two capacitances in series:

$$\frac{1}{C_{\mathrm{dl}}} = \frac{1}{C_{\mathrm{H}}} + \frac{1}{C_{\mathrm{D}}} \tag{2.20}$$

where C_{H} is the Helmholtz capacitance discussed above, with d taken to be the distance to the OHP, and C_{D} is the diffuse double layer capacitance. From the GCS model, C_{D} is related to potential as follows:

$$C_D = \frac{1}{(2\varepsilon\varepsilon_0 z_i^2 e^2 c_i / k_B T)^{1/2} \cosh[z_i e(U - U_Z)/k_B T]} \tag{2.21}$$

where c_i is the concentration of species *i*, and z_i its charge. While C_H is theoretically independent of potential, C_D increases exponentially around its minimum at the PZC. Because series capacitances combine in the reciprocal, C_{dl} will be dominated by the smaller of the two components. Away from the PZC, C_D is large, and henceforth will make a negligible contribution to the total capacitance. C_D also increases with increasing electrolyte concentration and ionic charge, again making a negligible contribution to the total, C_{dl}.

Though there currently exist refinements to the GCS model of the double layer capacitance, these minutiae are inconsequential to this work. In solutions typically employed for semiconductor metallization, the concentrations of the ionic species are relatively high, and the interfacial capacitance in the absence of a specific adsorbate will be dominated by C_{dl}.

ELECTROCHEMISTRY OF SAMS ON METAL SURFACES

As mentioned above, the ideal polarizable electrode is important for the study of electrode-solution interfaces. One such electrode is a mercury electrode immersed in a solution of potassium chloride, which has proven to be a popular system for study. Another more recently discovered system which exhibits this property is a metal surface (typically a coinage metal) with a long-chain SAM formed on it [135]. Because of the similarity in the electrochemistry of SAM-covered surfaces with those found in super-filling baths (specifically, the adsorption of a long-chain organic blocking layer), a short review of the electrochemistry of SAMs is in order.

Because of the highly ordered nature of the adsorbate, long-chain thiol SAMs form a dense organic blocking layer on the surface of the metal [138] whose properties can be easily controlled by researchers [165]. When used in electrochemical research, this high degree of control over the interface has allowed for an interesting array of experiments to be conducted. One such experiment is to investigate the interfacial capacitance of a SAM-covered metal relative to the bare metal surface. It has been shown that for a metal surface covered with a thiol SAM, the measured C_{dl} is much lower. When SAMs of differing chain length (and hence film thickness) were investigated, the double layer capacitance was shown to be inversely proportional to the chain length. Fitting C_{dl} to equation (2.19), and setting d equal to the film thickness returned a value of the film's relative permittivity $\varepsilon \approx 2$ [179].

In another experiment, researchers created two SAMs sandwiched between two mercury electrodes and measured the interfacial properties [180]. Once again, they found that the interfacial capacitance was inversely proportional to the distance between the electrodes, and calculated a dielectric constant for the organic film of $\varepsilon \approx 2.7 \pm 0.3$. Concurrently, they found the resistance of the film to be linearly dependent on length, with a calculated resistivity, $\rho = 1.7 \pm 0.5 \times 10^{14}$ Ω cm, very close to that of bulk polyethylene.

Additionally, electrochemical impedance spectroscopy has been used to model a thiol SAM covered Au surface [181]. It was shown that the interface could be modeled as a capacitor in series with the solution resistance. For monolayers that did not form a complete blocking layer, the model circuit was modified with a high resistance path in parallel with the monolayer capacitance [182]. This can be understood if one takes the SAM covered portion of the surface to be a blocked electrode, with charge transfer only able to occur at the small portion of the electrode where the SAM coverage is incomplete. The high resistance is calculated from

$$R_{\mathrm{P}} = \frac{\partial U}{\partial I} \tag{2.22}$$

where I is the current uncorrected for the actual area of the unblocked portion of the electrode. Because only a very small portion of the electrode is unblocked, the current is very low, even though the current density at the unblocked areas is unaffected by the presence of the SAM at other areas. When corrected for area, the interfacial resistance is similar to that of an unblocked surface.

A Faradaic current can occur on a surface covered with a SAM when the SAM contains defects, such as domain boundaries, pinholes or collapsed sites [136, 183]. It has also been postulated that this current can arise from the tunneling of the electric charge through the organic layer directly to an electroactive species in solution [170]. This same research has shown that the two current pathways may both be present, the tunneling current being strongly dependent on the chain length of the SAM, with a much higher tunneling current present for shorter chains. Additional research has shown that a faradaic current only occurs at pinhole defects in the overlayer, and that tunneling occurs at collapsed sites [184]. They further reported no evidence that tunneling was able to occur across the fully formed SAM, in contradiction to other reports. However, there is a great deal of disagreement and uncertainty in the mechanism of the charge transfer, and even whether tunneling is occurring [185].

Although thiol SAMs have been shown to be highly stable in electrochemical solutions, they can be removed from the surface by the electroreduction of the thiolate bond [186]. This proceeds through the following generalized reaction:

$$\mathrm{Au\text{-}SR} + e^{-} \rightarrow \mathrm{Au} + \mathrm{RS}^{-} \qquad \{2.14\}$$

Porter has extensively studied the electrochemical stripping of thiol SAMs [187]. Using cyclic voltammetry, the reduction of SAMs of various chain lengths from Au and Ag surfaces has been investigated [187-191]. Using a 0.5 M NaOH solution, and scanning in the negative direction from the OCP, they were able to detect a peak shortly before the onset of hydrogen evolution, which they identified as reaction {2.14}. They noted that this peak shifted to more negative potentials with increasing chain length.

Alkanethiols in solution exist primarily in their protonated form. For alkylthiols of the form RSH, $\mathrm{p}K_\mathrm{a}$ values range from 7-11 [192]. Looking at the deprotonation reaction of a generic alkylthiol:

$$\mathrm{RSH} \leftrightarrow \mathrm{RS}^{-} + \mathrm{H}^{+} \qquad \{2.15\}$$

a $\mathrm{p}K_\mathrm{a}$ value of 9 and a pH of 1 would imply one of every billion thiol molecules in solution was in the deprotonated state.

Integration of the charge under the peak lead to a value of 90 ± 7 $\mu\mathrm{C\ cm^{-2}}$, which is very close to the value expected to desorb a monolayer commensurate with a closest-packed adlayer from the surface. The charge under the peak was independent of chain length, indicating that the packing density was not affected by length. They were also able to show using both DL and charge-transfer measurements that following the electrochemical desorption of the SAM, the surface returned to an unblocked state.

These studies were conducted in a very alkaline solution. Studies in strongly acidic solutions did not produce as clear of a desorption peak at negative potentials. The potential at which the thiols desorb is shifted precipitously to more negative potentials, and the current associated with the thiol electro-reduction is completely masked by hydrogen evolution.

Because SAM-covered metal electrodes behave so well as blocked electrodes, i.e. ideally polarizable electrodes, they have been extensively studied by researchers. Of particular interest is the effect they have on metal deposition.

SAMs formed on Au from short-chained alkane thiols ($n \leq 6$) have been studied to determine their effect on the under-potential deposition (UPD) of Cu [168]. The adsorption/desorption of the copper UPD layer is not blocked by the SAM. Relative to a bare Au surface, bulk Cu deposition is mildly suppressed [193]. Deposition was found to occur preferentially at defects in the thiol adlayer. It is important to remember that for these short-chain alkanethiols, a fully ordered SAM is not formed. Full ordering does not occur until the chain length reaches $n \approx 8$. Therefore the blocking associated with longer chain SAMs is not fully evident.

For SAMs formed from longer chains, where blocking would be expected to be more complete, Cu deposition has been found not to occur on the Au surface, but instead on the surface of the SAM [194]. Because of the potential drop across the SAM during deposition, a much larger applied potential is required for the electroreduction of copper [169, 195]. These results would seem to be consistent with monolayers that have no defects, as previous work has shown that deposition would occur preferentially in defects were they present. This was confirmed by deliberately forming pinhole defects in the monolayers, and observing that Cu deposition occurred at these locations [196]. In addition, SAMs have been shown to inhibit Cu deposition in superfilling plating baths on the portions of the copper surface on which they formed [197]. The SAMs did not desorb at the potentials used for plating, and plating was unaffected on other areas of the surface.

Of particular note is that the short-chain SAMs remain on the surface of the electrode following both adsorption and desorption of the Cu. Following the formation of the Cu UPD layer, the alkanethiols are bound to the surface not by a Au-S bond, but by a Cu-S bond. The subsequent stripping of the copper does not remove the thiol, as it returns to being bound to the surface with by Au-S bond. This ability to remain at the solution-electrolyte interface during the deposition and stripping of copper is an important property of these alkanethiols, and has been previously mentioned when discussing the accelerator, a very similar molecule to the short-chain thiols studied here.

Self-assembled monolayers formed by the adsorption of alkanethiols have been extensively studied using electrochemical methods by numerous researchers. Because of a number of interesting similarities, the results from this work can be used to shed light on the behavior of the surface-active species present in plating baths that exhibit superfilling. It is likely that an understanding of the behavior of SAM covered metal electrodes will contribute to an understanding of suppressor covered metal electrodes in the following chapters.

Chapter 3

EIS BACKGROUND

Electrochemical Impedance Spectroscopy (EIS) is a technique whereby an electrochemical interface is investigated by applying a small sinusoidal variation (typically 5 - 10 mV, peak-to-peak) superimposed on a constant DC potential measuring the current response. The frequency of electrochemical relaxations is typically observed over the frequency range 1 MHz to 1 mHz. By probing the interface at different frequencies, the response of different processes at the interface can be separated. The copper sulfate system has long been a subject of investigation by EIS [73, 74, 83, 111, 198-201]. To fully understand EIS, it is helpful to review some of the tenets of impedance and alternating current.

As stated above, in EIS, the applied potential, U_{app}, combines a constant potential, U_{DC}, overlaid with an alternating potential, U_{AC}, which can be represented by the following equation:

$$\tilde{U}_{\text{app}} = U_{\text{DC}} + \tilde{U}_{\text{AC}} \tag{3.1}$$

where the total applied potential is explicitly written as a phasor and the alternating potential, U_{AC}, is given by:

$$\tilde{U}_{\text{AC}} = U_p * \sin(\omega t) \tag{3.2}$$

where U_{p} is the amplitude of the applied perturbation, t is time, and ω is the angular frequency, which is related to the conventional frequency, f, by the following equation:

$$\omega = 2\pi f \tag{3.3}$$

U_{app} will induce in the system a current response in the form of:

$$\tilde{I} = I_p * \sin(\omega t + \varphi) \tag{3.4}$$

where ϕ is the phase angle that separates the current and potential phasors. The current and potential are related by the following equation:

$$\tilde{U}_{\text{app}} = \tilde{I} * Z \tag{3.5}$$

where Z is the impedance of the system under investigation. Z is a function of frequency, and is made up of real and imaginary parts:

$$Z(\omega) = Z_{\text{Re}} - iZ_{\text{Im}} \tag{3.6}$$

where i = √-1. Figure 3.1 is a graphical representation of the sinusoidal current and potential, using both Cartesian (a) and Polar (b) coordinates. The phase angle, ϕ, is related to Z_{Re} and Z_{Im} by the following equation:

$$\phi = \tan^{-1}\frac{Z_{\text{Im}}}{Z_{\text{Re}}} \tag{3.7}$$

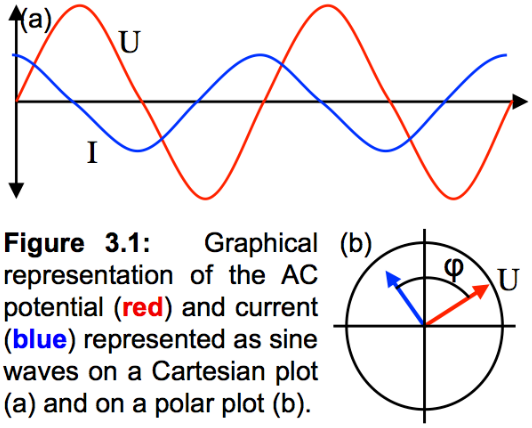

Figure 3.1: Graphical representation of the AC potential (**red**) and current (**blue**) represented as sine waves on a Cartesian plot (a) and on a polar plot (b).

Impedance data is typically plotted in one of two ways. This first is a Nyquist plot (see Figure 3.6 for an example), in which Z_{Re} is plotted on the abscissa and -Z_{Im} on the ordinate over the range of frequencies investigated. The second is a Bode plot, in which the magnitude of Z, given by:

$$Z = \sqrt{Z_{\text{Re}}^2 + Z_{\text{Im}}^2} \tag{3.8}$$

is plotted (in a log-log format) on the ordinate with the frequency on the abscissa; the phase angle is frequently overlaid on the other ordinate, though not on a logarithmic scale (see Figure 3.7 for an example).

An electrode-electrolyte interface can be represented in a very basic manner with an equivalent circuit consisting of a resistor in parallel with a capacitor, depicted in Figure 3.2. The two elements in series represent the two ways in which charge can flow through the interface. The capacitor mimics the double layer response, in which current flows though no charges

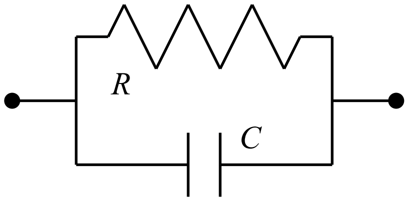

Figure 3.2: Basic equivalent circuit model of electrode-electrolyte interface represented as a resistor in parallel with a capacitor.

actually cross the electrode-electrolyte interface. The resistor accounts for charge transfer in the oxidation/reduction reaction. In a normal resistor, the relationship between the voltage and current is given by the following:

$$V = IR \tag{3.9}$$

Equation (3.9) can also be written in differential form:

$$R = \frac{\partial V}{\partial I} \tag{3.10}$$

Here, the resistance is explicitly defined as the differential of the voltage with respect to the current. For a normal resistor, the resistance, R, should be constant and not voltage-dependent. This is not the case for electrochemical charge transfer. Recall from Chapter 2 the relationship between the current and applied overpotential given in equation (2.7):

$$I = -I_0 e^{\left(\frac{-\alpha nF}{RT}\right)\eta} \tag{3.11}$$

By differentiating, the inverse of the resistance can be written as:

$$R^{-1} = \frac{\partial I}{\partial \eta} = I_0 \frac{\alpha nF}{RT} e^{\left(\frac{-\alpha nF}{RT}\right)\eta} \tag{3.12}$$

and the resistance of the system as:

$$R = \frac{\partial \eta}{\partial I} = \frac{RT}{\alpha nFI_0} e^{\left(\frac{\alpha nF}{RT}\right)\eta} \tag{3.13}$$

Note that the resistance of an electrochemical reaction is not constant and is dependent on the overpotential. This is obvious when one considers the exponential nature of a current-voltage plot from the Tafel equation. As the overpotential increases, the current increases exponentially, and the slope of the curve increases. The increasing slope is consistent with a decrease in the incremental resistance. For copper deposition, the applied potential is more negative than the equilibrium potential, leading to an overpotential, η, which is negative. A larger driving force for deposition will lead to a smaller resistance, as shown in equation (3.13). For small perturbations in η, such as those used in EIS, the current response can be taken as essentially linear, leading to a discreet value of R at a given measuring potential. Knowing R over a range of potentials allows researchers to use equation (3.13) to solve for kinetic parameters of the reaction, such as the transfer coefficient, α, and the exchange current, I_0 [202].

To make the equivalent circuit in Figure 3.2 better reflect the electrochemical cell, some enhancements are required. First, the entire electrochemical cell has an uncompensated resistance, represented in the circuit as R_{S}, which represents the resistance of all other elements in the system (ionic conductivity, cell design, etc.). Second, the double layer capacitance, though usually written as a capacitor, is often taken to be a Constant Phase Element (CPE), represented by an equivalent capacitance, Q, with an exponent, n [203]:

$$Z_{\text{CPE}} = \left(i\omega Q\right)^n \tag{3.14}$$

The exponent, n, is included to account for the fact that a real electrode-solution interface is often not an ideal capacitor, for which $n = 1.0$. For fitting in which $n > 0.9$, the CPE can be assumed to be close to ideal, and we can take $Q = C_{\text{p}}$. The equivalent circuit, known as the Randles equivalent circuit, is shown in Figure 3.3. The total impedance of the equivalent circuit is:

$$Z_{\text{EQ}} = \frac{R_{\text{S}} + R_{\text{P}} + R_{\text{S}} R_{\text{P}} Q (i\omega)^n}{1 + R_{\text{P}} Q (i\omega)^n} \tag{3.15}$$

It is helpful to summarize the behavior of the Randles circuit at various frequencies. At very high frequencies, the impedance of a capacitor (or constant phase element) approaches zero. In this limiting case, the impedance of the parallel capacitor and resistor (which is the inverse of the sum of the inverses) will be dominated by the capacitor, which will be zero. Therefore, the impedance of the entire circuit is R_{S}. At low frequencies, the impedance of a capacitor becomes very large, so the impedance of the parallel element will be dominated by the parallel resistor, and the total impedance of the circuit will be $R_{\text{S}} + R_{\text{P}}$. In both those cases, Z_{Im} will be zero, and the impedance will only be made up of the real part. For intermediate

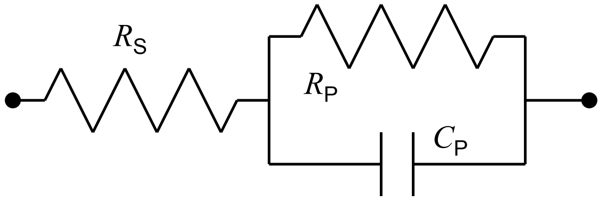

Figure 3.3: Randles equivalent circuit of an electrochemical cell with uncompensated resistance, R_{S}, in series with parallel resistance-capacitance network consisting of a resistance, R_{P}, in parallel with a constant phase element (CPE), denoted here as C_{P}.

frequencies between these two limiting cases, the impedance will have both imaginary and real parts; it is in this region that EIS can provide useful information about the system under investigation.

It should be noted that one key aspect of electrochemical cells has so far been omitted: diffusion. The above discussion assumes that at no point does the diffusion of electroactive species to the surface limit the current able to flow through the cell, i.e. the system is under kinetic limitation. For systems under diffusion limitation, further modifications must be made to the Randles circuit. One such is the addition of a Warburg element, which modifies the impedance to account for diffusion. In the system studied here, the effects of diffusion are noticeable at lower frequencies (typically below 10 Hz). In addition, other circuit models exist that allow for various other forms of electrochemical reactions such as adsorption/desorption (represented by an inductor [201, 204, 205]), multi-step processes [206-209], or others. These are discussed as appropriate below. Equations (3.1) – (3.5) are the only instances currents and potentials will be denoted explicitly as phasors.

EXPERIMENTAL

All experiments were carried out at room temperature in a conventional three-electrode cell located in a Faraday cage to minimize stray electric and magnetic fields. The counter electrode consisted of platinum gauze whose surface area was much greater than the working electrode. It was cleaned in 30 vol% HNO_3 prior to each experiment and was separated from the working electrode compartment with a porous glass membrane. The working electrode was a polished-platinum rotating disk electrode (RDE) (Metrohm Model 628-1) with an area of 0.071 cm^2. The platinum disk electrode was mechanically polished to 50 nm alumina particles, cleaned in 30 vol% HNO_3 for not less than two minutes, and then rinsed with de-ionized water (18 MΩ).

The reference electrode was a saturated mercury/mercury sulfate electrode (SMSE) (U_{eq} = 0.65 V vs. SHE) and was connected to the cell via a Luggin capillary placed about 0.2 cm from the working electrode. All potentials are reported with respect to the saturated mercury sulfate electrode, unless indicated otherwise.

Solutions were prepared from $CuSO_4 \cdot 5H_2O$ (99.7%, J. T. Baker), H_2SO_4 (Assay, Baker), and deionized water (18 MΩ). Three base solutions were employed: 0.27 M $CuSO_4$ and 1.78 M H_2SO_4, (pH = -0.1) henceforth referred to as the high acid (HA) solution; 0.55 M $CuSO_4$ and 0.46 M H_2SO_4 (pH = 0.6) or medium acid (MA) solution; and 0.63 M $CuSO_4$ and 0.1 M H_2SO_4 (pH = 1.3) or low acid (LA) solution. HCl (Assay, Baker) was added to the base solutions to give Cl^- concentrations up to 50 ppm (50 ppm = 50 mg L^{-1} = 1.4 mM Cl^-). After the base solution had cooled to room temperature, a suppressor (Shipley C2001; Rohm and Haas) was added to the base solution in concentrations up to 25 mL L^{-1}. Allowing the solution to cool is important, as the suppressor is known to degrade at elevated temperatures. Prior to each experiment, the platinum disk electrode was plated with a copper film deposited at 1 mA (14 mA cm^{-2}) for 90 s; this film was deposited in the base MA solution and then transferred to the solution of interest after rinsing with DI H_2O. This method has been shown to produce smooth copper deposits, with a roughness factor close to 1 [210]. The thickness of the copper film was about 0.5 μm. All experiments were performed at a rotation rate of 1000 rpm, unless otherwise noted.

Initially, the copper film was deposited potentiostatically at a low overpotential, but this produced very sporadic results. Visual inspection of the electrode surface showed it to sometimes be only partially covered with copper. When investigating this issue, it was noticed that the resultant current was highly variable when compared to the same applied potential of deposition. It was finally determined that this was an effect of the suppressor, and that potentiostatic plating at low overpotentials was inferior to galvanostatic plating, which ensured a constant plating rate and produced a reproducible deposit of known thickness.

Impedance measurements were conducted at constant potential with an RMS amplitude of 10 mV. A platinum wire and 1 μF capacitor were placed in the Luggin capillary, in parallel with the reference electrode. Placement of a platinum wire and capacitor in this manner has the effect of lowering the impedance of the RE circuit and decreasing the noise [211]. Before each measurement, the system was allowed to reach a steady state by holding the potential of the Cu rotating disk electrode at the measurement potential for at least 30 s. Successive spectra at each potential were identical and scans from low to high frequency gave similar results as scans from high to low frequency, demonstrating the stability and reproducibility of these measurements (see below).

CYCLIC VOLTAMMETRY

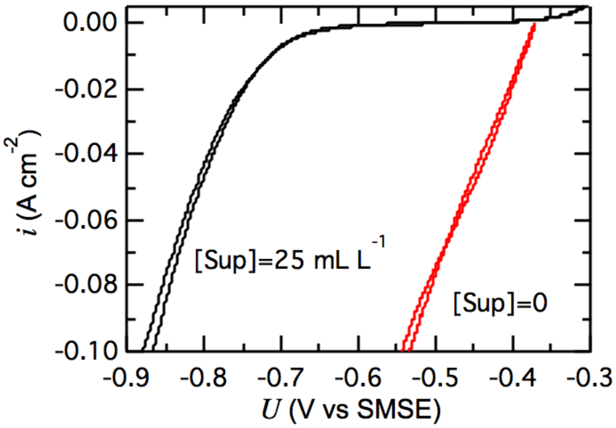

Figure 3.4: Current-potential curves in MA solution containing 50 ppm Cl$^-$ with (**black**) and without (**red**) 25 mL L^{-1} suppressor. The scan rate was 20 mV s^{-1}.

Figure 3.4 shows current-potential curves for a rotating Cu disk in the MA solution containing 50 ppm chloride, both with (**black**) and without (**red**) suppressor. In the absence of the suppressor, the current increased very rapidly as the potential was swept negative of the open circuit potential (U_{OC} = -0.35 V). In solutions with suppressor, the onset of copper deposition was shifted negative by 0.35 V to -0.7 V. This increase in overpotential is due to the adsorption of a suppressor-chloride complex, which strongly inhibits copper deposition [32, 81, 212, 213]. In the absence of chloride, the suppressor does not strongly adsorb on the copper surface and there is little inhibition of deposition.

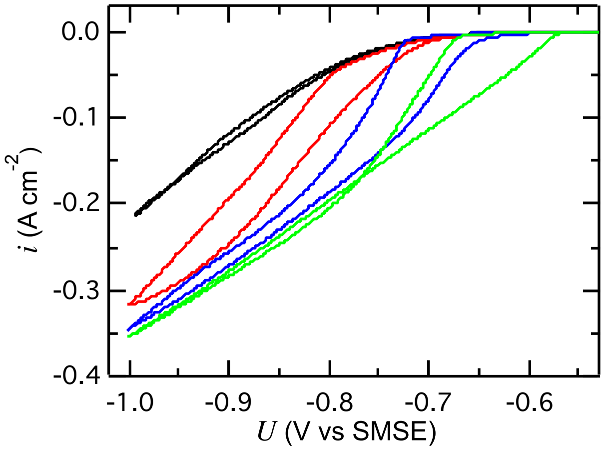

Figure 3.5: Current-potential curves in MA solution containing 25 mL L^{-1} suppressor and chloride ion concentrations of 50 (**black**), 30 (**red**), 15 (**blue**), and 5 (**green**) ppm. Scan rate = 20 mV s^{-1}.

Figure 3.5 shows typical current-potential curves at the Cu disk in MA solutions with 25 mL L^{-1} suppressor and chloride concentrations of 50 (**black**), 30 (**red**), 15 (**blue**) and 5 (**green**) ppm (1.4 to 0.14 mM). For the 50 ppm Cl$^-$ solution, the current increases exponentially with potential, typical for a fully suppressed copper surface. For solutions with [Cl$^-$]< 50 ppm, the current is the same as for the 50 ppm solution at low overpotentials, however, at more negative potentials the deposition current increases to values larger than in the 50 ppm solution. The critical potential at which this increase occurs, U_{crit}, becomes more negative with increasing chloride concentration. This characteristic increase in deposition current compared to the deposition current for the 50 ppm solution at a critical potential indicates a transition from a state of suppression to a state of non-suppression at the metal-solution interface.

It is also evident from the current-voltage curves that for [Cl$^-$] < 50 ppm, the reverse scans exhibit hysteresis in that deposition continues to a more positive potential than in the forward scan. A similar effect is well known for copper deposition from solutions that contain chloride, suppressor, and accelerator [84, 214] and is attributed to the gradual displacement of the suppressor complex by the accelerator, leading to an increased deposition rate. In this case there is no accelerator present, and the hysteresis is due to slow re-adsorption of the suppressor complex as the potential is swept positive of the critical potential. A similar effect has been reported for copper deposition from solution containing chloride and polypropylene glycol as the suppressor, but no accelerator [36].

IMPEDANCE SPECTROSCOPY

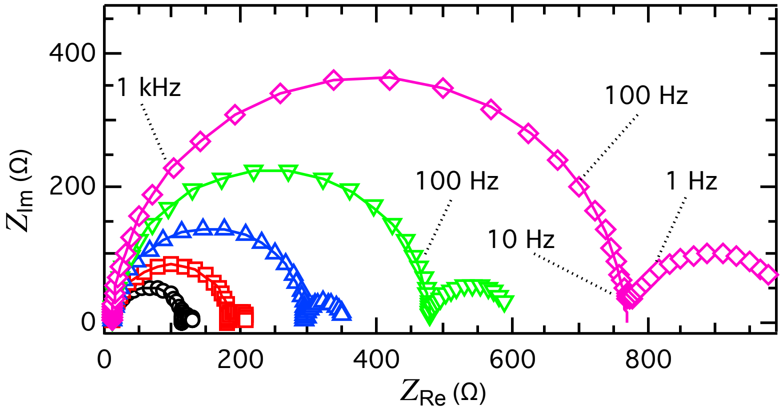

Figure 3.6: Complex-plane (Nyquist) plots of the MA solution containing 25 mL L^{-1} suppressor and 30 ppm chloride at applied potentials of -0.68 V (○), -0.66 V (□), -0.64 V (△), -0.62 V (▽), and -0.60 V (◇) (all vs. SMSE). The solid line shows a fit to equation 3.15.

During EIS, the system is held at a constant DC potential while a small AC perturbation is applied to the signal. The frequency of the AC perturbation is systematically changed, giving the response of the system over a wide range of frequencies. With each new frequency, the system is allowed to reach a steady-state before the measurement is taken.

Figure 3.6 is a complex plane (Nyquist) plot of the MA solution with 25 mL L^{-1} and 30 ppm chloride at a copper rotating disk electrode; potentials of -0.68 V (○), -0.66 V (□), -0.64 V (△), -0.62 V (▽), and -0.60 V (◇). In all cases, two loops with distinct time-constants are observed. Similar results were obtained at other chloride concentrations (not shown), as well as in the LA and HA solutions. The higher frequency loop is associated with charge transfer at the interface and was modeled using the Randles equivalent circuit shown in Figure 3.3 and the data were fit using equation (3.15). In most cases, fitting produced $n > 0.9$, and we take $Q = C_P$. For all five potentials, a lower frequency loop is observed in addition to the high frequency loop associated with the interfacial charge transfer. This low frequency loop is associated with the diffusion-limited flux of copper ions to the surface. Figure 3.7 displays the same set of data plotted on a Bode plot.

From analysis of the impedance spectra we can make the following observations. At very high frequencies, the impedance of the capacitor tends to zero. Therefore, the total impedance of the system will be R_S. In the system under investigation, R_S is a function of the geometry of the cell, the ionic conductivity of the solution, and the resistance of the wires used in the experiment. In Figure 3.7, it can be seen that the impedance at high frequency is independent of the applied potential, typically 11 - 12 Ω.

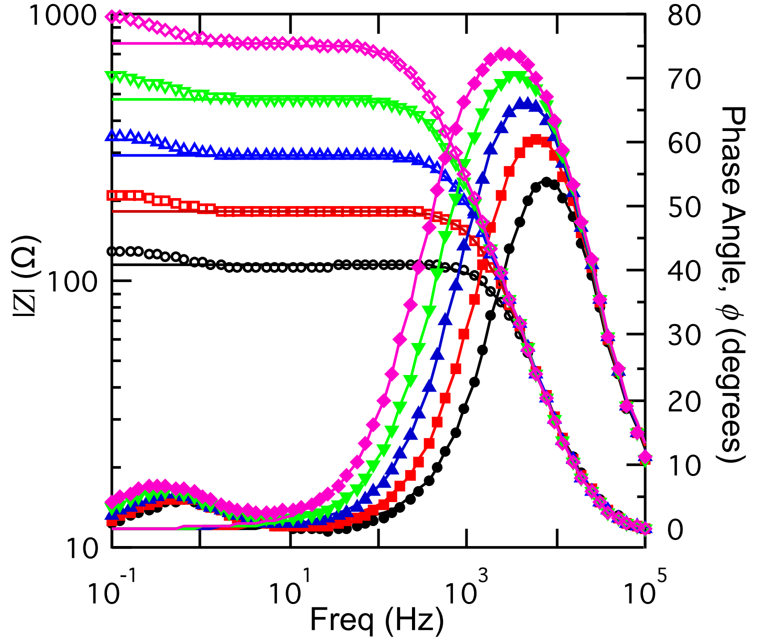

Figure 3.7: Bode plot of the MA solution containing 25 mL L^{-1} suppressor and 30 ppm chloride at applied potentials of -0.68 V (○●), -0.66 V (□■), -0.64 V (△▲), -0.62 V (▽▼), and -0.60 V (◇◆) (all vs. SMSE). The left axis (hollow markers) is the magnitude of the impedance and the right axis (solid markers) is the phase angle, *f*. The solid line shows a fit to equation3.15.

The other limiting case of the circuit model is reached at low frequencies, where the impedance of the capacitive element goes to infinity. In this case, the overall impedance of the circuit is the sum of R_S and R_P. The parallel resistance element can be thought of as the charge-transfer resistance, R_{ct}. Figures 3.6 and 3.7 show the dependence of R_P on applied potential. As the potential is stepped from -0.60 V to -0.68 V, R_P decreases from about 800 Ω to about 120 Ω. Figure 3.7 also illustrates the range of frequencies over which the changing impedance of the capacitance affects the measurements. At frequencies above 100 kHz, the impedance of the CPE is close to zero, and investigating the system at higher frequencies would not be helpful. Furthermore, below 100 Hz, the impedance of the CPE becomes so high that nearly all the current flowing through the system is going through the resistive element. This is much more noticeable by looking at the value of the phase angle. At all five potentials, the magnitude of the impedance has reached a steady-state value before the phase angle had dropped to zero, indicating some residual capacitive behavior in the system.

The limits of the interfacial circuit model used here are also readily apparent. For frequencies below 10 Hz, the model predicts a constant impedance (solid lines in Figures 3.6 and 3.7). However, at all five potentials a second smaller loop is seen on the Nyquist plot. This is seen on the Bode plot as a gradual increase in the impedance at low frequencies, and a second local maximum in the phase angle. At these low frequencies, the effect of the CPE on the total impedance is negligible. Instead, the effects of diffusion of the electroactive species, in this case cupric ions, to the surface are seen. This will be discussed in greater detail below.

When performing these experiments, it is imperative that the measurements remain reproducible over the time scale of the experiment. For these experiments, the frequency range from 100,000 to 0.1 Hz was investigated, with 10 frequencies per decade, for a total of 60 measurement points per spectrum. During this time, a constant DC potential is being applied resulting in a constant driving force for copper deposition on the electrode surface. Typical experimental durations were on the order of 15 min. For high plating rates, a significant amount of copper can build up on the electrode, possibly changing its area or character, or allowing aging of the solution that could affect the measurements. It is therefore not inconceivable that the system will not be in equilibrium for the entire period. If it is not, the data collected at the beginning of the experiment will not be comparable to that collected at the end. Experiments are typically conducted by sweeping the frequency from high to low. If the system is stable over the duration of the experiment, a sweep in the reverse direction, from low to high frequency, should produce identical results.

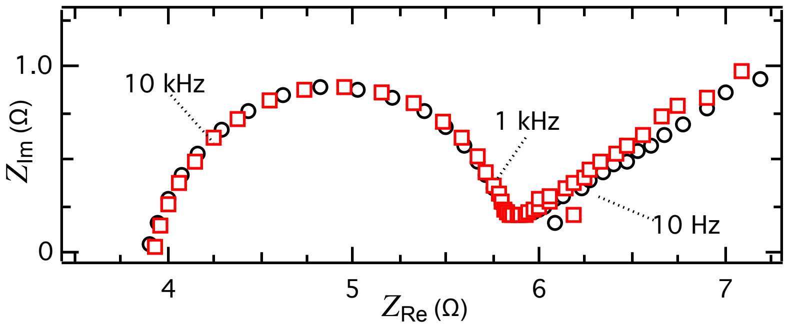

Figure 3.8: Nyquist plot of HA solution containing 50 ppm chloride with applied potential of -0.2 V vs. SCE. The frequency was either swept from 100k Hz to 1 Hz (○) or 1 Hz to 100 kHz (□).

Figure 3.8 shows just a spectrum for the high acid solution with added chloride (270 mM $CuSO_4$, 1.8 M H_2SO_4, 1.4 mM Cl^-). The applied potential is -0.2 V (vs. SCE) and the frequency was swept from both high to low (100 kHz to 1 Hz, (○)) and low to high (1 Hz to 100 kHz, (□)). As can be seen, the data are nearly identical, and fitting to the circuit in Figure 3.4 returns nearly identical results (Table 3.1). Note that in this experiment, the rotation rate of the electrode was zero (i.e. it was stationary). Throughout the course of this investigation, experiments such as this were conducted periodically to ensure the validity of the data. Unless otherwise stated, the sweep direction of the frequencies did not unduly affect the measured data.

Table 3.1

Sweep direction	R_S (Ω)	R_P (Ω)	C_p (μF)	n
High to Low	3.95	1.89	19.0	0.964
Low to High	3.95	1.91	20.8	0.957

To further confirm the stability of the solution under experimental conditions over time, experiments were repeated in succession. Figures 3.9a and 3.9b show Nyquist plots of frequency sweeps at +0.02 V (vs. SCE) and -0.12 V (vs. SCE), respectively. The scans were conducted in the MA solution with no additives (550 mM $CuSO_4$, 0.46 M H_2SO_4), and were alternated between the two potentials until all eight scans were completed. The figures illustrate some important points; the scans are very reproducible, and the potential dependence of the charge transfer resistance is clear. The slight drift in the spectra has been seen by previous authors [215]. It is also clear from these figures (Figure 3.9b in particular), that these data cannot be fit using a simple Randle's circuit. Interestingly, the results are similar to those for copper deposition in perchlorate solutions [216] and match simulations for a reaction that has a solution soluble intermediate [217]. We can attempt to fit the data using a two-element equivalent circuit, as shown in Figure 3.10, as it is more likely to produce a good fit [128].

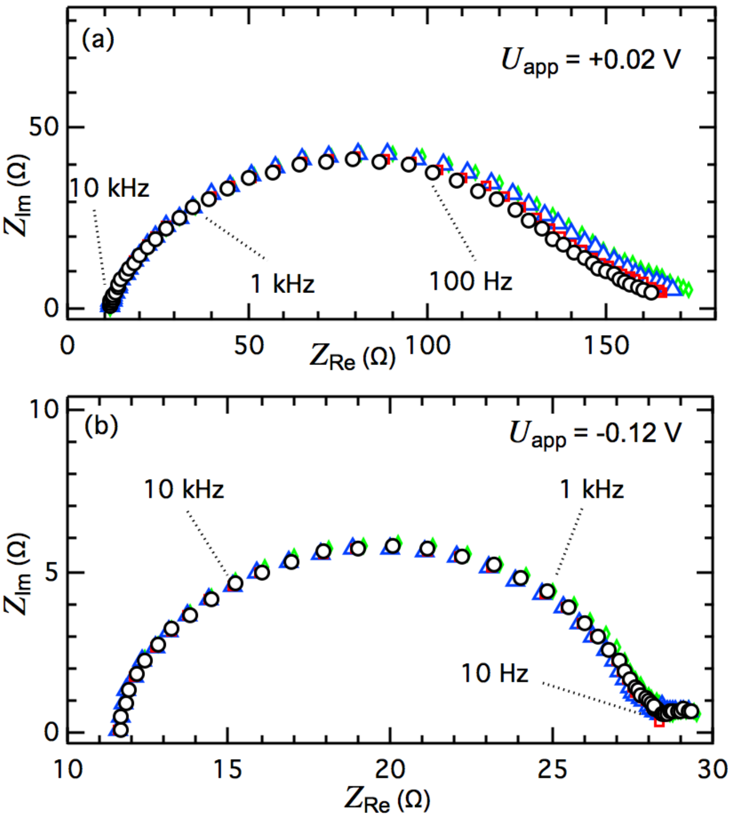

Figure 3.9: Nyquist plots of MA solution with no additives at applied potentials of (a) +0.02 and (b) -0.12 V vs SCE. Experiments were performed sequentially, with (○) first, followed by (□), (△), and finally (◇).

Figure 3.10

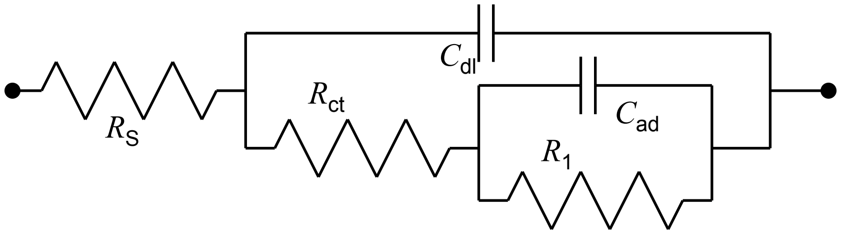

Figure 3.10: Model of two-element circuit used to fit data consisting of the electrical double layer, C_{dl}, in parallel with the charge transfer resistance, R_{ct}, in series with an element that accounts for adsorption of an active copper species as part of the electrodeposition process.

The equivalent circuit in Figure 3.10 is designed to mimic a two-step Cu reduction process, with the reaction {2.4} being followed sequentially by reaction {2.2}. C_{dl} is the capacitance of the electric double layer; R_{ct} and R_1 are the charge transfer resistances of the two steps of the copper ion reduction; the second parallel element C_{ad} accounts for the adsorption of a reaction intermediary to the copper surface [218].

Figures 3.11a and 3.11b show the initial scans from Figures 3.9a and 3.9b (open circles) and the fits using the circuit in Figure 3.10 (solid line). The best fits are summarized in Table 3.2:

Table 3.2

	R_S (Ω)	R_{ct} (Ω)	C_{dl} (μF)	n_{dl}	R_1 (Ω)	C_{ad} (μF)	n_{ad}
+0.02 V	11.58	27.55	18.2	0.785	120	196	0.415
-0.12 V	11.49	2.45	9.33	0.862	14.4	47.8	0.643

From the data, the potential dependence of the charge transfer resistance is clear; higher overpotentials (more negative applied potentials) are consistent with a smaller charge transfer resistance. However, it is also apparent from the data and the fits that attempting to fit the data to this equivalent circuit has difficulties. The values of n for both constant phase elements were significantly less than 1, indicating a high degree of non-ideality in trying to model the process as ideal capacitors. In addition, the double-layer capacitances, which have not been corrected for area (≈ 0.071 cm^2) are significantly higher than would be expected for a metal surface in contact with an electrolyte solution (125 - 250 μF cm^{-2} versus an expected 10 - 20 μF cm^{-2}). From this it can be concluded that we will have great difficulty deriving physical factors by trying to fit to this cell, a phenomenon seen previously with similar solutions [128, 201].

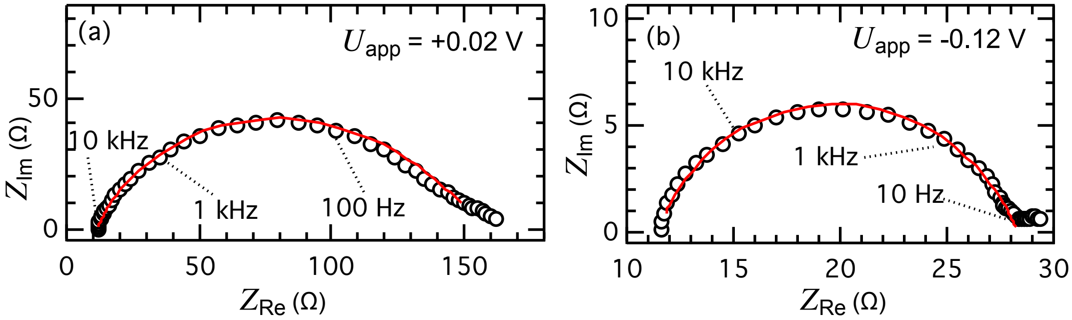

Figure 3.11: Nyquist plots of MA solution with no additives at applied potentials of (a) +0.02 and (b) -0.12 V vs. SCE (○) and a best fit (**solid red line**) using the two-element circuit in Figure 3.10.

It is also interesting to note that the solution used in these experiments did not contain chloride. The reduction of cupric ions in a sulfate solution has long been known to take place via the two-step process denoted in reactions {2.4} and {2.2}, with reaction {2.4}, the reduction of cupric ions to cuprous ions being the rate limiting step [71, 219]. Relative to the first step, the reduction of cupric ions to copper is much faster. Modeling this process using electrochemical impedance spectroscopy requires using an equivalent circuit model similar to that used in Figure 3.10. From the fitting results shown in Figures 3.11a and 3.11b, a few inferences can be made. Though the values listed in the table above should not be taken at face value, the near order of magnitude difference in the two parallel resistances is a strong indication of a two-step process, one of which is much faster than the other. For the data at -0.12 V, it is likely that the 14.4 Ω resistance corresponds to the reduction of cupric ions to cuprous ions, and the 2.45 Ω resistance to that of the reduction of cuprous ions to copper. However, the actual process is likely far more complex than this simple circuit would imply.

For the reduction of copper in the absence of chloride, many reaction steps could be hypothesized. For example, it could include: adsorption of a complexed cupric ion, de-chelating of the ion, reduction to a cuprous ion, desorption of the cuprous ion, the comproportionation reaction between copper and cupric ions to form two cuprous ions, reduction of a cuprous ion to copper, and of course, a reaction involving a one-step process in which a cupric ion is reduced directly to copper by reacting with two electrons simultaneously. It should immediately be obvious that creating an equivalent circuit model this complex will lead to some very clear problems. The first is that some of the reactions mentioned have similar time constants, and it may not always be possible to disentangle the effects from each other. The second, and more fundamental problem to actual experimentation is that you have a circuit whose large number of fitting parameters significantly exceeds the data being fit. In a situation like this, it is very easy to achieve multiple equally good fits using different fitting parameters. Consequently, the resulting interpretation of the physical constants represented by the model circuit elements becomes complex. Trying to deduce the fundamental reaction constants from systems such as this can lead researchers to ‘find’ results in the data that are not actually there. Even when one is cautious to ensure the fitting parameters have an echo in reality, false fits can abound. This is not to say that good models cannot be created based on the underlying kinetics, only that EIS can at times be a very blunt tool to investigate very complex systems.

For the bulk of this analysis, a simple Randle’s circuit will be used, except where specifically stated. Returning to the data shown in Figures 3.6 and 3.7, we can see a situation in which the Randle's fit is particularly apt. This solution contains chloride, which is known to complex with cuprous ions, stabilizing them and increasing their concentration in solution. It also has the effect of making the first step of the copper reduction reaction faster. Therefore, it is not unexpected to see that fitting electrochemical impedance spectroscopy data to the cell would produce a good fit.

In Figures 3.6 and 3.7, it is clear that there is a significant potential dependence to the measured impedance data. Scans were conducted from -0.54 V to -0.86 V (vs SMSE) for the MA solution containing 25 mL L^{-1} suppressor and chloride concentrations of 50 (○), 30 (□), 15 (△), 10 (▽), and 5 ppm (◇). While it is clear that the charge transfer resistance is strongly dependent on the applied potential (discussed more below), the series resistance does not show the same dependence. Figure 3.12 is a plot of those R_S values.

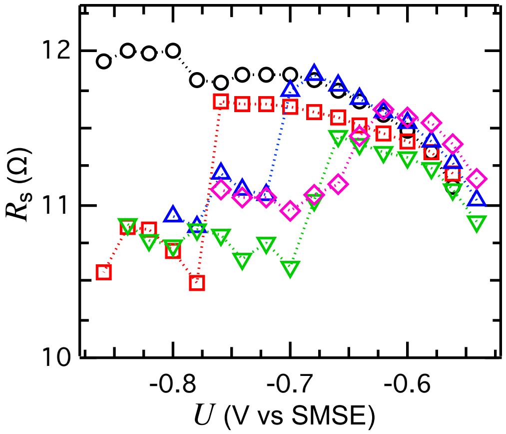

Figure 3.12: Plot of R_S at different applied potentials in the MA solution containing 25 mL L^{-1} and chloride concentrations of 50 ppm (○), 30 ppm (□), 15 ppm (△), 10 ppm, (▽), and 5 ppm (◇).

A few things can be deduced from these data. First, the series resistance of the cell is broadly independent of applied potential as expected. The series resistance should be primarily a function of the cell geometry, the electronic components used in the experiments—the electrodes, wires, equipment, etc.—and the conductivity of the solution itself. None of these things change from one applied potential to the next. However, there are two minor potential dependencies, to be discussed below. The second important thing to note is that the addition of various amounts of chloride did not lead to a large change in the series resistance. However, it did manifest itself in one small but important way.

At a chloride concentration of 50 ppm, the series resistance is very constant as the frequency scans are conducted at progressively more negative potentials. A similar result is seen in a solution containing 30 ppm chloride, with the exception that there is a sharp but relatively small decrease at around -0.76 V vs. SMSE. Similar sharp drops are seen at other chloride ion concentrations, with the decrease shifting to more positive potentials as the chloride ion concentration decreased. This is an interesting effect that will be discussed extensively throughout this work, but is noted here for thoroughness. Though there is a jump in the series resistance at a relatively well-defined potential, the jump is small, and doesn't broadly change the overall series resistance.

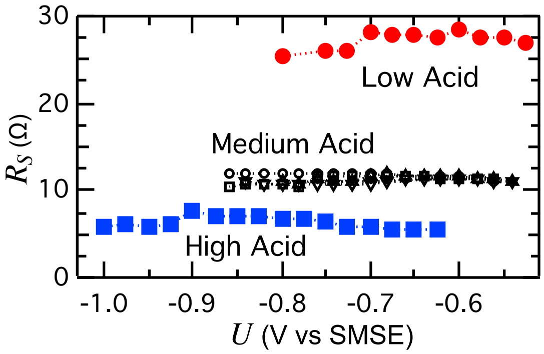

Figure 3.13: Plot of R_S at different applied potentials in the LA (●), HA (■) and MA solution containing 25 mL L^{-1} suppressor and chloride concentration of 50 ppm. For the MA solution, chloride concentrations of 50 ppm (○), 30 ppm (□), 15 ppm (△), 10 ppm, (▽), and 5 ppm (◇) are shown.

Figure 3.13 shows two representative plots of R_S versus potential for the HA (■) and LA (●) solutions, both with 25 mL L^{-1} suppressor and 50 ppm chloride. It is clear from the figures that R_S is independent of potential over the measured range In both solutions there is a small but sharp drop in R_S, similar to that seen in the MA solution. For the LA solution, the drop is shifted to a more positive potential, while the shift in the HA solution is significantly negative. Another key point to note is that good fits were achieved at far more negative potentials in the HA solution than in the MA solution. The opposite was seen in the LA solution, in which good fits of the data could only be obtained at potentials more positive of that which was achievable in the MA solution.

However, the most obvious and most important difference between the three solutions is the clear difference in the series resistance. This is most likely caused by significantly different conductivities of the three solutions. For the ionic solutions used in this work, the conductivity will be related to the sum of the charged species in the solution, as approximated in the following formula:

$$I = \sum_i c_i |z_i| \tag{3.16}$$

where species i has concentration c_i and charge z_i. (This should not be confused with the ionic strength of the solution, which is calculated using the square of the charge of each species.) To calculate this value, the speciation of the solutions must be calculated. This can be done using the following series of equations and their corresponding equilibrium constants.

$$H_2SO_4 \Leftrightarrow H^+ + HSO_4^- \qquad \{3.1\}$$

$$HSO_4^- \Leftrightarrow H^+ + SO_4^{2-} \qquad \{3.2\}$$

with $K_1 = 2.4 \times 10^6$ and $K_2 = 1.0 \times 10^{-2}$, defined as:

$$K_1 = \frac{\{H^+\}\{HSO_4^-\}}{\{H_2SO_4\}} \qquad (3.17)$$

$$K_2 = \frac{\{H^+\}\{SO_4^{2-}\}}{\{HSO_4^-\}} \qquad (3.18)$$

Because the pH is known (and hence $\{H^+\}$) for each solution, the speciation of each solution can be determined. This was done using HYDRAQL. Because the cell setup remains unchanged, the observed change in R_S must be due to the differences in the solution. There is no appreciable difference in the solution viscosity, so the change in R_S should be due to different ionic conductivities.

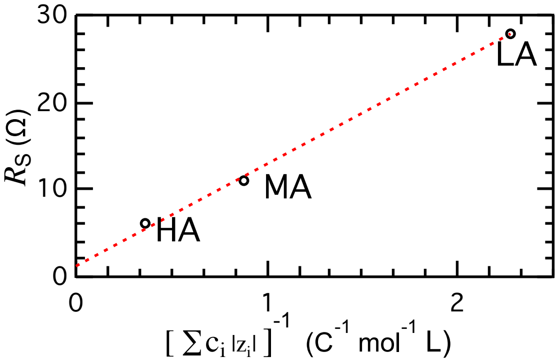

Figure 3.14: Plot of average R_S values for the three base solutions as a function of the inverse of the total ion concentration in the solution.

Figure 3.14 is a plot of R_S versus the *inverse* of the ionic concentration of each solution. The dashed line is a linear fit (R^2 = 0.998). As the inverse ionic concentration approaches zero (i.e., infinite ionic conductivity), the series resistance approaches a value just above zero. This is to be expected [181]. The conducting parts of the experimental setup are made of very low impedance metal wires, and should have a very low conductivity. The cell has been designed to minimize resistance as much as possible. Though the data plotted in Figure 3.14 are only a rough guide, and do not take into account the ionic concentration or its effect on the activity coefficients, the effect is clear: the solution causes a large uncompensated series resistance that will have major implications, discussed in further detail later in this chapter.

Figure 3.15 shows the inverse of the interfacial capacitance derived from the EIS data shown in Figures 3.5 and 3.6 plotted scale versus the applied potential. The values are from the same fits as the R_S values in Figure 3.12, and the various chloride ion concentrations shown (5 - 50 ppm) are represented by the same symbols. The capacitance was corrected for the surface area (≈ 0.071 cm^2) and is therefore shown as the inverse of the capacitance per square centimeter. C_P^{-1} increases with increasing overpotential, and is broadly independent of chloride ion concentration, expect for the solution with only 5ppm chloride. However, each solution shows a significant and rapid drop in C_P^{-1} (i.e. a large increase in the interfacial capacitance) at a potential that becomes increasingly negative with higher chloride ion concentrations. Negative to this potential, the capacitance is roughly independent of both applied potential and chloride ion concentration. For the solution with a chloride ion concentration of 50 ppm, only a hint of the beginning of a decrease is evident.

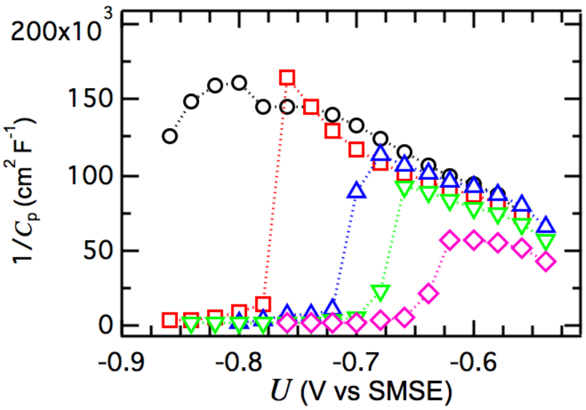

Figure 3.15: Plot of the inverse of the area corrected C_P at different applied potentials in the MA solution containing 25 mL L^{-1} suppressor and chloride concentrations of 50 ppm (○), 30 ppm (□), 15 ppm (△), 10 ppm, (▽), and 5 ppm (◇).

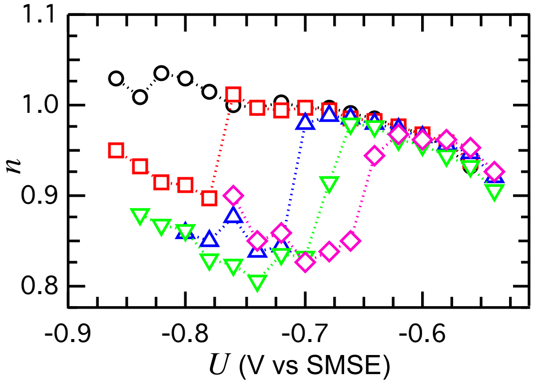

Figure 3.16: Plot of n at different applied potentials in the MA solution containing 25 mL L^{-1} suppressor and chloride concentrations of 50 ppm (○), 30 ppm (□), 15 ppm (△), 10 ppm, (▽), and 5 ppm (◇).

Figure 3.16 shows the values for n from the same series of experiments for the fitting of the constant phase element of the Randle's circuit given in equation (3.15). As can be seen, the values of n for nearly all potentials and chloride concentrations are very close to 1.0, indicating a very good fit to the circuit model and implying it is a good representation of the reactions taking place at the interface.

However, as seen in Figure 3.12, a transition is seen at a potential that becomes increasingly more negative with increasing chloride concentration.

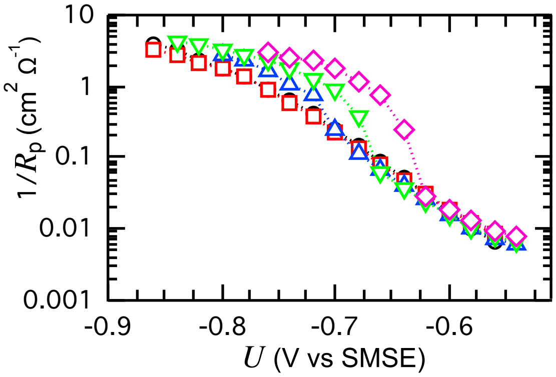

Figure 3.17: Plot of the inverse of the area corrected R_P at different applied potentials in the MA solution containing 25 mL L^{-1} suppressor and chloride concentrations of 50 ppm (○), 30 ppm (□), 15 ppm (△), 10 ppm, (▽), and 5 ppm (◇).

Figure 3.17 is a semi-logarithmic plot of the inverse of the interfacial charge transfer resistance, R_P^{-1}, versus the applied potential, where R_P has been corrected for the area of the working electrode. At potentials more positive than -0.6 V (vs. SMSE), the slope of the graph deviates from linearity. Between this potential and -0.75 V (vs. SMSE), the slope of the graph is linear, with additional deviations seen for potentials more negative than -0.75 V. Also very evident is a significant and somewhat sharp increase in R_P^{-1} (corresponding to a *drop* in the charge transfer resistance) at various potentials whose value is a function of the chloride ion concentration. It is clear from this and the preceding figures that the potentials at which this transition takes place are the same. It also corresponds to the same potential at which the current increases, as seen previously in Figure 3.5. Clearly, some transition in the deposition kinetics is occurring at these potentials.

To further understand this, it will be helpful to adjust the applied potential for the uncompensated resistance, or IR-drop. The non-negligible series resistance coupled with a large current flow leads to a significant IR-drop in the cell. Correcting for this will allow the plotting of R_P^{-1} and C_P^{-1} as a function of the potential that is applied to just the metal-solution interface. The potential drop occurring over other parts of the cell is represented by the product of the series resistance R_S and the current, I. Note that the potential is corrected for the bulk current, and not the current density, which is dependent upon the area of the working electrode. To determine this potential, the applied potential must be subtracted from the product of the steady-state current measured during the experiment, and the R_S value obtained from fitting to the simple

Randle's circuit. Figures 3.18 and 3.19 show C_P^{-1} and R_P^{-1} re-plotted with applied potential corrected for the IR-drop.

Immediately apparent in Figure 3.18 is that the transition from one state to the next is much sharper, and occurs over a much narrower potential range than was apparent from previous figures. Also, more apparent in this plot is that the 50 ppm chloride solution seems on the verge of undergoing a transition from one state to the other, and may even be at its transition potential, (though this may be contradicted by the lack of an apparent transition potential visible in Figure 3.19).

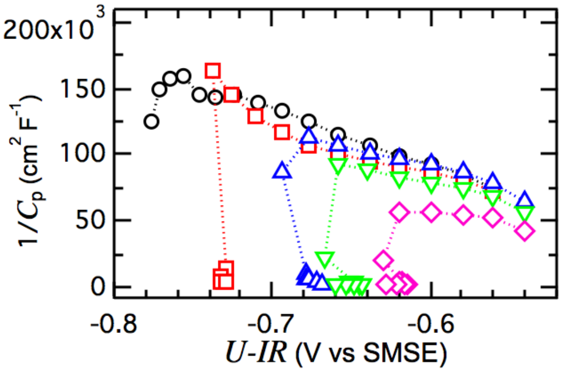

Figure 3.18: Re-plot of Figure 3.15 with the applied potential corrected for the IR-drop.

In Figure 3.19, it is clear that for potentials more negative of -0.65 V up to the transition potential, log R_p^{-1} is linear with an inverse slope of 64 mV decade^{-1}. For potentials more positive than -0.65 V, a deviation from linearity is seen. This deviation is due to the contributions from the cuprous ion formation reaction and back (dissolution) reaction [32]. Also interesting to note is that at low chloride concentrations, a return to a linear slope at more negative potential is somewhat apparent (5 and 10 ppm solutions). This is hard to determine however, as there are only a few data points with which to see this trend. (See below for further discussion.)

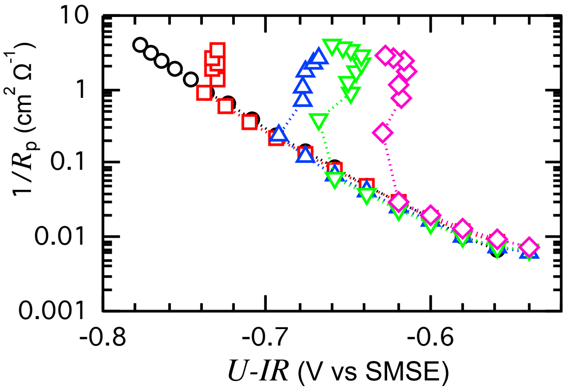

Figure 3.19: Re-plot of Figure 3.17 with the applied potential corrected for the IR-drop.

Figure 3.20 is a semi-logarithmic plot of the steady-state current densities measured during the impedance measurements versus the applied potential corrected for the IR-drop (note that since the current in this range is negative, what is actually plotted is the logarithm of the absolute value). It is also clear from this plot that there is a sharp transition at the same potential from one state to another. It is not surprising that the transition involves a large increase in the current, as Figure 3.19 shows a large drop in the charge transfer resistance at the transition potential. A drop in resistance will lead to an increased current at the same potential. For potentials negative of -0.65 V, the current density displays a Tafel slope of 78 mV decade^{-1}, close to the slope of 64 mV decade^{-1} obtained from $\partial U / \partial \log R_p^{-1}$ in Figure 3.19.

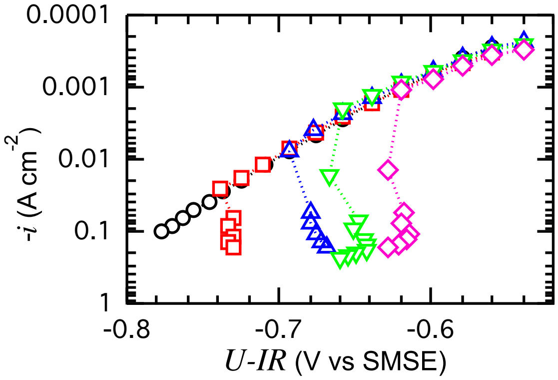

Figure 3.20: Semi-logarithmic plot of the current density versus the applied potential corrected for the IR-drop. Note that the current has a negative sign, so the plot is of the logarithm of the absolute value. The data is from the MA solution containing 25 mL L^{-1} suppressor and chloride concentrations of 50 ppm (○), 30 ppm (□), 15 ppm (△), 10 ppm, (▽), and 5 ppm (◇).

An even more interesting finding is seen in Figures 3.21a and 3.21b, which are log-log plots of R_p^{-1} versus the magnitude of the current density for the MA solution with various (5 – 50 ppm) chloride concentrations. Combining equations (3.11) and (3.12), and noting that a linear plot can be represented by $y = mx$, gives:

$$I_0 \frac{\alpha n F}{RT} e^{\left(\frac{-\alpha n F}{RT}\right)\eta} = m\left(I_0 e^{\left(\frac{-\alpha n F}{RT}\right)\eta} \right) \tag{3.19}$$

Simplifying the equation and rearranging terms gives:

$$m = \frac{\alpha n F}{RT} \tag{3.20}$$

where

$$\frac{F}{RT} = 38.9 \text{ V}^{-1} \tag{3.21}$$

From the figures, it is clear that the plot is linear and has a slope of approximately 40 V^{-1} at low current densities, i.e. before a transition occurs. This corresponds to $\alpha n \approx 1.0$. This is very reasonable for a two-electron reaction with a charge transfer coefficient of 0.5. At higher current densities, after the transition, the slope of the line changes to 18 - 24 V^{-1}, a significant difference.

Note that the transition is not seen for the solution with 50 ppm chloride, and occurs at progressively lower current densities (lower overpotentials) with decreasing chloride concentration. This lower slope indicates a significant change in the mechanism of copper deposition, and could have various explanations. First, it is possible that the rate-limiting step of the reaction transitions to a one-electron reaction, (n = 1). Alternately, it could indicate a significant change in the charge transfer coefficient of the reaction between the two states. Or it could be a combination of the two.

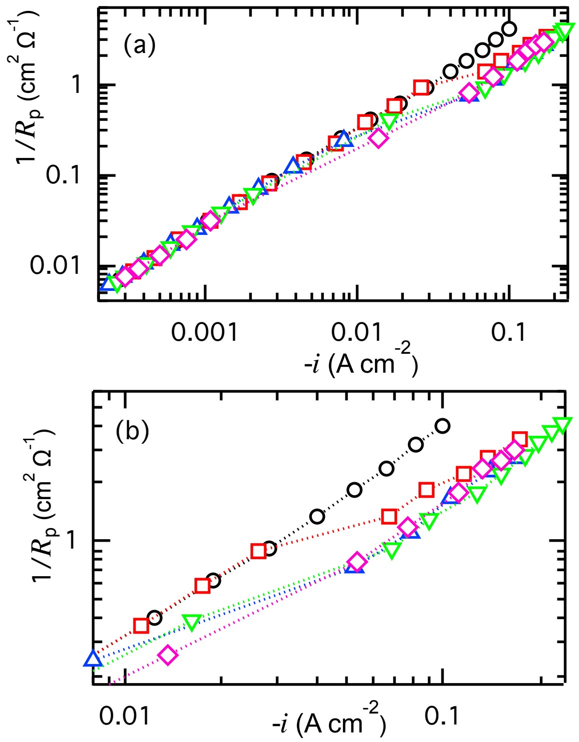

Figure 3.21: Log-log plot of the inverse of the area corrected R_P versus the current density. Note that the current has a negative sign, so the plot is of the logarithm of the absolute value. The data is from the MA solution containing 25 mL L^{-1} suppressor and chloride concentrations of 50 ppm (○), 30 ppm (□), 15 ppm (△), 10 ppm, (▽), and 5 ppm (◇).

From Figures 3.15 – 3.21, it should be clear that there is a significant transition in the electrochemical reaction taking place at the electrode. From Figure 3.20, it is clear that copper deposition is occurring both positive and negative of the transition potential. Using results in the MA solution with 30 ppm chloride as an example, the current density at the transition potential is 26 mA cm^{-2}. The plating rate for copper deposition, v, as a function of the steady-state current density, i_{SS}, assuming that 100% of electrons flowing across the interface are involved in the reduction of copper, is given by the following equation:

$$v = \frac{i_{SS} m_{Cu}}{nF\rho_{Cu}} \tag{3.22}$$

where m_{Cu} is the atomic mass of copper (63.546 g mol^{-1}), ρ_{Cu} the density of copper (8.96 g cm^{-3}), n the number of electrons required for the reduction of cupric ions to metallic copper, and F is Faraday's constant (96,485 C mol^{-1}). This leads to a plating rate of 9.56 x 10^{-7} cm s^{-1} or 9.56 nm s^{-1} for a current density of 26 mA cm^{-2}. These are not trivial deposition rates, nor are currents of this magnitude a result only of parasitic side reactions. Only the reduction of copper to a metal can account for these currents.

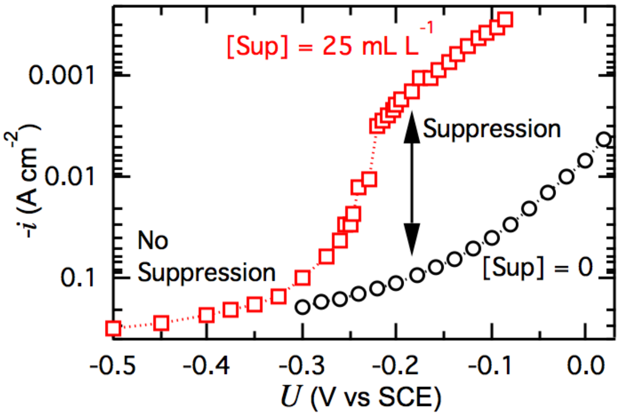

Figure 3.22: Semi-logarithmic plot of the current density versus the applied potential for MA solutions containing 30 ppm Chloride both with (□) and without (○) the suppressor. Note that the current has a negative sign, so the plot is of the logarithm of the absolute value.

Figures 3.22 and 3.23 show the transition from a suppressed to an unsuppressed state. In both plots, the MA solution with 30 ppm Cl$^-$ is shown, both with (□) and without (○) suppressor. Figure 3.22 is a semi-log plot of the (negative of the) current plotted versus potential (note that the reference electrode was a SCE for these experiments). In the solution without suppressor, the current increases at very low overpotentials. In the solution with suppressor, the current is initially much lower at a given potential, indicating the effect of the suppressor. After the critical potential, the current quickly rises to the level of the solution without suppressor, indicating that the suppressing effects of the suppressor are no longer occurring.

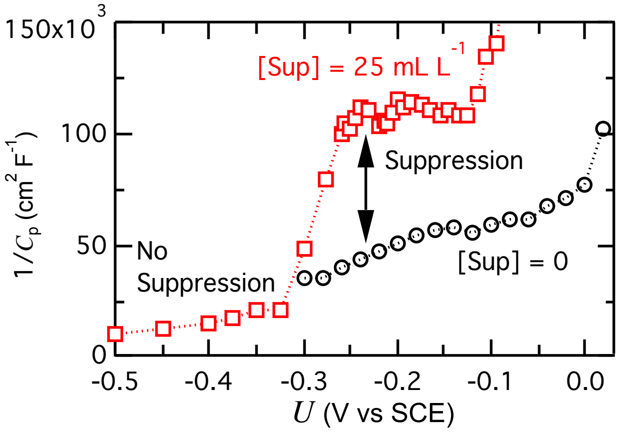

Figure 3.23: Plot of the inverse of the area corrected C_P at different applied potentials in MA solutions 30 ppm chloride both with (□) and without (○) the suppressor.

Figure 3.23 shows this as well, but clearly adds the detail of a change in surface state. It is a plot of the inverse of the capacitance versus the potential (again with a SCE RE). Recall from Chapter 2 that the inverse of the capacitance is analogous to d, the distance separating two plates of a parallel plate capacitor. As discussed previously, the presence of an organic adsorbate can manifest itself in this manner. The difference in between the solution without suppressor and that with it is striking. Even more so is the sharp transition in the capacitance in the solution with suppressor after the critical potential to a value similar to that seen in the solution without suppressor. This is very clear evidence that the suppressor is on the surface during conditions of suppression, and desorbs when the system transitions to a state of non-suppression.

At this point it is clear that the system is undergoing a transition from a suppressed to unsuppressed state at the critical potential. The change in the interfacial capacitance of the system is the most telling piece of evidence to indicate what is going on at the copper-electrolyte interface at this transition potential. Recall from Chapter 2 that the interfacial capacitance can be modeled as a parallel plate capacitor separated by a distance d. This distance, the OHP, is usually assumed to be on the order of a solvated ion, about 0.5 nm. In copper sulfate solutions containing chloride and a long-chain polyether molecule, copper deposition is suppressed at current densities in which electroplating normally takes place (15 mA cm^{-2}), and the polyether molecule has been shown to adsorb to the surface of the copper surface [36], and effect shown for other halides bromine and iodine as well [220, 221]. The presence of a large adsorbed organic molecule at the surface has been shown significantly decrease the capacitance [179, 180], partly due to the increased separation, d, between the surface and the charges in solution, and the change in the dielectric constant from that of water to that of the organic adsorbate [182].

Therefore, the most likely explanation is that at the critical potential, the suppressor, necessary for suppression and known to adsorb to the surface during copper deposition, is desorbing, leading to both the large increase in capacitance and deposition rate. The results from the 5 ppm chloride solution are also telling. The suppressor adsorbs to the copper surface only in the presence of chloride. For a small chloride ion concentration of 5 ppm, the suppressor complex is not able to fully adsorb, and the capacitance, as shown in Figure 3.18, is higher because of that. For chloride concentrations of 10 ppm or more, the suppressor is able to fully adsorb. However, it should be noted that Figures 3.19 and 3.20 make clear that the current is still fully suppressed under these conditions.

In Chapter 4, I will discuss an alternate method of determining the critical potential at which the suppressor desorbs, but before that, a bit more discussion on the EIS measurements are in order. The EIS data were analyzed using the Randles equivalent circuit and although it provides a very good fit under most situations, it needs to be made clear that it is only a partial model of the system under investigation. Most tellingly is the change in the fitting parameters when the system transitions from suppression to non-suppression with the desorption of the suppressor. This is most evident in Figure 3.12, but confirmed in Figure 3.16.

As previously mentioned above, there is a noticeable decrease in the series resistance obtained from the fit that clearly coincides with the transition from suppression to non-suppression. Though only on the order of 1 Ω (~9%), it is a real effect, and R_S transitions to a different but constant value. Something similar is seen in Figure 3.16 for the value of *n* obtained from the CPE. These two effects, when taken in tandem, should be a clear indicator that the model circuit used to fit during suppression is not as valid after the suppressor has desorbed from the surface. Fits of this data were not as good as that obtained in the suppressed region. This could indicate that the copper reduction mechanism has shifted. Further study on this may be warranted, as researchers in the future may be able to use this transition and vary the solution and experimental parameters to determine the exact method of copper reduction on either side of the critical potential.

Further evidence that the Randles equivalent circuit is a simplified model of the interface can be seen in Figure 3.24. It is a Nyquist plot of the impedance data taken in the MA solution with 45 ppm chloride and 25 mL L^{-1} suppressor at -0.35 V (vs. SCE). The frequency was scanned from 100 kHz to 0.01 Hz. Scanning to very low frequencies

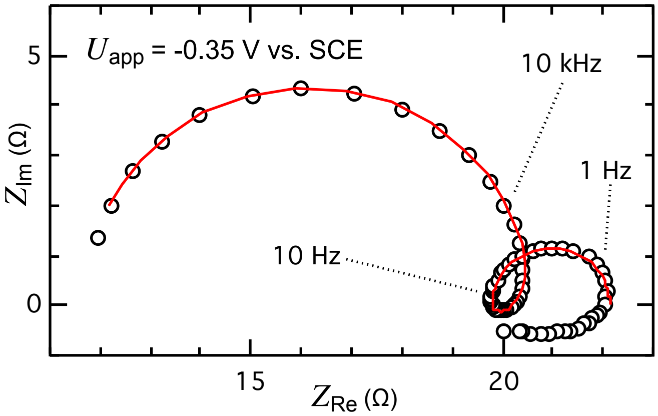

Figure 3.24: Nyquist plots of MA solution containing 25 mL L^{-1} suppressor and 45 ppm chloride at an applied potential of -0.35 V (vs. SCE). Both experimental data (○) and best fit (**solid red line**) are shown. The data has not been corrected for the electrode area.

shows a low frequency loop. A scan under the same conditions sweeping the frequency from 0.01 Hz to 100 kHz (i.e., from low to high instead of the standard high to low) produced nearly identical results, indicating that the additional low frequency loop is not an experimental artifact, but is in fact a real response of the system. This has been shown in other copper sulfate solutions that contain chloride and a branch chained polyether [111]. The effect has been ascribed to the presence of the accelerator [222], although this is clearly not the case since it is seen here in solutions that do not contain either SPS or MPSA. Interestingly, this same feature was seen in other solutions containing metal cations in a divalent state [111, 223-226]. In these cases, the authors ascribed the inductive loop to the ability of the dissolution reaction to proceed via different reaction pathways. Figure 3.25 is a representation of a possible equivalent circuit model for copper-electrolyte interface under investigation. It differs from the circuit proposed in the literature [227] due to the exchange of an adsorption capacitor with the inductor, L. The solid line in Figure 3.24 is a fit to the experimental data using the equivalent circuit in Figure 3.25 with the following circuit element parameters:

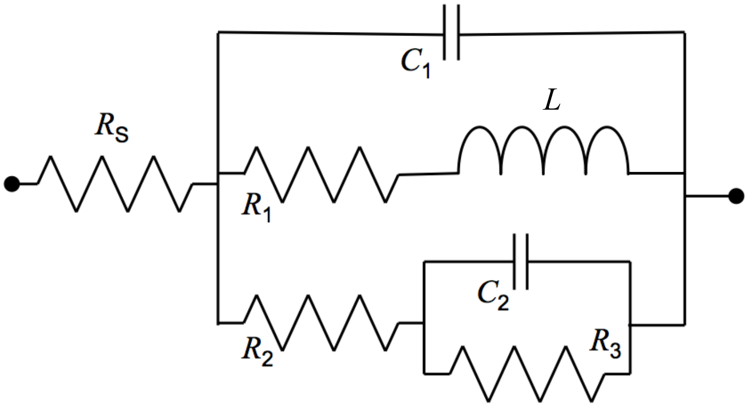

Figure 3.25: Equivalent circuit used to provide the fit to the data shown in Figure 3.24.

Table 3.3

R_S (Ω)	R_1 (Ω)	R_2 (Ω)	R_3 (Ω)	C_1 (μF)	n_1	C_2 (F)	n_2	L (H)
11.61	81	9.1	3.0	0.72	0.974	3.5×10^{-2}	0.98	1.1×10^{-2}

Note that both values for the exponent of the CPE are very close to 1, which would normally indicate a very good fit to the data. However, when fitting to the circuit, is important to realize that the values obtained from the best fit do not necessarily correspond to real phenomena. An inductance on the order of 0.01 H is very large, and is hard to explain if it were a real inductance. More likely is that it is a pseudo-inductance, a manifestation of relaxation and adsorption reactions taking place on the metal surface. Under AC conditions, these reactions would manifest themselves mathematically in the impedance data as very similar to an inductor. This is different than the model for the double layer capacitance, which is very similar to a real world capacitor. EIS has the potential to help researchers understand the processes occurring during copper deposition, but one must be careful when developing models to ensure that they retain a basis in reality.

One particular phenomenon that does not readily lend itself to representation via a simple circuit element is diffusion. Figure 3.26 is a Nyquist plot of the MA solution with 45 ppm chloride both with (□) and without (○) rotation of the working electrode at an applied potential of -0.22 V (vs. SCE). Two things are immediately obvious. First, the loop is much larger for the solution without convection, indicating a much higher charge transfer resistance at the same potential. This is easily understood if one considers the fact that the rotation of the RDE creates a large flux of solution (and hence cuprous ions) to the electrode surface, leading to a higher current (and lower resistance) for a given potential. The second obvious thing is the behavior of the impedance at low frequencies. Without rotation, the measured impedance continues to increase as the frequency decreases. This is indicative of a Warburg impedance, which represents the response of a system under mass transfer control. By analyzing this response, physical parameters of the system, such as the diffusion coefficient can be determined. To do this, we must begin by analyzing the system

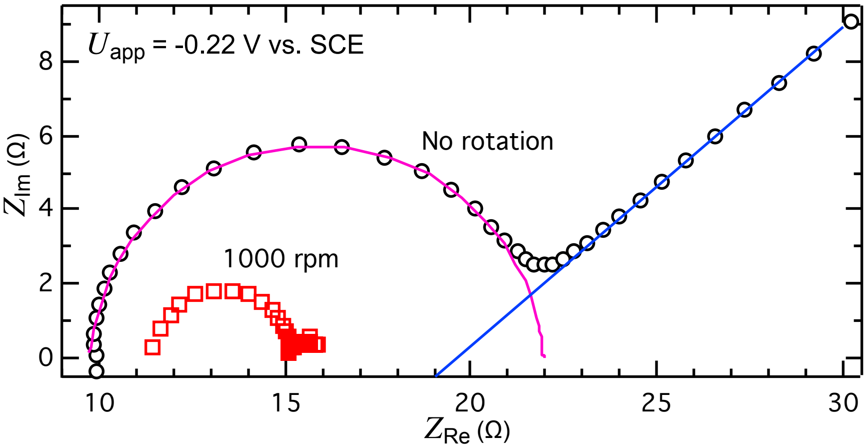

Figure 3.26: Nyquist plots of the MA solution with 45 ppm chloride at an applied potential of -0.22 V (vs. SCE). Rotation rates of 1000 (□) and 0 (○) rpm are shown. The fit of a simple Randles circuit is shown (**solid magenta line**), as is a linear extrapolation of the impedance response at low frequencies (**solid blue line**).

as if the low frequency response was not present, i.e. as a Randles circuit without any influence from diffusion. The magenta line is the best fit, and gives values for the elements as follows: R_S = 9.74 Ω, R_P = 12.2 Ω, C_P = 3.53 μF, and n = 0.962. The Warburg coefficient, σ, for a reaction involving n electrons, is given by:

$$\sigma = \frac{RT}{An^2F^2D^{1/2}\sqrt{2}} \cdot \left(\frac{1}{c_\mathrm{O}^*} + \frac{1}{c_\mathrm{R}^*} \right) \tag{3.23}$$

where A is the area of the electrode, D is the diffusion coefficient and c_i^* is the bulk concentration of the oxidants and reductants. For a Warburg impedance, the slope of the data at low frequencies should be 1. The blue line in Figure 3.26 is a linear fit of the data at low frequencies, but displays a slope of 0.85, below the expected value, which has been seen by other researchers [128]. An alternate method of determining σ is from the slope of the graph of the real part of the impedance vs. the inverse of the square root of the angular impedance (Z_Re vs. $\omega^{-1/2}$). The slope of this line (not shown) was found to be 82.7 Ω $s^{-1/2}$. Strictly speaking, the Warburg impedance is only applicable when both the oxidants and reductants are solution soluble species. If we assume that the response we are measuring is the reduction of cupric ions to an intermediate (solution soluble) cuprous species, we obtain a value for the diffusion coefficient of 3.57 x 10^{-6} cm^2 s^{-1}, which is very similar to previous published values [111, 228].

Chapter 4

From the result presented in Chapter 3, it is clear that there is a distinct transition during copper deposition from a state of suppression to one of non-suppression. It is also clear that the transition from suppression to non-suppression involves the desorption from the surface of the suppressor molecule, which is most likely adsorbed to the copper surface in a reaction mediated by chloride, and possibly copper(I). The desorption occurs at a critical potential that was shown to be a function of chloride concentration as well as overall bath composition, which will henceforth be referred to as the Vereecknen Potential, U_V, after the researcher who first proposed investigating it quantitatively.

This chapter will cover two main topics. The first is an attempt to better determine the value of U_V. As will be discussed below, EIS is not the best technique to determine it. Second, a wide range of bath chemistries will be investigated to determine the dependence of U_V on the concentrations of the various solution species. Though EIS was initially used, another technique, Pseudo Steady State Voltammetry (PSSV) will be investigated to see if it can provide superior resolution of U_V.

EXPERIMENTAL

All experiments were carried out at room temperature in a conventional three-electrode cell located in a Faraday cage to minimize stray electric and magnetic fields. The counter electrode was separated from the working electrode compartment with a porous glass membrane. The working electrode was a polished platinum rotating disk electrode (RDE) (Metrohm Model 628-1) with an area of 0.071 cm^2. The platinum electrode was mechanically polished to 50 nm alumina particles, cleaned in 30 vol% HNO_3 for not less than two minutes, and then rinsed with de-ionized water (18 MΩ).

The reference electrode was a saturated mercury/mercury sulfate electrode (SMSE) (U_{eq} = 0.65 V vs. SHE) and was connected to the cell via a Luggin capillary placed about 0.5 cm from the working electrode. All potentials are reported with respect to the saturated mercury sulfate electrode, unless indicated otherwise. The counter electrode consisted of platinum gauze, cleaned in 30 vol.% HNO_3 prior to experiments.

Solutions were prepared from $CuSO_4 \cdot 5H_2O$ (99.7%, J. T. Baker), H_2SO_4 (Assay, Baker), and deionized water (18 MΩ). Three base solutions were employed: 0.27 M $CuSO_4$ and 1.78 M H_2SO_4, (pH = -0.1) henceforth referred to as the high acid (HA) solution; 0.55 M $CuSO_4$ and 0.46 M H_2SO_4 (pH = 0.6) or medium acid (MA) solution; and 0.63 M $CuSO_4$ and 0.1 M H_2SO_4 (pH = 1.3) or low acid (LA) solution. HCl (Assay, Baker) was added to the base solutions to give Cl^- concentrations up to 50 ppm (50 ppm = 50 mg L^{-1} = 1.4 mM Cl^-). A suppressor (Shipley C2001; Rohm and Haas) was added to the base solution in concentrations up to 25 mL L^{-1}. Prior to each experiment, the platinum disk electrode was immersed in the solution and a copper film was deposited at 1 mA (14 mA cm^{-2}) for 90 s. The thickness of the copper film was about 0.5 µm. All experiments were performed at a rotation rate of 1000 rpm.

PSEUDO STEADY STATE VOLTAMMETRY

Figure 4.1 shows current-voltage curves for a Cu disk electrode in MA solution with chloride concentrations of 50 (black), 30 (red), 15 (blue), 10 (green), and 5 (magenta) ppm at a scan rate of 0.5 mV s^{-1}. These slow scan rate current-voltage curves also show the transition from suppression to non-suppression at the Vereecken potential, U_V. As was seen in the previous chapter, U_V shifts progressively to more negative potentials with increasing chloride concentration. However, as described in the previous chapter, it is necessary to correct the potential for IR-drop to determine the actual interfacial potential when desorption occurs.

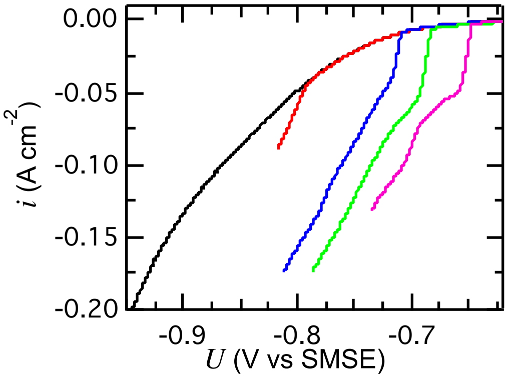

Figure 4.1: Current-potential curves in MA solution containing 25 mL L^{-1} suppressor and chloride ion concentrations of 50 (**black**), 30 (**red**), 15 (**blue**), 10 (**green**), and 5 (**magenta**) ppm. Scan rate = 0.5 mV s^{-1}.

For each solution, Impedance Spectroscopy measurements were conducted to determine the series resistance of the cell. The data were fit to a Randle's circuit to determine R_{S}. The R_{S} value used to correct for the IR-drop was an average of the values obtained a different potentials, with a focus on the value obtained near U_{V}.

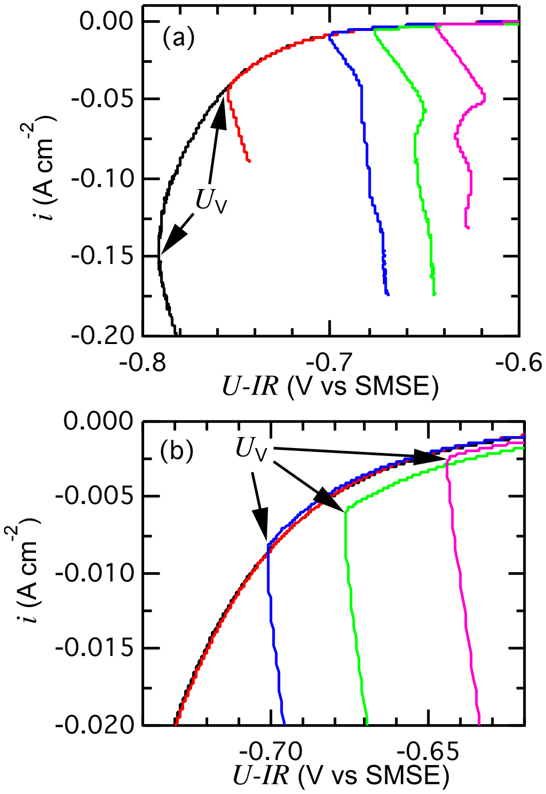

Figure 4.2: Re-plot of Figure 4.1 with the potential corrected for the IR-drop. Vereecken potentials were determined by using the negative most potential reached, as indicated on the chart. Curves are for the MA solution containing 25 mL L^{-1} suppressor and chloride ion concentrations of 50 (**black**), 30 (**red**), 15 (**blue**), 10 (**green**), and 5 (**magenta**) ppm. Scan rate = 0.5 mV s^{-1}.

Figures 4.2a and 4.2b show just such plots (Figure 4.2b is simply a zoomed in graph to get a better view of the transition at low chloride solutions). The five scans from Figure 4.1 have been corrected to take into account the IR-drop. The Vereecken potential was taken as the negative most potential in the scan. As can be seen from the plots, it is relatively easy to determine the potential by visual inspection, unlike EIS, which was more subjective. In addition, determining the Vereecken potential from PSSV experiments instead of EIS leads to a more precise value. This is obvious when one thinks about the state of the copper surface as the potential is slowly swept negative. Starting the scan near the OCP ensures that the surface is in a fully suppressed state, and remains so as the potential is slowly swept negative [105]. At no time prior to U_{V} is the surface perturbed in such a manner as to desorb the suppressor from the surface. Because deposition is always suppressed, there is no risk of encountering the hysteresis effects that are common in this system when the potential is swept negative of U_{V}. This may not be the case with EIS measurements, where a sinusoidal potential perturbation of 10 mV is applied, which at some point will be close enough to U_{V} to induce a (small) hysteresis effect. Also, the very slow scan rate of 0.5 mV s^{-1} should negate any of the transient effects of cyclic voltammetry, and keep the system in quasi steady-state for the duration of the experiment right up to U_V. In the figures, the sharp transition allows for unambiguous determination of the critical potential, corresponding to the most negative potential under which the system is fully suppressed. It should be noted that the apparent negative slope in the CV at potentials "negative" of U_V are due to the change in the charge-transfer (parallel) resistance associated with the transition from suppression to non-suppression.

Figure 4.3 is a comparison of the Vereecken potentials obtained from EIS measurements (solid markers) and PSSV (open markers) for the HA (○●), MA (□■), and LA (△▲) solutions with different chloride concentrations. It is clear from the figure that the values obtained from the two different methods are in good agreement with each other. However, there are some systematic differences that are worth discussing. For every solution combination investigated, U_V as determined by PSSV is more positive than U_V determined by EIS. This further reinforces the point discussed above, that PSSV is a better technique to determine U_V because the potential is slowly scanned to more negative potentials while the system remains in a state of suppression. As soon as the system transitions from suppression to non-suppression, the current increases and a hysteresis effect is induced.

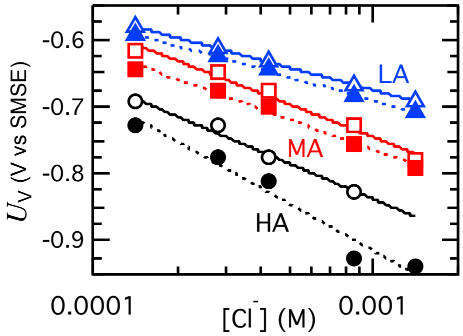

Figure 4.3: Plot of the Vereecken potentials as a function of chloride ion concentration for the HA (○●), MA (□■) and LA solutions (△▲). The values were obtained from EIS (solid markers) and PSSV (open markers) measurements.

Next, it is clear that in all three base solutions, U_V is strongly dependent on the chloride concentration. For the LA solution, the slopes, $\partial U_V/\partial \log[\mathrm{Cl}^-]$, obtained from EIS and PSSV are -111 (▲) and -117 mV (△) decade^{-1}, respectively. For the MA solution, the corresponding slopes are -163 (■) and -150 mV (□) decade^{-1}. In the HA solution, there is less agreement in the slopes, which are -176 (●) and -232 (○) mV decade^{-1}. In addition to providing a more accurate means of measuring U_V, PSSV has the added benefit of being relatively quick from an experimental standpoint, as it does not require detailed analysis as is the case with the EIS spectra, and therefore allows the testing of a large number of solution combinations rapidly.

Figure 4.4 shows the dependence of U_V on the suppressor concentration over a range of chloride concentrations in the LA solution. Chloride concentrations of 50 (●), 30 (■), 15 (▲), 10 (▼), 5 (◀), 3 (○), 1.5 (□), and 1 (△) ppm are shown, along with fits (solid lines) to the corresponding data (the dashed lines are not fits and included to help show the trend in that particular chloride concentration). It is readily apparent that U_V is only weakly dependent on the suppressor concentration over most chloride ion concentrations, as long as the concentration is above a threshold value of about 1 ml L^{-1}. In general, U_V shifts to more negative values with increasing suppressor and chloride ion concentration. For chloride concentrations in the range 1 – 10 ppm, the slopes $\partial U_V/\partial \log[\mathrm{Sup}]$ vary between -2 and -5 mV decade^{-1}. For chloride concentrations above 10 ppm, a similar weak dependence of U_V on suppressor is seen in the higher suppressor concentration range. The slope of the dependence seems to increase with increasing chloride concentration, but with only two data points, it is very difficult to say definitively that this is the case. It is evident that U_V at low suppressor concentrations is more positive than expected based on extrapolation of the curves.

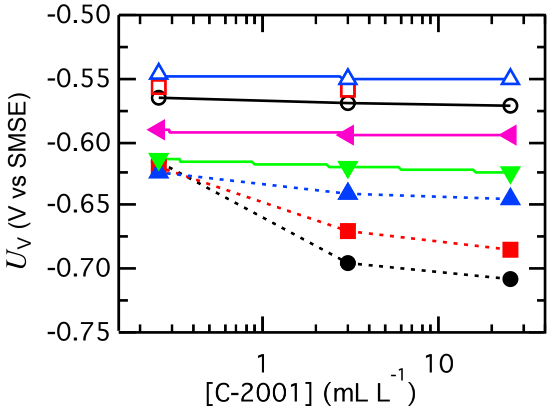

Figure 4.4: Plot of the Vereecken potentials as a function of suppressor concentration in the LA solution for chloride ion concentrations of 50 (●), 30 (■), 15 (▲), 10 (▼), 5 (◀), 3 (○), 1.5 (□), and 1 (△) ppm. The solid lines are the least squares fits for those concentrations; the dashed lines only show the trend for that concentration by connecting adjacent points.

The behavior of the system at low suppressor concentrations requires more discussion. At 0.25 mL L^{-1} the suppressor concentration is too low to effectively inhibit deposition and increasing the chloride concentration leads to an increase in the rate of copper deposition and hence a *positive* shift in U_V [100]. This seems to be a range in which the accelerating effects of chloride are overpowering the inhibitive effects of the suppressor, most likely due to the very low concentration of suppressor in the bath [32, 91]. This point will be further discussed in Chapter 5 when a more detailed model of the adsorbed suppressor-chloride complex is put forth.

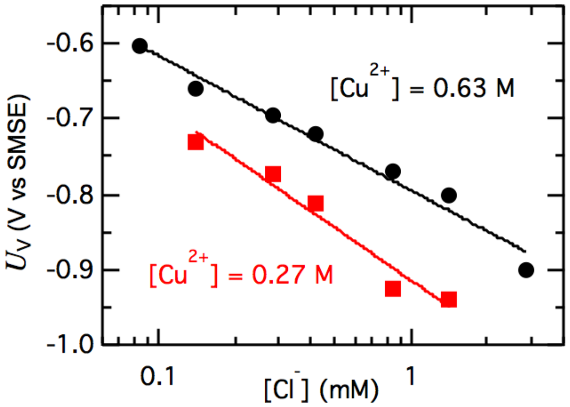

Figure 4.5: Plot of the Vereecken potentials as a function of chloride ion concentration for solutions containing 0.63 M Cu^{2+} (●) and 0.27 M Cu^{2+} (■). The solid lines are the least squares fits for those solutions.

So far, the Vereecken potential has been shown to be a function of chloride and suppressor concentration. Figure 4.5 is a semi-logarithmic plot of U_V with respect to the chloride concentration for two solutions with different copper concentrations. Both solutions contain 25 mL L^{-1} suppressor and a sulfuric acid concentration of 1.78 M, but the copper ion concentrations are 0.63 M (●) and 0.27 M (■). Note the wider than normal range of chloride ion concentrations in the 0.63 M Cu solution, in which the range from 3 - 100 ppm is plotted. Increasing the copper concentration from 0.27 M to 0.63 M results in a positive shift of about 80 mV at low to medium chloride concentrations and corresponds to a cupric ion dependency $\partial U_V/\partial \log[Cu^{2+}]$ of about 220 mV $decade^{-1}$.

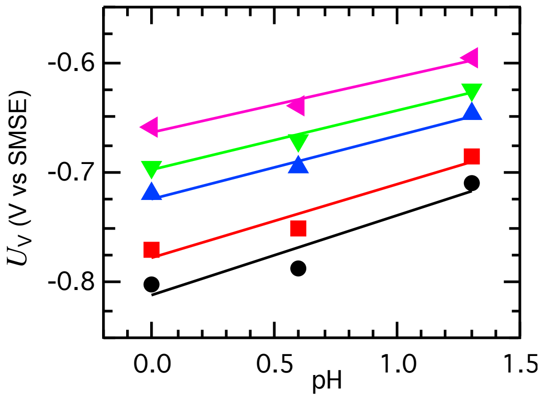

Figure 4.6: Plot of the Vereecken potentials as a function of pH in copper sulfate solutions containing 25 mL L^{-1} suppressor and chloride ion concentrations of 50 (●), 30 (■), 15 (▲), 10 (▼), and 5 (◀) ppm. The solutions with pH = 0 and pH = 1.3 had a copper concentration of 0.63M. The solution with pH = 0.6 was the MA solution, and had a copper concentration of 0.55 M, and values for U_V were adjusted +5 mV to correct for the different copper concentration (0.55 M in the MA solution) based off the fit in Figure 4.5.

One final dependence that has not yet been looked at is that of the pH. Figure 4.6 is a plot of the Vereecken potentials as a function of pH for solutions with 25 mL L^{-1} suppressor and chloride ion concentrations of 50 (●), 30 (■), 15 (▲), 10 (▼), and 5 (◀) ppm. The solutions with pH = 0 and pH = 1.3 had copper concentrations of 0.63M. The solution with pH = 0.6 was the MA solution, and had a copper concentration of 0.55 M. To make U_V strictly comparable to the other solutions plotted here, it needs to be corrected for the different copper concentration. As seen in Figure 4.5, U_V has a dependence on the copper concentration of 220 mV decade^{-1}; this results in a +5 mV shift for U_V, for which the plotted values have been corrected. It is clear from the figure that the U_V is dependent on the pH of the solution, and shifts to more positive potentials in solutions with a higher pH. The solid lines are fits of the data, which yield slopes between 70 and 80 mV pH^{-1} depending on chloride ion concentration. However, it should be noted that for all five chloride concentrations, U_V is a few millivolts below where it would be expected it to be if fits were perfectly linear. This could either be an artifact of the correction based on the copper concentration, or an indication that U_V is not fully linear over the entire range [105].

From Figures 4.5 and 4.6, it is clear that there is a dependence of U_V on the copper concentration and pH of the solution. Looking back at Figure 4.3, it is clear that the differences seen between the HA, MA, and LA solutions are a composite effect of the changes in both the copper concentration and the pH.

In the plating industry there is a trend to move towards plating baths with low acid and high copper content for improved wafer-scale uniformity and wafer throughput [229, 230]. However, these results illustrate that increasing pH and cupric ion concentration result in a positive shift in the Vereecken potential and hence a narrower potential range for suppression during copper deposition. This explains the slower feature filling observed for low acid baths [230]. Other work investigating the effect of pH on superfilling [231] found no difference in the strength of the suppressor, but this study did not look at regions outside those typically found during plating, so were operating in a range in which the suppressor was always adsorbed to the copper surface.

Over the course of this study, a wide range of solution combinations were investigated. Figure 4.7 is a chart of the Vereecken potentials for all investigated solutions, with the solution parameters. The following chapter will discuss a thermodynamic model of the adsorbed complex using the data obtained here to determine the nature of the complex.

U_V (V vs. SMSE)	[Cu^{2+}] (M)	[Cl$^-$] (ppm)	[Sup] (mL L^{-1})	pH	U_V (V vs. SMSE)	[Cu^{2+}] (M)	[Cl$^-$] ppm	[Sup] (mL L^{-1})	pH
-0.709	0.629	50	25	1.3	-0.770	0.275	30	0.25	0.1
-0.685	0.629	30	25	1.3	-0.752	0.275	15	0.25	0.1
-0.646	0.629	15	25	1.3	-0.734	0.275	10	0.25	0.1
-0.624	0.629	10	25	1.3	-0.699	0.275	5	0.25	0.1
-0.595	0.629	5	25	1.3	-0.678	0.629	50	250	1.3
-0.940	0.275	50	25	0.1	-0.643	0.629	30	250	1.3
-0.925	0.275	30	25	0.1	-0.611	0.629	15	250	1.3
-0.812	0.275	15	25	0.1	-0.588	0.629	10	250	1.3
-0.774	0.275	10	25	0.1	-0.573	0.629	5	250	1.3
-0.729	0.275	5	25	0.1	-0.548	0.629	3	250	1.3
-0.791	0.551	50	25	0.6	-0.469	0.629	1.5	250	1.3
-0.755	0.551	30	25	0.6	-0.480	0.629	1	250	1.3
-0.701	0.551	15	25	0.6	-0.717	0.629	100	250	1.3
-0.677	0.551	10	25	0.6	-0.716	0.629	150	250	1.3
-0.644	0.551	5	25	0.6	-0.532	0.629	3	25	1.3
-0.695	0.629	50	3	1.3	-0.569	0.629	3	3	1.3
-0.670	0.629	30	3	1.3	-0.566	0.629	3	0.25	1.3
-0.640	0.629	15	3	1.3	-0.559	0.629	1.5	3	1.3
-0.619	0.629	10	3	1.3	-0.556	0.629	1.5	0.25	1.3
-0.594	0.629	5	3	1.3	-0.551	0.629	1	25	1.3
-0.615	0.629	50	0.25	1.3	-0.550	0.629	1	3	1.3
-0.619	0.629	30	0.25	1.3	-0.547	0.629	1	0.25	1.3
-0.623	0.629	15	0.25	1.3	-0.902	0.629	100	25	0
-0.614	0.629	10	0.25	1.3	-0.802	0.629	50	25	0
-0.591	0.629	5	0.25	1.3	-0.771	0.629	30	25	0
-0.882	0.275	50	3	0.1	-0.719	0.629	15	25	0
-0.869	0.275	30	3	0.1	-0.694	0.629	10	25	0
-0.782	0.275	15	3	0.1	-0.660	0.629	5	25	0
-0.747	0.275	10	3	0.1	-0.603	0.629	3	25	0
-0.703	0.275	5	3	0.1	-0.623	0.629	1.5	25	0
-0.767	0.275	50	0.25	0.1	-0.624	0.629	1	25	0

Figure 4.7: Chart of every Vereecken potential found for every solution combination investigated. All values for U_V were determined using PSSV.

Chapter 5

From the data presented in previous chapters, it is clear that a suppressor-chloride complex is adsorbed on the copper surface and is desorbed at potentials more negative than U_{V}. The Vereecken potential was shown to be logarithmically dependent on $[\mathrm{Cl}^-]$, $[\mathrm{Cu}^{2+}]$, [Sup], and $[\mathrm{H}^+]$ implying that all are involved in the formation of the complex that suppresses copper deposition. Before formulating a general expression for the formation of this complex, it is helpful to review the formation of the CuCl film formed by the complexation of Cu^+ in the presence of small chloride concentrations.

In the presence of millimolar concentrations of chloride ions in acidic copper sulfate solutions without any other additives, an insoluble cuprous chloride film will form on the copper surface [65, 91]. This film is formed under open-circuit conditions due to the comproportionation reaction of copper (thus forming free cuprous ions) and at low overpotentials by the stepwise reduction of cupric ions to the adsorbed CuCl intermediate reaction {5.1}, which may be reduced further to metallic copper, reaction {5.2}:

$$\mathrm{Cu}^{2+} + \mathrm{Cl}^- + e^- \leftrightarrow \mathrm{CuCl}_{ads} \qquad U^0_{\mathrm{Cu}^{2+}/\mathrm{CuCl}_{ads}} = 0.538 \text{ V (SHE)} \qquad \{5.1\}$$

$$\mathrm{CuCl}_{ads} + e^- \leftrightarrow \mathrm{Cu} + \mathrm{Cl}^- \qquad U^0_{\mathrm{CuCl}_{ads}/\mathrm{Cu}} = 0.137 \text{ V (SHE)} \qquad \{5.2\}$$

From reactions {5.1} and {5.2}, it follows that there is a potential range between the two equilibrium potentials where the CuCl film is thermodynamically stable. At more negative potentials ($U < U_{\mathrm{eq}}(\mathrm{CuCl}_{\mathrm{ads}}/\mathrm{Cu})$), the CuCl is reduced further to metallic copper. Thus the formation of the copper-chloride-suppressor complex is analogous to the formation of $\mathrm{CuCl}_{\mathrm{ads}}$.

To determine the equilibrium potential for an electrochemical reaction, it is useful to review the basics of the thermodynamics of electrochemical reactions. The Gibbs free energy change, ΔG, for a reversible reaction is given by:

$$\Delta G = -nFU_{\mathrm{rxn}} \qquad (5.1)$$

When all the substances are at unit activity, we have an expression for the standard free energy change of the reaction:

$$\Delta G^0 = -nFU^0_{\text{rxn}} \tag{5.2}$$

For a general reaction in which x moles of oxidants are reduced to y moles of reductants via a reaction involving n moles of electrons:

$$x\text{Ox} + ne^- \leftrightarrow y\text{Red} \qquad \{5.3\}$$

the free energy change of reaction {5.3} is given by:

$$\Delta G = G^0 - \text{R}T\ln\frac{a^y_{\text{Red}}}{a^x_{\text{Ox}}} \tag{5.3}$$

where R is the molar gas constant (8.414 J mol^{-1} K^{-1}), T is the temperature, a_{Ox} is the activity of the oxidants, and a_{Red} is the activity of the reductants. Substituting equations (5.1) and (5.2) into equation (5.3) gives the expression for the equilibrium potential:

$$U_{eq} = U^0_{eq(\text{Ox/Red})} + \frac{\text{R}T}{nF}\ln\frac{a^y_{\text{Red}}}{a^x_{\text{Ox}}} \tag{5.4}$$

where F is Faraday’s constant (96,485 C). Equation (5.4) is known as the Nernst equation. For the purposes of this work, it will be more useful to use a base-10 logarithm instead of the natural logarithm. Multiplying by the factor of 2.303, and inserting numerical values for the constants gives an expression for the Nernst equation (at 298K):

$$U_{eq} = U^0_{eq(\text{Ox/Red})} + \frac{0.0592}{n}\log\frac{a^y_{\text{Red}}}{a^x_{\text{Ox}}} \tag{5.5}$$

From the Nernst equation, the equilibrium potential for a complex or adsorbate such as CuCl can be calculated from the equilibrium potentials for the free metal ions (e.g. $U_{\text{eq}}(\text{Cu}^{2+}/\text{Cu}^+)$ and $U_{\text{eq}}(\text{Cu}^+/\text{Cu})$) and the complexation constant or solubility product (e.g. $K_{\text{S}} = [\text{Cu}^+][\text{Cl}^-]$ [87]. For the formation of CuCl:

$$\text{Cu}^+_{aq} + \text{Cl}^-_{aq} \leftrightarrow \text{CuCl}_{ads} \qquad \{5.4\}$$

The solubility product for this reaction $K_{\text{S}} = [\text{Cu}^+][\text{Cl}^-] = 3.3 \times 10^{-7}\ \text{M}^2$. The reduction of cupric ions to metallic copper can be written as:

$$\mathrm{Cu}^{+}_{aq} + e^{-} \leftrightarrow \mathrm{Cu} \qquad \{5.5\}$$

The equilibrium potential for reaction {5.5} is given by:

$$U_{eq} = U^{\circ}_{eq(\mathrm{Cu}^{+}/\mathrm{Cu})} + 0.0592{*}\log[\mathrm{Cu}^{+}] \quad U^{0}_{eq(\mathrm{Cu}^{+}/\mathrm{Cu})} = 0.521\ \mathrm{V\ (SHE)} \qquad (5.6)$$

For the case where cuprous ions are complexed with chloride, substitution of [Cu^{+}] from the expression for K_{S} into (5.6) gives:

$$U_{eq} = U^{\circ}_{eq(\mathrm{Cu}^{+}/\mathrm{Cu})} + 0.0592{*}\log K_{\mathrm{S}} - 0.0592{*}\log[\mathrm{Cl}^{-}] \qquad (5.7)$$

The equilibrium potential for the electrochemical reduction of CuCl {5.2} is given by:

$$U_{eq} = U^{\circ}_{eq(\mathrm{CuCl}_{ads}/\mathrm{Cu})} - 0.0592{*}\log[\mathrm{Cl}^{-}] \qquad (5.8)$$

From equations (5.7) and (5.8), it can be seen that:

$$U^{\circ}_{eq(\mathrm{CuCl}_{ads}/\mathrm{Cu})} = U^{\circ}_{eq(\mathrm{Cu}^{+}/\mathrm{Cu})} + 0.0592{*}\log K_{\mathrm{S}} \qquad (5.9)$$

Using a similar approach, an equation for the Vereecken potential as a function of the various solution species can be determined. We can begin with a general expression for the formation of a complex involving the suppressor ether groups (-OEt-), chloride, and Cu^{+}, which is given by:

$$\mathrm{Cu}^{+} + k(-\mathrm{OEt}-) + b\mathrm{Cl}^{-} \leftrightarrow \left(\mathrm{Cu(I)}(-\mathrm{OEt}-)_{k}\mathrm{Cl}_{b}\right)^{(1-b)} \qquad \{5.6\}$$

where k is the number of suppressor ether groups involved in adsorption and b is the number of chloride ions per cuprous ion that are in the adsorbed complex. From the experimental results shown in Chapter 4, it is clear that cupric and hydrogen ions are also involved in the adsorption of the suppressor complex. It has previously been shown [97] that the ether groups in PEG also complex with cupric ions:

$$\mathrm{Cu}^{2+} + m(-\mathrm{OEt}-) \leftrightarrow \mathrm{Cu(II)}(-\mathrm{OEt}-)^{2+}_{m} \qquad \{5.7\}$$

In the case of PEG, m = 4. Equation {5.7} can be substituted into equation {5.6}. However, the charge isn't balanced, but this can be corrected by adding H^{+} ions. After doing so, the total reaction can be described by:

$$\begin{aligned} &k\mathrm{Cu(II)}\left(-\mathrm{OEt}-\right)_m^{2+} + \mathrm{Cu}^+ + b\mathrm{Cl}^- + c\mathrm{H}^+ \leftrightarrow \\ &\left[\mathrm{Cu(II)}_{k-d}\left(-\mathrm{OEt}-\right)_{km}\mathrm{Cu(I)Cl}_b\mathrm{H}_c\right]^{1-b+c+2(k-d)} + d\mathrm{Cu}^{2+} \end{aligned} \tag{5.8}$$

Reaction {5.8} is written only for an individual ether group. Suppressor molecules are made up of multiple ether groups per molecule (e.g. for a 3400 MW PEG, there would be 77 of them). To describe the actual complex measured in the previous experiments, it is necessary to rewrite equation {5.8} for the complete suppressor molecule $\mathrm{HO((CH_2)_xO)_yH}$:

$$\begin{aligned} &\frac{1}{a}\left[\mathrm{Cu(II)}_w\mathrm{HO}\left((\mathrm{CH}_2)_x\mathrm{O}\right)_y\mathrm{H}\right]_{aq}^{\frac{2w}{a}+} + \mathrm{Cu}^+ + b\mathrm{Cl}^- + c\mathrm{H}^+ \leftrightarrow \\ &\left(\mathrm{Cu(II)}_{(w/a)-d}\left(\mathrm{HO(CH_2)}_x\mathrm{O})_y\mathrm{H}\right)_{1/a}\mathrm{Cu(I)Cl}_b\mathrm{H}_c\right)_{ads} + d\mathrm{Cu}^{2+} \end{aligned} \tag{5.9}$$

where y is the number of ether groups per molecule and x is the number of methylene groups per oxygen (for PEG x = 2 and for PPG x = 3; for a copolymer x is between 2 and 3; because the suppressor used in this study was proprietary, the number has not been disclosed). As with the CuCl case discussed above, a solubility product for this reaction can be written. For reaction {5.9}, it is:

$$K_\mathrm{S} = \frac{[\mathrm{HO((CH)_2)}_x\mathrm{O)}_y\mathrm{HCu(II)}_w]^{1/a}[\mathrm{Cu}^+][\mathrm{Cl}^-]^b[\mathrm{H}^+]^c}{\left[\mathrm{Cu}^{2+}\right]^d} \tag{5.10}$$

The equilibrium potential for copper in the presence of the cuprous complex can be determined from combination of equation (5.10) and the equilibrium potential for the Cu^+/Cu couple. The approach is the same as that for the CuCl system discussed above. The equilibrium potential for the Cu^+/Cu couple is given by reaction {5.1}.

However, we can simplify the model a bit by recognizing that the cupric ion concentration in solution is much greater than that of the suppressor concentration. This allows us to make the simplification that $[\mathrm{HO((CH_2)_xO)_yHCu(II)_w}] \approx [\mathrm{Sup}]$. Substitution of the free cuprous ion concentration, $[\mathrm{Cu}^+]$, from equation (5.10) into equation (5.1) gives:

$$U_\mathrm{eq} = U^\mathrm{o}_{\mathrm{eq(Cu^+/Cu)}} + 0.0592\left(\log K_\mathrm{S} - b\log[\mathrm{Cl}^-] - \frac{1}{a}\log[\mathrm{Sup}] + c*\mathrm{pH} + d\log[\mathrm{Cu}^{2+}]\right) \tag{5.11}$$

Equation (5.11) describes the potential where the adsorbed cuprous chloride suppressor complex is reductively desorbed from the surface, and corresponds to the Vereecken potential, U_{V}. When deriving the Nernst equation for a complexation reaction, the equilibrium constant is usually incorporated into the standard equilibrium potential. Equation (5.11) is then reduced to:

$$U_{\mathrm{V}} = U_{\mathrm{V}}^{\circ} + 0.0592\left(-b\log[\mathrm{Cl}^{-}] - \frac{1}{a}\log[\mathrm{Sup}] + c * \mathrm{pH} + d\log[\mathrm{Cu}^{2+}]\right) \tag{5.12}$$

where $U_{\mathrm{V}}°$ is the standard equilibrium potential for the reduction of the adsorbed Cu(I) complex given by the reaction:

$$\begin{gathered}\left(\mathrm{Cu(II)}_{[(w/a)-d]}[\mathrm{HO(CH_2)}_x\mathrm{O)}_y\mathrm{H}]_{1/a}\mathrm{Cu(I)Cl}_b\mathrm{H}_c\right)_{ads} + d\mathrm{Cu}^{2+} + e^{-} \leftrightarrow \\ \mathrm{Cu} + \tfrac{1}{a}\mathrm{Cu(II)}_w\mathrm{HO((CH_2)}_x\mathrm{O)}_y\mathrm{H} + b\mathrm{Cl}^{-} + c\mathrm{H}^{+}\end{gathered} \qquad \{5.10\}$$

Equation (5.12) gives the dependence of U_{V} on the suppressor, chloride ion, cupric ion concentrations and the pH. From the dependencies of the U_{V} discussed in Chapter 4, values for the coefficients a, b, c, and d, in reactions {5.9} and {5.10} can be estimated.

There are two ways to go about doing so. The first is to use all the data presented in Figure 4.7 and fit it to equation (5.12) using a least squares fitting method. This has the advantage of being most accurate, in that it incorporates all given information. However, this method makes the assumption that the suppressor complex adsorbed to the surface and it's desorption mechanism is the same in all circumstances and under all conditions. This may not be the case. This method will be discussed in greater detail below.

A simple method for determining the values is to hold all other experimental parameters constant, and vary a single parameter to see how it affects U_{V}. For example, from Figure 4.4, the dependence of U_{V} on the suppressor concentration was shown to be between -2 and -5 mV decade^{-1}. All other experimental parameters were held constant. Substituting these values into equation (5.12) leads to the conclusion that $a \approx 20 - 30$. This implies that there are approximately 25 ether groups in the suppressor available for complexing for every cuprous moiety.

Figure 4.6 shows a pH dependence of +70 to +80 mV decade^{-1}, values that are very consistent over the range of chloride concentrations studied. These slopes suggest a value of $c \approx 1$, indicating one proton per cuprous ion is incorporated in the chloride suppressor complex to partially compensate for the excess negative charge introduced by the chloride ions.

The Vereecken potential's dependence on the cupric ion concentration was found to be $\partial U_V/\partial \log[Cu^{2+}]$ = 220 mV. From this slope, it can be determined that $d \approx 3 - 4$. This implies that three to four cupric ions are released from the aqueous Cu(II)-ether complex during adsorption, and it countered by the addition one cuprous ion. It is possible that the cupric ion does not actually detach from the suppressor complex, but is instead reduced to a cuprous ion upon adsorption to the surface via the comproportionation reaction. This would release a second cuprous ion into the solution.

It is interesting to note that the results indicate that a total of four ions (1 Cu^+, 2 Cl^-, and 1 H^+) are displacing three to four Cu^{2+} ions. In other words, the number of occupied sites on the suppressor complex remains about the same before and after adsorption to the copper surface. From reaction {5.7} and reference [97] (about one Cu^{2+} ion per 4 ether groups), and from the observation that about 25 ether groups are associated with each cuprous ion in the complex, it can be concluded that many cupric ions remain associated with the adsorbed complex.

Figure 4.5 shows the results for two separate series of experiments in which solutions with two different copper concentrations were investigated across a range of chloride concentrations. Slopes between -100 and -200 mV decade^{-1} are seen, although it is clear that the chloride dependence seems to depend on the copper concentration. These slopes for the dependence on chloride imply values for $b \approx 2 - 3$, suggesting that there are 2 or 3 chloride ions per cuprous ion in the complex. The involvement of multiple chloride ions is consistent with the fact that the molecule used in this study is one of the strongest known suppressors. For weaker suppressors, such as PPG, it was previously found that $b \sim 1$ [36].

Another method for determining values for the coefficients of equation (5.12) is to conduct least squares fitting. A fit was done using all 62 values from Figure 4.7. The following values were obtained: a = 0.068, b = 1.84, c = 1.32, and d = 3.05; the adjusted r^2 was 0.883. These values imply that the suppressor complex is comprised of 2 chloride ions, 3 cupric ions, and 1.3 hydrogen ions. It also implies that there are about 15 (a^{-1} = 14.7) EtO groups per copper ion in the complex.

However, a glance at Figure 4.4 shows that the method of fitting the data from every experiment may not be the most appropriate means of determining the coefficients. At very low suppressor concentrations (0.25 mL L^{-1}), increasing the chloride ion concentration beyond 10 ppm does not shift the Vereecken potential to more negative values as predicted by the model, but in fact shifts it more positive at very high chloride concentrations. It is most likely that in this range, there is no adsorption of the suppressor complex that inhibits copper deposition in the same manner as in other systems. Therefore, it is inappropriate to include the experimentally determined Vereecken potentials in the model. To that end, the three values from the LA solution with a suppressor concentration of 0.25 mL L^{-1} and chloride ion concentrations of 50, 30 and 15 ppm were excluded from a second fitting attempt (the solutions are highlighted in red in Figure 4.7).

The second fitting had a very similar adjusted r^2 of 0.884, indicating the overall validity of the fitting process. The individual fitting parameters were: a = 0.136, b = 1.93, c = 1.35, and d = 3.19. With the exception of a, most values were very similar to the previous fit. However, a nearly doubled, implying that there are only about 7 (a^{1} = 7.37) EtO groups per copper ion in the complex. Also of note is the *t-stat* for a obtained in the two fitting scenarios. In the former case, it was 0.808, in the latter, 1.51. *T-stat* values below 2 are usually indicative of a fitting variable whose value is not statistically significant to the fit. In this case, it is probably a result of the very weak dependence of U_V on the suppressor concentration, and the small range over which accurate data was recorded. However, the near doubling of the *t-stat* from one fitting to the next provides a qualitative indication that the fit, especially in regards to a has improved. Also, the value of seven EtO groups per copper ion is similar to results found by other researchers [105].

Knowing the individual values for the species that make up the suppressor complex allows for the determination of the solubility constant of the suppressor complex, K_S, from equation (5.10) using the Vereecken potential and the concentrations for each solution investigated. To begin, one simplification can be made. The suppressor concentrations used in this study were in the range of 1-100 mM. But, due to the proprietary nature of the Shipley additive, a precise value is not given. However, this is not important for the following, and is not necessary to calculate K_S. To understand why this is, note that in equation (5.11), the logarithm of the suppressor concentration is multiplied by the inverse of a. Since a is large, that term can be neglected in equation (5.11). Equation (5.11) then reduces to:

$$U_{\mathrm{eq}} = U^{\mathrm{o}}_{\mathrm{eq(Cu^+/Cu)}} + 0.0592\left(\log K_{\mathrm{s}} - b\log[\mathrm{Cl^-}] + c * \mathrm{pH} + d\log[\mathrm{Cu^{2+}}]\right) \tag{5.13}$$

Up to this point in the discussion, ideal solution behavior has been assumed. Furthermore, all pHs used in the calculations have been the measured value, which by definition takes into account the activity of the hydrogen ion. In equations where $[\mathrm{H^+}]$ is written, $\{\mathrm{H^+}\}$ is actually being discussed. In addition, the very low chloride concentration used in this study ensures that its activity coefficient is close to one, and we can make the valid assumption that $\{\mathrm{Cl^-}\} \approx [\mathrm{Cl^-}]$.

For copper, however, the situation is more complicated [50, 232]. Because the copper concentration is relatively high, the assumption cannot be made that the activity coefficient is close to 1. To work with these solutions, more care must be taken in understanding the effects of the solution composition. Debye-Hückel theory [233] states that the activity coefficient, γ_i, of an ion in solution is give by:

$$\ln\gamma_i = -\frac{z_i^2 e^3 N_{\mathrm{A}}^{1/2}}{4\pi(\varepsilon\varepsilon_0 k_{\mathrm{B}} T)^{3/2}}\sqrt{\frac{I}{2}} \tag{5.14}$$

which is frequently reduced to:

$$\log\gamma_i = -Az_i^2\sqrt{I} \tag{5.15}$$

where the constant A has a value for water at room temperature (298K) of 0.509 $\mathrm{mol^{-1/2}\ kg^{1/2}}$. However, Debye-Hückel theory is only valid for solutions with dilute ionic strength, typically taken to be less than 1 mM. For higher ionic strengths, various models have been developed, including the Davies Equation, the Pitzer Equations and specific ion interaction theory. However, these all suffer from the drawback that one must accurately calculate the ionic strength of the solutions. For the multi-component solutions used in semiconductor metallization, these problems are not trivial. Though values for disassociation constants exist in the literature, trying to determine an accurate solution speciation from them using mathematical means is fraught with difficulty [234]. For this reason, some researchers have taken to measuring the cupric ion activity in copper plating solutions directly [235]. For solutions containing 1 M H_2SO_4 and a $CuSO_4$ concentration that ranged from 150 – 750 mM, the activity coefficient of the cupric ion was found to be around 0.1. For solutions containing 0.1 M H_2SO_4 and the same range of $CuSO_4$ concentrations, the activity coefficient was around 0.3. Unfortunately, no attempt was made to measure the cupric ion activity at the time the experiments in this study were conducted. However, the similarity of the solutions used here to those in the reference allows us to use estimates in the range of 0.1 to 0.3 for this work.

Recalling that $U_{\mathrm{eq}}°(\mathrm{Cu}^+/\mathrm{Cu}) = -0.129$ V and rearranging terms in equation (5.13) gives:

$$\log K_{\mathrm{S}} = \frac{U_{\mathrm{V}} + 0.129}{0.0592} + b\log[\mathrm{Cl}^-] - c*\mathrm{pH} - d\log\left(\gamma_{\mathrm{Cu}^{2+}}[\mathrm{Cu}^{2+}]\right) \tag{5.16}$$

The value of the activity coefficient for the cupric ions will be varied according to the solution of interest. For example, for the LA solution (0.1 M H_2SO_4 and 0.63 M $CuSO_4$), a value of $\gamma_{\mathrm{Cu}} = 0.3$ can be used.

The value for log K_{S} was calculated for each experiment according to equation (5.16) and plotted as a function of Cl^-, pH, and Cu^{2+} to check for the concentration independence. Figure 5.1 is a plot of -log K_{S} plotted as a function of chloride concentration for the range of solutions investigated. For the black circles (○) $b = 2$; for the red squares (□) $b = 3$. From the graph it is apparent that only for $b = 2$ is K_{S} independent of chloride concentration. For a value of $b = 3$, a 60 mV per decade chloride dependence was observed (indicating one too many Cl^- were assumed). It is therefore concluded that two chloride ions are involved in reaction {5.9}.

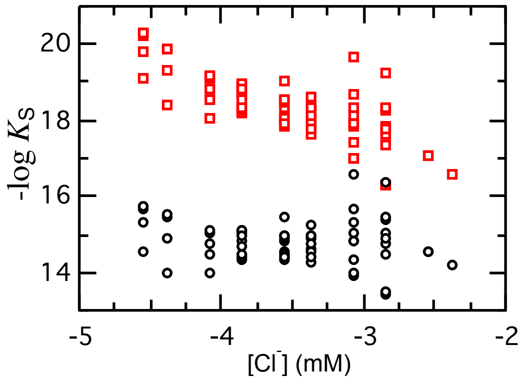

Figure 5.1: Plot of -log K_{S} plotted as a function of chloride concentration for the range of solutions investigated. Values were determined from equation (5.16); for the black circles (○) $b = 2$; for the red squares (□) $b = 3$.

As may be recalled from Figure 4.3, slopes larger than 120 mV decade^{-1} (b = 2) were found for MA and HA solutions. This is related to influence of the data at higher chloride concentrations, as we seen in Figure 4.4, and discussed at length earlier in this chapter. When ignoring these higher chloride concentrations, slopes of about 120 mV decade^{-1} were found in all cases.

In a similar manner, the other variables (c and d) can be confirmed by determining the value that produces values for K_S that are not dependent on the underlying variable. For the pH dependence, only a value of c = 1 gave a pH-independent value of log K_S. For d = 3, log K_S was independent of the cupric ion concentration. Thus, it can be concluded that the values of the coefficients are b = 2, c = 1, and d = 3. Using these values, the complete complexation reaction written for one suppressor molecule, and assuming 25 ether units per cuprous ion then becomes:

$$\begin{aligned}&\left(\mathrm{Cu(II)}_w\mathrm{HO}\left((\mathrm{CH_2})_x\mathrm{O}\right)_y\mathrm{H}\right)^{2w+}_{(aq)} + 25\mathrm{Cu}^+_{(aq)} + 50\mathrm{Cl}^-_{(aq)} + 25\mathrm{H}^+_{(aq)} \leftrightarrow \\ &\left(\mathrm{Cu(II)}_{(w-75)}\left(\mathrm{HO(CH_2)}_x\mathrm{O}\right)_y\mathrm{H}\right)\mathrm{Cu(I)}_{25}\mathrm{Cl}_{50}\mathrm{H}_{25}\Big)^{(w-4)+}_{ads} + 75\mathrm{Cu}^{2+}\end{aligned} \qquad \{5.10\}$$

The exact number of cupric ions, w, is unknown.

Figure 5.2 is a plot of the -log K_S calculated from all 62 solution combinations shown in Figure 4.7 with b = 2, c = 1 and d = 3. The average of the 62 values gives log K_S = -13.76 ± 1.03. However, the least squares fitting done above did not return integer values for all of the variables. The values plotted above imply that there are two chloride ions in the complex for every one cuprous ion. However, given the large nature of the suppressor molecule, and the fact there are 25 $CuCl_2H$ groups per molecule, it is entirely conceivable that the ratio of chloride to cuprous ions is not an integer value. The same applies for the hydrogen ions. As an example,

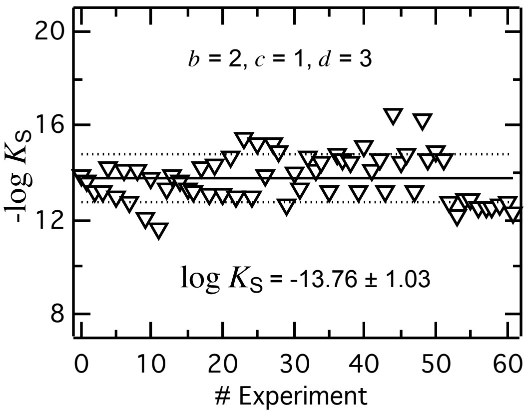

Figure 5.2: Plot of -log K_S calculated from all 62 solution combinations shown in Figure 4.7 with b = 2, c = 1 and d = 3. The average of the 62 values gives log K_S = -13.76 ± 1.03.

the best fit obtained above had b = 1.9 and c = 1.3. Using these numbers gives the following reaction:

$$\begin{gathered}\left(\mathrm{Cu(II)}_{w}\mathrm{HO}\left((\mathrm{CH}_2)_x\mathrm{O}\right)_y\mathrm{H}\right)^{2w+}_{(aq)} + 25\mathrm{Cu}^{+}_{(aq)} + 48\mathrm{Cl}^{-}_{(aq)} + 33\mathrm{H}^{+}_{(aq)} \leftrightarrow \\ \left(\mathrm{Cu(II)}_{(w-75)}\left(\mathrm{HO}(\mathrm{CH}_2)_x\mathrm{O}\right)_y\mathrm{H}\right)\mathrm{Cu(I)}_{25}\mathrm{Cl}_{48}\mathrm{H}_{33}\Big)^{(w-4)+}_{ads} + 75\mathrm{Cu}^{2+}\end{gathered} \quad \{5.11\}$$

Figures 5.3 and 5.4 are plots of –log K_S calculated using b = 2, c = 1.3 and d = 3 and b = 1.9, c = 1.3 and d = 3, respectively.

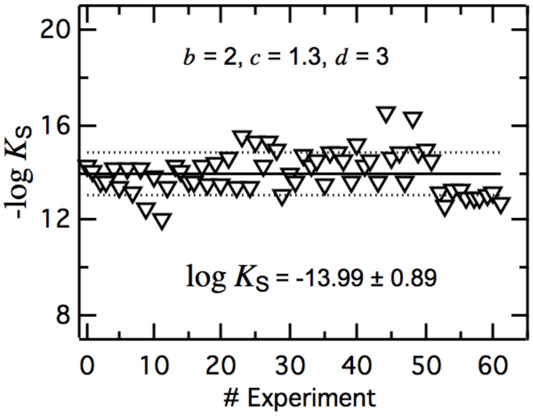

Figure 5.3: Plot of -log K_S calculated from all 62 solution combinations shown in Figure 4.7 with b = 2, c = 1.3 and d = 3. The average of the 62 values gives log K_S = -13.99 ± 0.89.

Some discussion points are in order at this point. First, it is not clear that the increased specificity of the values has made the model any more accurate. There is a degree of uncertainty in the values for the Vereecken potential, and it is hard to quantify how much. This is a result of the difficult nature of measuring its exact value for any given solution, as well as the correction for the IR-drop of the experimental setup. This spread is apparent in Figures 4.3 and 4.5 in particular. Because there is already some noise in the data, it is likely that very accurate models of the suppressor chloride complex will not provide an exact answer not because of a failure of the model, but because of the uncertainty in the measurements. As an example, it has been shown that correcting for the Ionic conductivity of the solution significantly improves the measured value of K_S [105].

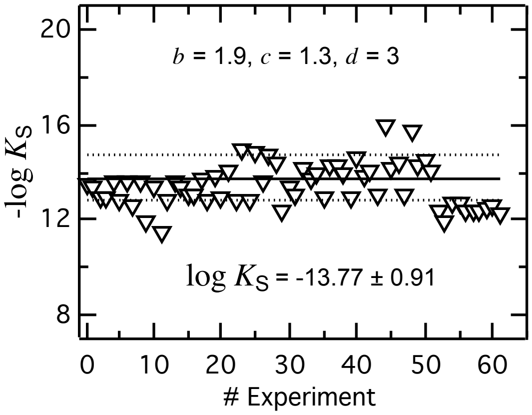

Figure 5.4: Plot of -log K_S calculated from all 62 solution combinations shown in Figure 4.7 with b = 1.9, c = 1.3 and d = 3. The average of the 62 values gives log K_S = -13.77 ± 0.91.

Second, from Figures 5.2 – 5.4, it is clear that small changes to the coefficients produced very small changes to the calculated values for K_S. Figure 5.5 is an overlay of the calculated values of -log K_S from all three sets of fitting parameters, and the average value and standard deviation (-13.72 ± 0.96). As is clear from the figure, the changes to the coefficients have only a small effect on individual values. This is a strong indication of the robustness of the model and lends credence to its overall conclusion. The extremely low value of the solubility constant illustrates the high stability of the adsorbed suppressor complex on the copper surface. For comparison, the logarithm of the solubility constant for CuCl formation is log K_S = -6.5, or only about half that of log K_S for the Cu(I)-Chloride-Suppressor complex.

From the value of K_S, and using equation (5.11), the value of $U_V°$ can be calculated for reaction {5.10}. It was found to be -0.916 V ± 54 mV (vs SMSE). Adjusting to SHE, it is -0.276 V ± 54 mv (vs. SHE).

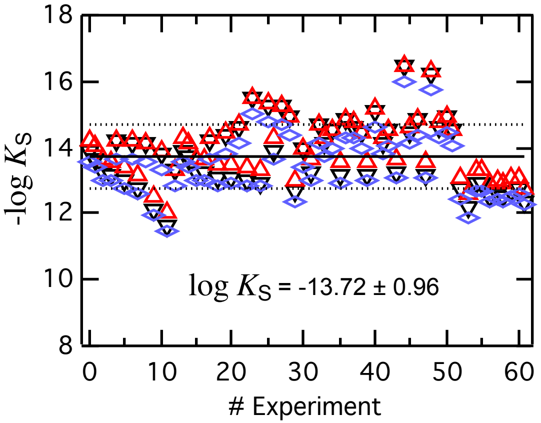

Figure 5.5: Plot of all calculated values of -log K_S from all three sets of fitting parameters.

It should be noted that the discussion above is based on a series of experiments that took place on rotating, planar surfaces. Ultimately, the solutions of interest, and the additives that go into them, are designed to produce their superfilling effects in deep trenches and vias. Under plating conditions, the concentrations of the various solution species are quite different in the trenches than at a flat surface or in the bulk solution [6, 29, 41, 46, 101, 236, 237]. For copper deposition into features such as trenches and vias, the local concentrations of Cu^{2+}, Cl^-, H^+, and the suppressor will determine the stability of the suppressor complex, and hence the degree of suppression of copper deposition. In addition, the non-planar geometry coupled with effects caused by IR-drop across the wafer from the terminal effect will create non-uniformity in the local deposition potential. This will also affect the stability of the suppressor complex.

Void-free filling is dependent on a number of factors. These include the differential coverage of the suppressor, accelerator, and leveler at the copper surface, in addition to the ability of the accelerator to displace the suppressor complex. According to the CEAC model of superfilling, the final factor is key. For researchers, knowing the energy required to displace the suppressor complex will allow them to build more accurate models to test future plating solutions and deposition parameters to better optimize trench and via filling. From equation (5.2), it is found that ΔG^0 = +26.1 kJ mol^{-1} for reaction {5.10}. As with the very negative log K_S, the positive value indicates that desorption of the suppressor complex is not spontaneous, and in fact requires a large amount of energy to accomplish. It is thus clear that the adsorption/desorption of the suppressor complex plays a crucial role in superfilling.

Chapter 6

Although it is of critical importance in superfilling, the role of the accelerator is currently poorly understood. It has long been known to affect the structure of copper deposits [238]. At this time, SPS is added to plating solutions in small quantities, whereby it leads to superfilling in solutions that also contain chloride and a suppressor [124, 239]. In the absence of either the accelerator or the suppressor, superfilling is not seen [45]. It is clear that superfilling is the result of a synergistic effect between the accelerator and suppressor complex, though the effects can be confused with that of the leveler [240]. Though SPS is the most common additive used as an accelerator, MPSA has been shown to behave similarly [35], as have other molecules of a similar structure [131]. Of particular interest is the mechanism by which it locally accelerates copper deposition. In the absence of other additives, in particular a suppressor complex, the accelerator actually suppresses copper deposition over the potential range of interest; voltammetry studies show that the copper reduction current is actually greater in acidified copper sulfate solutions that do not contain any additives than in solutions that contain SPS in amounts typical of plating baths that exhibit superfilling [32].

The complex nature of the accelerator has led researchers to suggest various mechanisms by which SPS accelerates copper deposition. The Curvature Enhanced Accelerator Coverage (CEAC) model posits that the accelerator physically displaces the suppressor from the surface over time, allowing for local acceleration of the copper plating. In plating baths containing both suppressor and accelerator, adsorption of the suppressor is more rapid than that of the accelerator [30]. But because adsorption of the suppressor (thiolate) - accelerator complex is stronger than adsorption of the suppressor-chloride complex, the accelerator irreversibly displaces the suppressor from the surface over time (the Cu-S bond energy is 274 kJ mol^{-1} [241]).

Although deposition on a surface with adsorbed accelerator is slower than on copper in an additive-free solution, it is still greatly enhanced compared to a surface on which the suppressor is adsorbed. Therefore, copper deposition in areas where the suppressor has been displaced by the accelerator will be faster than in areas where it has not. Broadly, this mechanism assumes that the accelerator is not a part of the chemical/electrochemical copper reduction mechanism.

Alternately, some researchers have postulated [32] that the full magnitude of acceleration can not be explained simply by the displacement of the suppressor by the accelerator. The copper ion is divalent, hence reduction to metallic copper involves a Cu(I) intermediate. At this point it is useful to recall the chemistry of copper plating solutions discussed in Chapter 2. (The first step of the reduction process, the reduction of cupric ions to cuprous ions is rate-limiting [72, 242, 243]. In the absence of complexing agents, the equilibrium concentration of cuprous ions is much lower than that of cupric ions. At equilibrium, the concentration of cuprous ions will be governed by the copper comproportionation reaction:

$$\mathrm{Cu} + \mathrm{Cu}^{2+} \leftrightarrow 2\mathrm{Cu}^{+} \qquad \{6.1\}$$

which has an equilibrium constant in acidified copper sulfate solutions of K_{Cu} = 5.6 x 10^{-7} ± 0.4 x 10^{-7} [61, 62], where K_{Cu} is defined as:

$$K_{\mathrm{Cu}} = \frac{\{\mathrm{Cu}^{+}\}^{2}}{\{\mathrm{Cu}^{2+}\}\{\mathrm{Cu}\}} \qquad (6.1)$$

The activity of a pure metal in solution is defined as a_{Cu} = 1. Substituting and rearranging the terms in equation (6.1) gives an expression for the cuprous ion concentration:

$$[\mathrm{Cu}^{+}]^{2} = K_{\mathrm{Cu}}[\mathrm{Cu}^{2+}] \qquad (6.2)$$

It can be inferred from equation (6.2) that a 0.55 M $CuSO_4$ solution in contact with metallic copper (e.g. a seed layer, or previously deposited copper), cuprous ions can form near the surface, and the solution should have a cuprous ion concentration of 0.55 mM. However, solutions open to the atmosphere contain dissolved oxygen, which can react with dissolved cuprous ions, oxidizing them to cupric ions. This prevents the reaction listed in reaction {6.1} from reaching equilibrium, and results in a cuprous ion concentration significantly below the equilibrium value. The addition of chloride to a solution leads the following complexation reaction:

$$\mathrm{Cu} + \mathrm{Cu}^{2+} + 2\mathrm{Cl}^{-} \leftrightarrow 2\mathrm{CuCl}_{\mathrm{ad}} \qquad \{6.2\}$$

which increases the Cu(I) concentration and also leads to the formation of a cuprous chloride film on the surface of metallic copper [87, 91]. Addition of the accelerator to the solution leads to the following complexation reaction:

$$\mathrm{Cu} + \mathrm{Cu}^{2+} + 2\mathrm{MPS} \leftrightarrow 2\mathrm{Cu(I)MPS}_{\mathrm{ad}} + 2\mathrm{H}^{+} \qquad \{6.3\}$$

where the adsorbed cuprous-MPS complex has the MPS in the deprotonated form [31, 244].

At this point, the reduction of hydrogen ions should be addressed.

$$2\mathrm{H}^{+} + 2e^{-} \leftrightarrow \mathrm{H}_2 \qquad U^{0}_{2\mathrm{H}^{+}/\mathrm{H}_2} = 0.0\ \mathrm{V\ (SHE)} \qquad \{6.4\}$$

The saturated mercury sulfate reference electrode (SMSE) used in these experiments has a potential of +0.64 V vs. the standard hydrogen electrode (SHE). Therefore, the standard potential of the SHE with respect to the SMSE is -0.64 V (vs. SMSE).

The accelerator reacts with the copper surface and copper ions in solution forming adsorbed cuprous-accelerator species via the following reactions [31, 244]:

$$4\mathrm{Cu} + \mathrm{SPS} \leftrightarrow 2\mathrm{Cu(I)MPS}_{\mathrm{ad}} + 2\mathrm{Cu}^{2+} \qquad \{6.5\}$$

$$2\mathrm{Cu}^{2+} + 4\mathrm{MPS} \leftrightarrow 2\mathrm{Cu(I)MPS}_{\mathrm{ad}} + \mathrm{SPS} + 4\mathrm{H}^{+} \qquad \{6.6\}$$

By combining reaction {6.1} and {6.6}, the following reaction for the adsorption of the accelerator to the surface can be obtained:

$$2\mathrm{Cu} + \mathrm{SPS} \leftrightarrow 2\mathrm{Cu(I)MPS}_{\mathrm{ad}} \qquad \{6.7\}$$

A similar reaction can be written for the adsorption of the suppressor mediated by the cuprous chloride on the copper surface discussed in the previous chapters [81, 83, 212]:

$$n\mathrm{CuCl}_{\mathrm{ad}} + \mathrm{Sup} \leftrightarrow \mathrm{CuCl}_{n}\mathrm{Sup}_{\mathrm{ad}} \qquad \{6.8\}$$

Three reactions can be written for various steps involved in the electrochemical reduction of copper:

$$\mathrm{Cu}^{2+} + e^{-} \leftrightarrow \mathrm{Cu}^{+} \qquad U^{0}_{\mathrm{Cu}^{2+}/\mathrm{Cu}^{+}} = -0.487\ \mathrm{V\ (SMSE)} \qquad \{6.9\}$$

$$\mathrm{Cu}^{+} + e^{-} \leftrightarrow \mathrm{Cu} \qquad U^{0}_{\mathrm{Cu}^{+}/\mathrm{Cu}} = -0.119\ \mathrm{V\ (SMSE)} \qquad \{6.10\}$$

$$\mathrm{Cu}^{2+} + 2e^{-} \leftrightarrow \mathrm{Cu} \qquad U^{0}_{\mathrm{Cu}^{2+}/\mathrm{Cu}^{+}} = -0.303\ \mathrm{V\ (SMSE)} \qquad \{6.11\}$$

Copper is known to form higher complexes with chloride. For a cuprous ion complexed with n

chloride ions, the general reaction is:

$$\mathrm{Cu}^{+} + n\mathrm{Cl}^{-} \leftrightarrow \mathrm{CuCl}_{n}^{(n-1)} \qquad \{6.12\}$$

For n = 1, the CuCl species is not soluble and forms on the copper surface (which is usually the source of the cuprous ion; Cu(I) has a solubility product log K_s = -6.73 and is present in only minute quantities in copper sulfate solutions not in contact with metallic copper. Higher complexes, such as $\mathrm{CuCl_2^-}$ and $\mathrm{CuCl_3^{2-}}$, have equilibrium constants of log β_2 = 5.38, log β_3 = 5.34, and log β_4 = 3.63 [88, 89]. The concentrations of these species are exceedingly low, and can safely be ignored for most practical purposes when working with electroplating solutions.

In addition to cuprous complexes with chloride, cupric ions also form chloride complexes, and the general reaction can be written as:

$$\mathrm{Cu}^{2+} + n\mathrm{Cl}^{-} \leftrightarrow \mathrm{CuCl}_{n}^{(n-2)-} \qquad \{6.13\}$$

For n = 1, the equilibrium constant log K_1 = 1.03. Higher order complexes have equilibrium constants of log β_2 = 1.60, log β_3 = 1.77, and log β_4 = 2.21 [88, 89]. As with the cuprous complexes, these higher order terms are negligible and can be ignored when working with real-world plating solutions.

For the electrochemical reduction of copper, the equilibrium potential of reaction {6.11} is given by the Nernst equation:

$$U_{\mathrm{Cu^{2+}/Cu}} = U^{0}_{\mathrm{Cu^{2+}/Cu}} + \frac{\mathrm{R}T}{2\mathrm{F}} \ln[\mathrm{Cu^{2+}}] \qquad (6.3)$$

where $U^{0}_{\mathrm{Cu^{2+}/Cu}}$ = -0.303 V (SMSE). For a solution with a cupric ion concentration of 0.55 M, the equilibrium potential of reaction {6.11} is modified using equation (6.3) and is -0.311 V (SMSE).

In addition, we can write two reactions for the electrochemical reduction of cuprous chloride species and one for the reduction of an adsorbed cuprous thiolate:

$$\mathrm{Cu}^{2+} + \mathrm{Cl}^{-} + e^{-} \leftrightarrow \mathrm{CuCl_{ad}} \qquad U^{0}_{\mathrm{Cu^{2+}/CuCl}} = -0.102 \text{ V (SMSE)} \qquad \{6.14\}$$

$$\mathrm{CuCl_{ad}} + e^{-} \leftrightarrow \mathrm{Cu} + \mathrm{Cl}^{-} \qquad U^{0}_{\mathrm{CuCl/Cu}} = -0.503 \text{ V (SMSE)} \qquad \{6.15\}$$

$$\mathrm{Cu(I)MPS_{ad}} + e^{-} + \mathrm{H^{+}} \leftrightarrow \mathrm{Cu} + \mathrm{MPS} \tag*{\{6.16\}}$$

The Nernst equation for reaction {6.4} is:

$$U_{2\mathrm{H^{+}/H_2}} = U^{0}_{2\mathrm{H^{+}/H_2}} - 2.303\frac{\mathrm{R}T}{2\mathrm{F}} * \mathrm{pH} \tag{6.4}$$

The measured pH of the solutions used here is 0.6, leading to an equilibrium potential of -0.658 V (SMSE). The oxidation reaction of water can be written as:

$$\mathrm{O_2} + 4\mathrm{H^{+}} + 4e^{-} \leftrightarrow 2\mathrm{H_2O} \qquad U^{0}_{\mathrm{H_2O/O_2}} = 0.589\ \mathrm{V\ (SMSE)} \tag*{\{6.17\}}$$

For reaction {6.17}, the Nernst equation is:

$$U_{\mathrm{H_2O/O_2}} = U^{0}_{\mathrm{H_2O/O_2}} - 2.303\frac{\mathrm{R}T}{4\mathrm{F}} * \mathrm{pH} \tag{6.5}$$

Given the measured pH of 0.6, reaction {6.17} has an equilibrium value of +0.598 V (SMSE). Figure 6.1 is a plot of the relevant equilibrium potentials plotted on the SMSE reference axis.

If the electrochemical deposition of copper proceeds through a two step mechanism, in which one step is significantly faster than the other, acceleration can be achieved by increasing the rate of the slow step, in this case, the initial reduction from cupric ions to cuprous ions.

Chloride has been shown to have this effect in acidified copper sulfate solutions [91]. Solutions with higher chloride ion concentrations exhibit a higher cathodic current at similar overpotentials, due to the accelerating effect of chloride. If the accelerator forms cuprous complexes, it is likely that this is one method by which it accelerates the deposition of copper. The presence of intermediates in the copper deposition reaction can be investigated *in situ* using a rotating ring-disk electrode (RRDE).

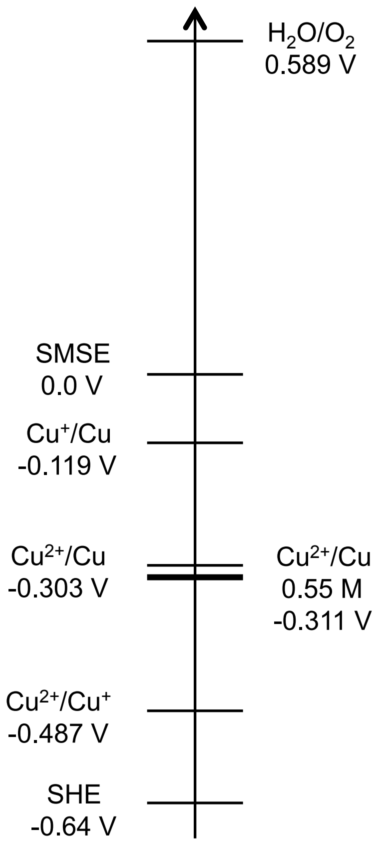

Figure 6.1: Various equilibrium potentials used in this chapter plotted on the SMSE scale.

Figure 6.2 shows an illustration of a RRDE, with an inner disk electrode with radius r_1, surrounded by a ring electrode with inner and outer radii r_2 and r_3, respectively. A plastic sheath electrically insulates the two rings from each other. Through the use of a bi-potentiostat, each electrode surface can be maintained at a potential independent of the other relative to the same reference electrode.

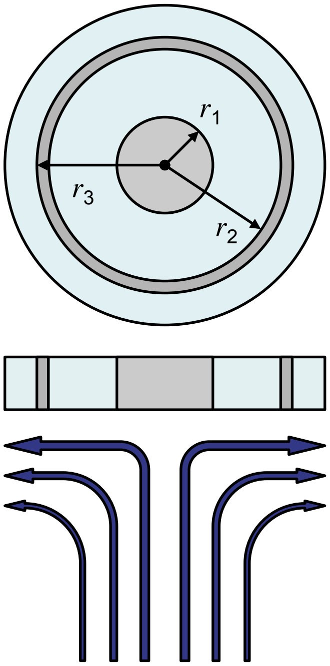

Figure 6.2: Top-down and side view of a Rotating Ring Disk Electrode. Disk and the ring electrodes (darker area) are electrically insulated from each other and can have independent potentials applied to them.

During rotation, transport at the surface of the disk acts upon the solution it is in contact with, forcing it outward radially from the center. Solution pushed out radially is replaced by solution drawn towards the disk from the bulk, in effect acting as a pump. The hydrodynamics of the solution are well understood, and a mathematical solution has been determined for the mass transport of species in the solution [245]. Species in solution acted upon by the disk have a well-defined path where they first pass over the inner disk before passing across the outer ring, as show in Figure 6.2. This allows for electroactive species to be probed sequentially at different potentials.

The RRDE is especially useful in the study of reactions that involve an intermediate [60, 186]. The flow of solution from the disk to the ring allows multi-step electron transfer processes to be separated into their constituent parts [186, 245]. For a two-step reaction, the intermediate following the first step may not have time to undergo the second step before being swept away from the disk by the forced convection of the rotation. However, proper experimental conditions may allow for its detection at the ring. Varying the rotation rate has the effect of varying the time an intermediate will take to travel from the disk to the ring. In this manner, the lifetime of reaction intermediates can be investigated.

In the case of copper deposition, partial reduction of the cupric species will leave free cuprous ions in solution [60]. Convection will cause them to travel towards the ring, where they can be detected. Figure 6.3 is a cross-sectional schematic representation of the RRDE; the solution is travelling radially away from the disk to the ring. Experimentally it is easier to apply a positive potential, oxidizing cuprous ions to cupric ions, than it is to apply a negative potential to reduce the ions to metallic form. There are two reasons for this; first, continued reduction to metallic copper leaves a deposit on the ring electrode, adversely affecting the results. Of greater importance, however, is the fact that reduction of cuprous ions at the ring would be masked by reduction of cupric ions; for a potential at which the reduction of Cu(I) occurs, the reduction of Cu(II) will also occur. Because all of the cupric ions are not reduced at the disk, a significant portion of them will remain in solution at the ring, where they will be reduced. In this case, the total current at the disk will consist of both reduction of the free cuprous ions of interest and the reduction of cupric ions.

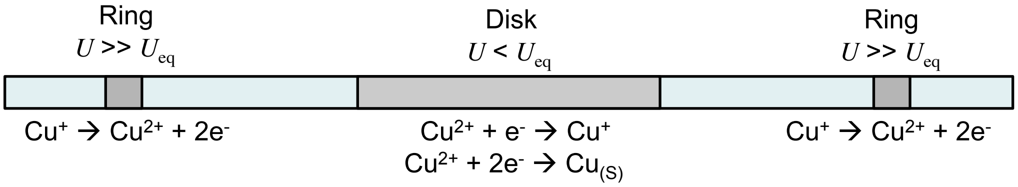

Figure 6.3: Close-up planar view of the RRDE with schematic representation of the applied potentials and the reactions occurring at each surface.

In the solution studied here, at the potential required to oxidize the cuprous species back to cupric ions, no other reactions take place. Therefore, the ring current can be assumed to be only from the presence of Cu(I). If a parasitic current is detected, and can be shown to be constant over the time frame of the experiment, then the total current can be corrected to arrive at a current resulting from the oxidation of copper.

To investigate the effects of SPS on the formation of Cu(I) complexes, it is also important to understand the electrochemical behavior of SPS over the potential range of interest, particularly the positive potentials at which the cuprous ions will be oxidized. If the potential at the ring is such that SPS undergoes an electrochemical reaction, leading to a detectable current, it may mask the oxidation current from the cuprous species. Previous work has detailed the response of SPS in the region of interest [32]. It has been shown that SPS oxidation does not occur at +0.5 V (vs. SMSE), but does take place at +0.9 V (vs. SMSE). The current at +0.9 V is readily detectable. This is will be discussed in more detail below.

EXPERIMENTAL

All experiments were carried out in the same cell as described in Chapter 2, unless stated otherwise. The bi-potentiostat (Eco Chemie PSTAT30) was operated with the ring potential held constant. The RRDE electrode consisted of a Pt disk electrode (A = 0.196 cm^2) and a glassy carbon ring electrode (A = 0.01 cm^2). The glassy carbon surface was chosen to minimize adsorption *in situ* by the organic products in solution, as this would tend to interfere with the current measurement by obstructing the surface. The rotation rate of the electrode for all experiments was 500 rpm.

Experiments were performed under both aerated and deaerated conditions in order to explore the influence of dissolved oxygen on the Cu(I)/Cu(II) equilibrium. An acidified copper sulfate solution of 0.55 M $CuSO_4$ and 0.46 M H_2SO_4 was prepared in a manner previously described (Chapter 3); SPS was added as needed as a sodium salt (bis-(sodium sulfopropyl)-disulfide, 80% purity). All concentrations of SPS are nominal values, not corrected for purity.

The collection efficiency of the RRDE was measured in the standard manner using a 1mM $Fe(CN)_6^{3-}$ solution. The disk was held at a potential negative enough to reduce the complex to $Fe(CN)_6^{4-}$, and the ring was held at a potential to oxidize it back to $Fe(CN)_6^{3-}$. In this solution, there are no parasitic reactions occurring at either the disk or the ring in the potential region of interest; therefore the entire ring current can be ascribed to oxidation of the previously reduced electroactive species. If the charge passed at the disk during reduction is greater than that passed at the ring during re-oxidation, it is clear that not all molecules reduced at the disk are detected at the ring. The ratio between the two currents is known as the collection efficiency, N, and is denoted as:

$$N = -\frac{I_\mathrm{r}}{I_\mathrm{d}} \tag{6.6}$$

where I_r and I_d are the currents at the ring and disk, respectively. N is constant for a given electrode, dependent only on r_1, r_2, and r_3; it is independent of other parameters such as rotation rate, ω, concentration, c_i, or diffusion coefficient, D_i. It is possible to calculate N from the known radii, and the calculation was similar to the measured value of N = 29%.

Prior to measurement of the collection efficiency, the electrode used in this study was polished in similar manner to that described previously [32]. Before each experiment, the electrode was cleaned in HNO_3 for 2 minutes, then rinsed with copious amounts of DI H_2O, before being placed in the electrochemical cell. The ring was operated in potentiostatic mode, with the potential being set to either +0.5 V or +0.9 V. The potential of the disk was initially swept from the open circuit potential in the positive direction, reversing in the negative direction at +1.0 V. It was then swept to -0.75 V, before reversing and returning to the initial open circuit potential. The sweep rate for all experiments was 50 mV s^{-1}.

RING POTENTIAL OF +0.5 V

Figure 6.4 shows the results of cyclic voltammograms on the disk while the ring is held at a constant potential of +0.5 V vs. SMSE. The solution was not deaerated prior to the experiments. The plots in the left column show the current at the disk while the plots in the right column show the current at the ring. SPS concentrations of 0, 100 μM and 500 μM are shown. As the disk is swept negative from the open circuit, the onset of copper reduction occurs at around -0.4 V. On the reverse scan, a large peak is observed at about -0.1 V as the deposited copper is oxidatively dissolved from the surface. For all three SPS concentrations, integration of the disk current over the duration of the experiment shows that the charge passed during deposition is similar to the charge passed during stripping. This was qualitatively confirmed by visual inspection of the disk following each experiment; the surface appeared macroscopically free of copper.

When the ring is held at a constant potential of +0.5 V, the current is initially very small, approximately 1 μA, near the detection limit of the experimental setup. As the disk potential is swept negative, it remains nearly constant until a sharp peak is observed at about -0.45 V, the start of bulk copper deposition on the disk. In all three cases, the ring current quickly drops back to a few μA as the disk potential is swept further negative. A small increase at very negative

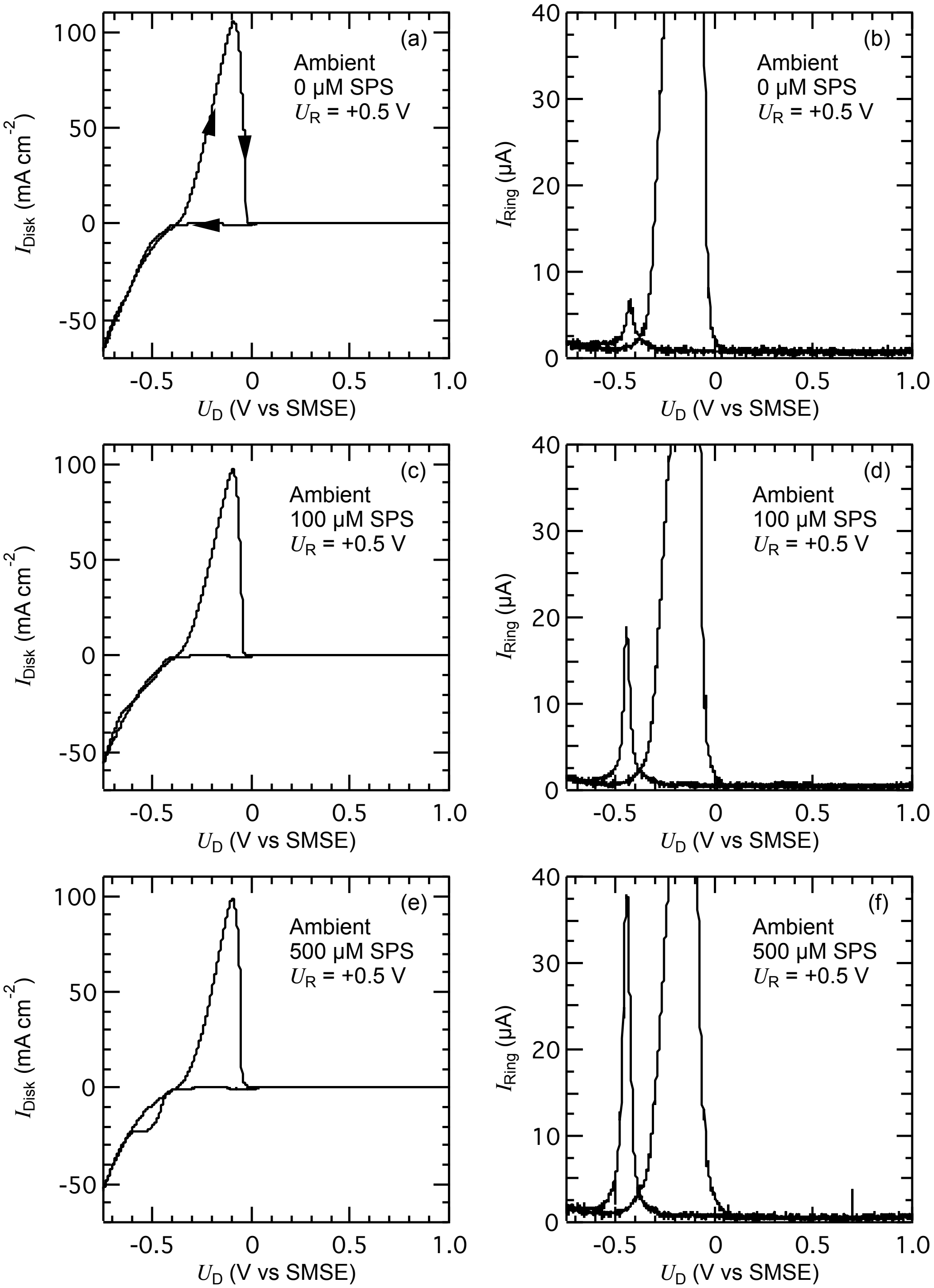

Figure 6.4: Cyclic voltammograms of a 0.55 M $CuSO_4$ + 0.46 M H_2SO_4 solution with SPS concentrations of 0 µM (a, b), 100 µM (c, d), and 500 µM (e, f). The left panel shows the disk current as a function of the applied potential to the disk, and the right panel shows the corresponding ring current. The disk potential was swept at 50 mV s^{-1} and the ring was held at a constant potential of +0.5 V vs. SMSE. The solution was *not* deaerated with nitrogen bubbling.

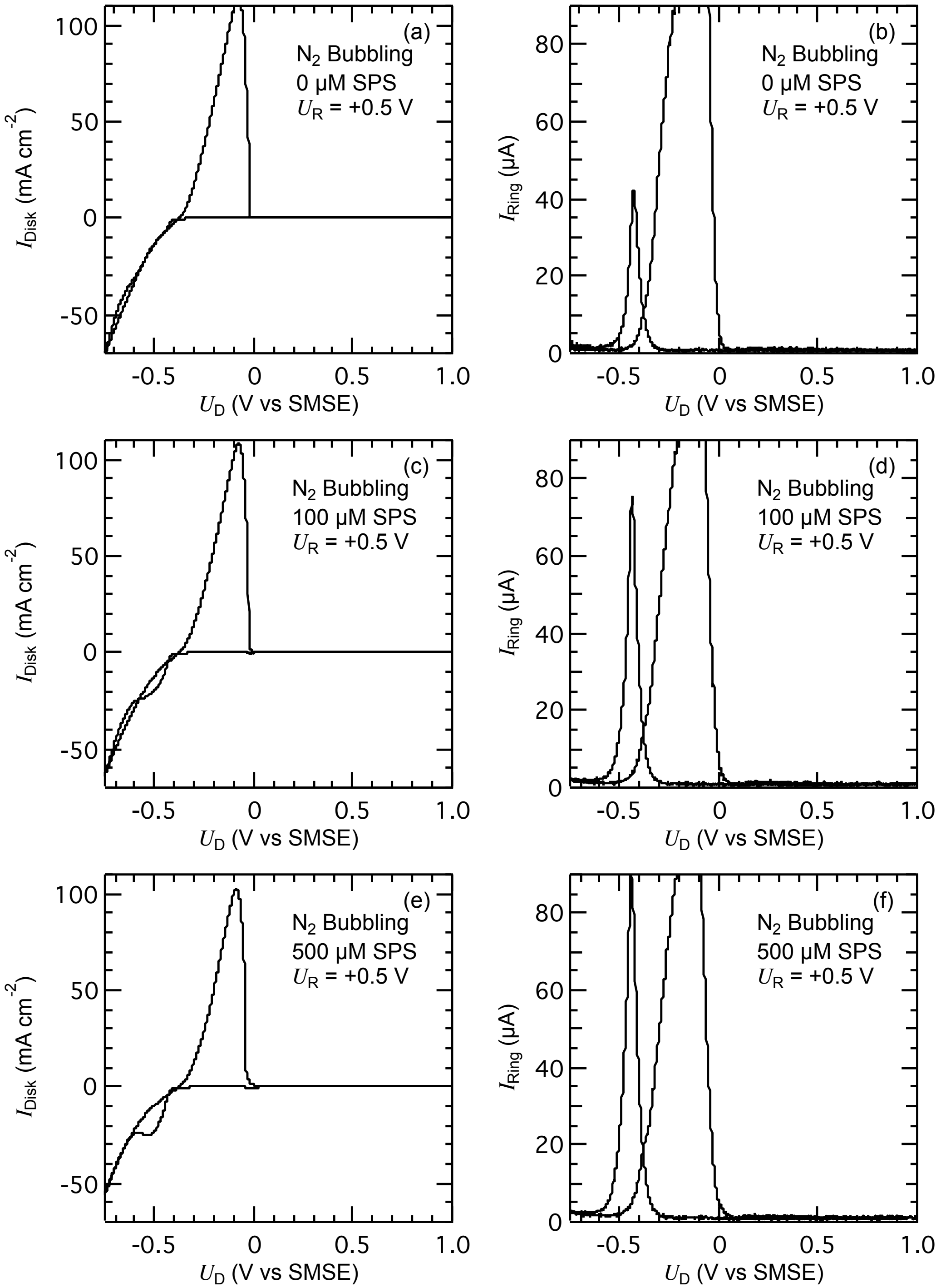

Figure 6.5: Cyclic voltammograms of a 0.55 M $CuSO_4$ + 0.46 M H_2SO_4 solution with SPS concentrations of 0 μM (a, b), 100 μM (c, d), and 500 μM (e, f). The left panel shows the disk current as a function of the applied potential to the disk, and the right panel shows the corresponding ring current. The disk potential was swept at 50 mV s^{-1} and the ring was held at a constant potential of +0.5 V vs. SMSE. The solution *was* deaerated with nitrogen bubbling.

potentials is observed. On the reverse scan, no peak is observed while the disk potential is negative of the Cu(II)/Cu equilibrium potential. With the onset of copper dissolution, a very large peak in the ring current is observed. The ring current drops to close to zero concurrent with the disk current becoming zero; this point indicates the conclusion of stripping of copper from the disk. For the remainder of the sweep, the ring current remains independent of the disk potential.

From these results, it is clear that Cu(I) species are present during the reduction of Cu(II). During copper stripping, not all of the dissolved copper is present as cupric ions. The large increase in the ring current during dissolution is the result of this incomplete oxidation, as Cu(I) species are swept to the ring and further oxidized to cupric ions. Cu(I) species are also detected in the initial sweep in the negative direction at the onset of copper deposition on the disk. For the solution without SPS, a peak of 7 μA is observed, an increase of about 6 μA above the background current. With an SPS concentration of 100 μM, the peak increases to nearly 20 μA. For 500 μM SPS, the peak in the current is nearly 40 μA. The small rise in the ring current at very negative potentials is due to the onset of hydrogen evolution at the disk, and the resulting oxidation of those products when they are swept to the ring.

Figure 6.5 shows results from the same series of experiments, but with the solution purged of oxygen by bubbling with nitrogen prior to collecting the cyclic voltammograms. Similar to the previous experiments, in all three solutions the onset of bulk copper reduction occurs at about -0.45 V, with nearly complete stripping on the reverse scan. Both stripping and the onset of bulk deposition are accompanied by an increase in the ring current, indicating the formation of Cu(I) species. However, in the purged solutions, the ring current during the onset of bulk deposition is much larger than in the oxygen containing solutions. Peak currents of 42 μA, 75 μA and 90 μA are observed for the solutions containing 0 μM, 100 μM and 500 μM SPS, respectively.

Figure 6.6 shows the peak ring currents during the onset of bulk copper deposition at the disk. Solutions through which nitrogen was bubbled (■) exhibit a higher ring current for all SPS concentrations than the solution exposed to the atmosphere (●). As the ring current is due to the oxidation of cuprous species, the lower current in solutions open to the air makes it clear that these solutions have a lower cuprous concentration than those without oxygen. The most likely cause is that the oxygen is oxidizing the copper from cuprous to cupric, and placing a limit on the cuprous ion concentration. Though they are still being formed at the same rate, the oxygen is removing them from solution before they can be detected at the ring.

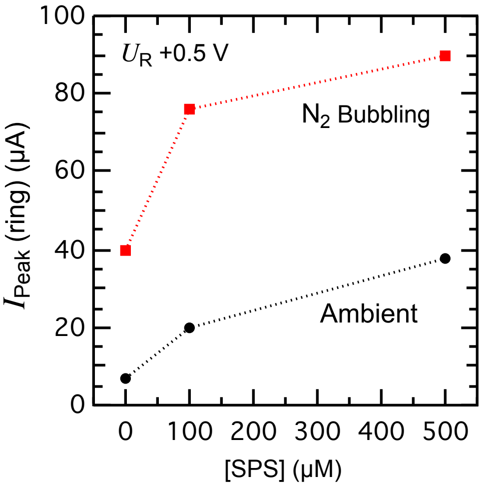

Figure 6.6: Plot of the peak ring currents measured during the forward scan as a function of SPS concentration in a 0.55 M $CuSO_4$ + 0.46 M H_2SO_4 solution for aerated (●) and deaerated (■) solutions. The ring potential was held constant at +0.5 V.

For both aerated and deaerated solutions, the peak corresponding to the presence of cuprous species increased with increasing SPS concentration. This implies that in the absence of any other complexing agents in the solution, SPS or one of its derivatives, can increase the stability of cuprous complexes in an acidified copper sulfate plating bath. However, the ability of SPS to increase the cuprous ion concentration may not be limitless. In contrast to the large increase in peak current resulting from raising the SPS concentration from 0 to 100 μM, the peak current increased only modestly when SPS concentration was further raised to 500 μM, and effect that is even more apparent in the deaerated solution. It is likely that there is a limit to the complexation of cuprous ions by SPS, and that it is reached at relatively low SPS concentrations. It is also interesting to note the measurable presence of cuprous ions in the absence of SPS in solutions exposed to the atmosphere. This is a clear indication that the Cu(I) is an important part of the electroreduction of copper in this potential range.

As the potential is scanned negative of equilibrium, a peak is seen in the voltammogram near the onset of cupper deposition. It is almost negligible in the solution without SPS, small in the 100 μM solution, and very clear in the 500 μM solution. This peak is frequently seen in copper sulfate deposition solutions, and is clearly due the presence of SPS. It is only noted here, but will be discussed in greater detail later.

Of final interest is the background ring current in the absence of a specific reaction. In all six cases in Figures 6.4 and 6.5, the current remains close to the detection limit of the experimental setup, about 1 μA. This is a key result, as it makes clear that at a potential of +0.5 V, no reactions are taking place at the ring. Both the oxidation of SPS and the evolution of oxygen gas (thermodynamically impossible, see below) are negligible at this potential.

RING POTENTIAL OF +0.9 V

Figure 6.7 shows the results of cyclic voltammograms on the disk while the ring is held at a constant potential of +0.9 V vs. SMSE. The solution was not deaerated during or prior to the experiments. As would be expected, the current response at the disk is nearly identical to the results for the ring held at +0.5 V. And while the measured ring currents also exhibit some similarities, there are important differences.

Of immediate importance is the relatively constant background current throughout the experiment. In the absence of SPS, it is 5 μA. Given the paucity of species in solution, this current could only result from the oxidation of water. Recall the equilibrium potential of reaction {6.17} is $U^0_{\mathrm{H_2O/O_2}} =$ +0.598 V (SMSE) in the solutions under investigation with measured pH = 0.6. This is one of the key reasons for selecting ring potentials of +0.5 V and +0.9 V. At +0.5 V, neither SPS nor water is oxidized, while both SPS and water are oxidized at +0.9 V. By investigating the response at these two potentials, we can separate out the effects of the background currents.

With the addition of 100 μM SPS, the ring current at +0.9 V increases to 12 μA. Since it has been previously shown that SPS can be oxidized at +0.9 V in this solution, it is likely that the measured ring current is a combination of the oxygen evolution and SPS oxidation. The current due to the oxidation of water, dependent only on pH, should be unaffected by the relatively small SPS addition. With an SPS concentration of 500 μM, the background ring current is higher still, approximately 40 μA throughout the experiment. This current is also the sum of the water oxidation (5 μA) and SPS oxidation (35 μA). The corrected currents for SPS oxidation, 7 and 35 μA, differ by a factor of five, proportional to the SPS concentrations.

A number of deviations from the background current are present in the data. In all cases,

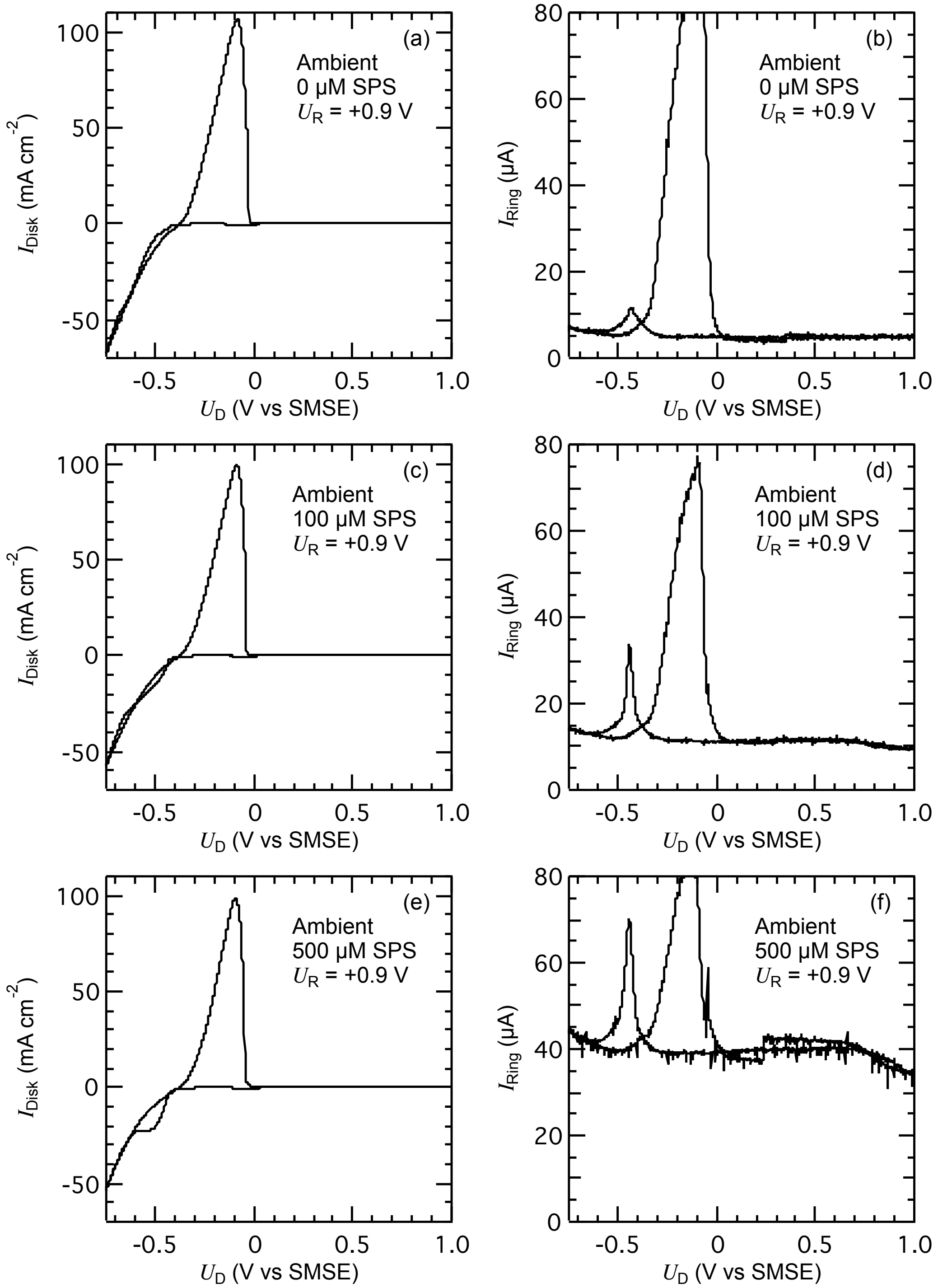

Figure 6.7: Cyclic voltammograms of a 0.55 M $CuSO_4$ + 0.46 M H_2SO_4 solution with SPS concentrations of 0 μM (a, b), 100 μM (c, d), and 500 μM (e, f). The left panel shows the disk current as a function of the applied potential to the disk, and the right panel shows the corresponding ring current. The disk potential was swept at 50 mV s^{-1} and the ring was held at a constant potential of +0.9 V vs. SMSE. The solution was *not* deaerated with nitrogen bubbling.

the ring current begins to increase at very negative disk potentials, a result of the oxidation of the products of hydrogen evolution. As before, a large ring current peak is observed to coincide with copper stripping from the disk, a result of the incomplete oxidation of the dissolved copper; the magnitude of this peak is similar under both conditions. Also as before, a sharp peak in ring current is observed near the onset of bulk copper deposition. Both the absolute magnitude of this peak, as well as its value adjusted for the background current, are seen to increase with increasing SPS concentration.

Finally, a drop in the ring current is seen when the disk potential is scanned positive of +0.7 V. Concurrent with this decrease at the ring is an increase in the current at the disk (not visible here, but shown for the deaerated solution in Figure 6.11) at the same potential. This is the result of shielding of the ring by the disk. At very positive potentials, SPS begins to be oxidized at the disk, decreasing the concentration of un-oxidized SPS as the solution is swept to the ring. With a lower un-oxidized SPS concentration in the solution above the ring, a lower ring current is detected at +0.9 V. For experiments with the ring at +0.5 V, no drop in the ring current was observed because SPS is not oxidized at this potential. Though not visible at the scale presented in Figures 6.4 and 6.5, the disk current did show a similar increase as the potential was scanned positive of +0.7 V. (This can be seen in Figure 6.11, which shows the same series of experiments with the ring held at +0.9 V; the difference in ring potential has no effect on the oxidation of SPS at the disk.)

Figure 6.8 shows the results from the same series of experiments with the solution having been deaerated by nitrogen bubbling prior to and during the experiment. Qualitatively, the results are the same. The current responses to the potential sweep on the disk are essentially identical. The current measured at the ring also shows the same features; a constant background current of about 5 μA in the absence of SPS, an increase in background current commensurate with an increase in SPS concentrations, a sharp peak during the onset of bulk copper deposition, a small increase at very negative potentials, a large spike during copper stripping, and a decrease in SPS containing solutions when the disk is scanned to very positive potentials.

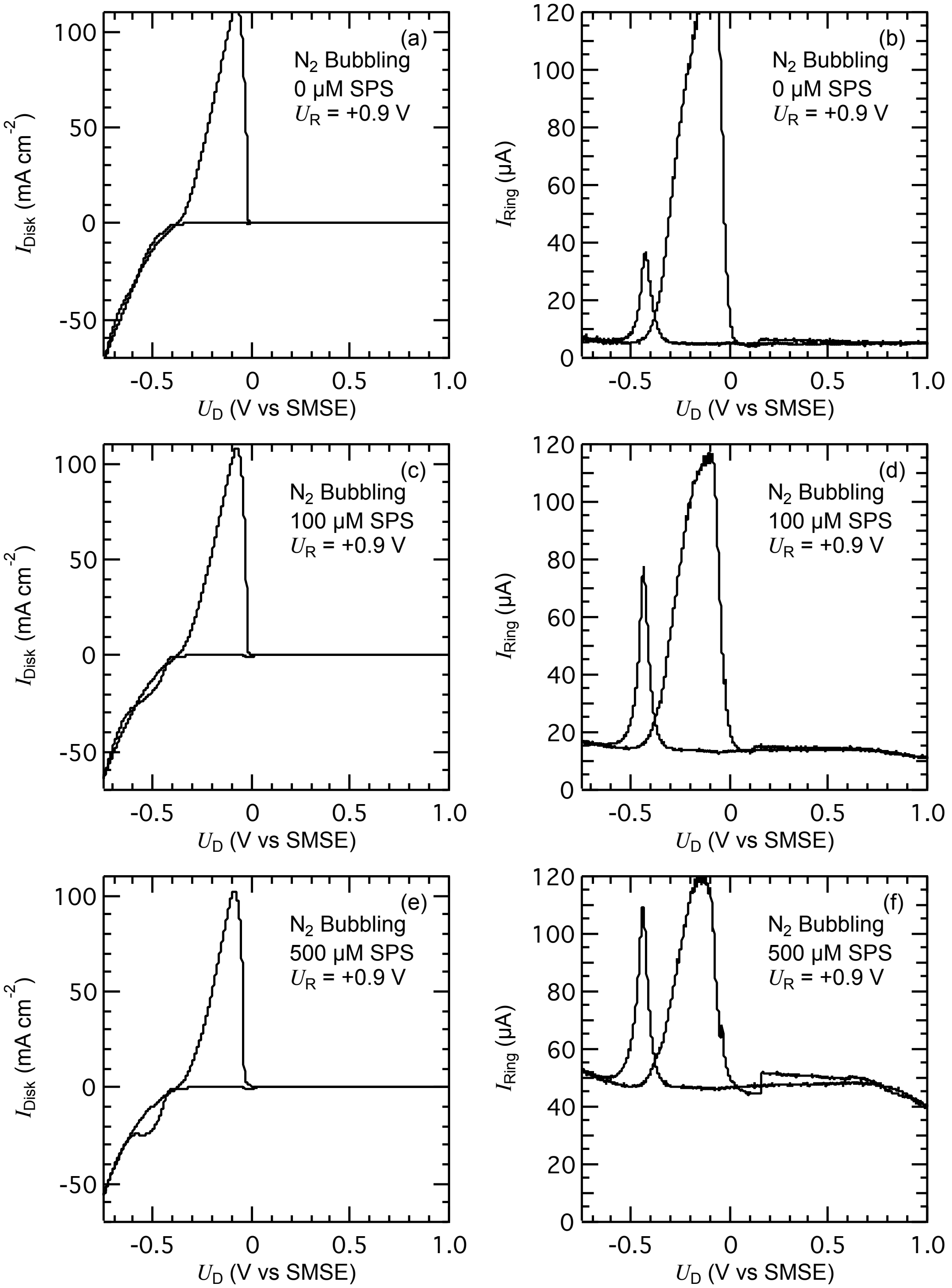

Figure 6.8: Cyclic voltammograms of 0.55 M $CuSO_4$ + 0.46 M H_2SO_4 solution with SPS concentrations of 0 μM (a, b), 100 μM (c, d), and 500 μM (e, f). The left panel shows the disk current as a function of the applied potential to the disk, and the right panel shows the corresponding ring current. The disk potential was swept at 50 mV s^{-1} and the ring was held at a constant potential of +0.9 V vs. SMSE. The solution *was* deaerated with nitrogen bubbling.

As before, the peaks in the ring current during the onset of copper deposition at the disk are larger in the absence of oxygen than when the solution is exposed to the atmosphere. Figure 6.9 shows the peak ring currents for the ring held at +0.9 V plotted against the SPS concentration for the solution exposed to the atmosphere (●) and the solution through which nitrogen was bubbled (🟥). A large increase in the current at the ring is present in the absence of oxygen, a clear indication of the ability of dissolved oxygen to oxidize cuprous species before they can travel to the ring and be detected.

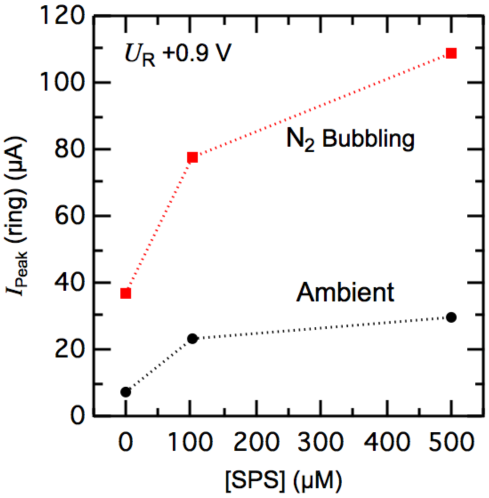

Figure 6.9: Plot of the peak ring currents measured during the forward scan as a function of SPS concentration in a 0.55 M $CuSO_4$ + 0.46 M H_2SO_4 solution for aerated (●) and deaerated (🟥) solutions. The ring potential was held constant at +0.9 V.

Figure 6.10 is a plot of the background currents versus the SPS concentration for the ring held at a potential of +0.9 V; the (negligible) background currents for the ring at +0.5 V are shown for comparison (●). The background ring current is taken to be the broadly constant current that flows over most of the disk potential range in the absence of a current at the disk. Values for both the aerated and deaerated solutions are shown. For both solutions that do not contain SPS a background current of 5 µA is present; this current results from the oxidation of water. The presence of oxygen in solution does not have any significant effect on this reaction, hence no difference in current is seen. When SPS is added to the solution, an increase in the background current proportional to the increase in SPS concentration is seen. This indicates that the

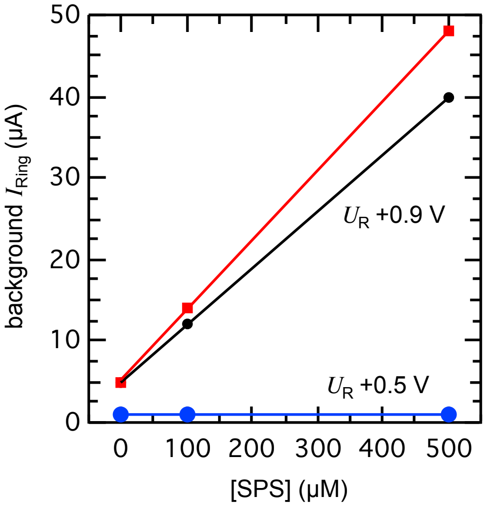

Figure 6.10: Plot of the background ring currents vs. SPS concentration with the ring held at +0.9 V for aerated (●) and deaerated (🟥) solutions of 0.55 M $CuSO_4$ + 0.46 M H_2SO_4. For comparison, the ring currents at +0.5 V are shown (●).

additional current is due to the oxidation of SPS, or one of its solution breakdown products.

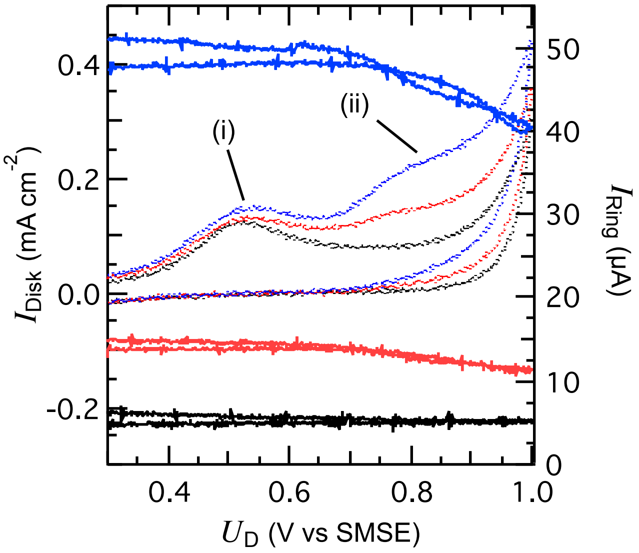

Figure 6.11: Cyclic Voltammograms of 0.55 M $CuSO_4$ + 0.46 M H_2SO_4 solution with SPS concentrations of 0 µM (**black**), 100 µM (**red**), and 500 µM (**blue**). The disk current is plotted on the left axis and the corresponding current for the ring held at +0.9 V is plotted on the right axis. The solution was deaerated with nitrogen bubbling.

Figure 6.11 provides further evidence that the increase in ring current upon the addition of SPS to the solution is due to its oxidation at the ring. The figure shows an expanded view of the behavior of the system at positive disk potentials. Three disk currents, corresponding to 0 µM (**black**), 100 µM (**red**), and 500 µM (**blue**) SPS are plotted on the left axis while the associated ring currents are plotted on the right. These solutions were bubbled with nitrogen prior to and during the experiments. As the disk potential is swept positive, a peak is observed (i) centered at +0.5 V. This peak results from the formation of an oxide layer at the platinum disk [246]. No change in ring current is observed. As the disk potential is scanned further negative, an increase in the disk current beyond +0.7 V is observed (ii) in solutions containing SPS. A corresponding drop in the ring current is seen in the same solutions. Both the increase in the disk current and the decrease in the ring current are more pronounced with increased SPS concentration. The onset of water oxidation is observed at slightly more negative disk potentials.

The drop in ring current coupled with an increase in current at the disk at disk potentials positive of +0.7 V indicates that the oxidation reaction that had been taking place at the ring is beginning to occur at the disk. As oxidation occurs at the disk, the concentration of unoxidized species decreases. This lower concentration leads to a lower ring current. The absence of this effect in solutions that do not contain SPS indicates that SPS, or one of its byproducts in solution, is taking part in this reaction.

EFFECT OF DISSOLVED OXYGEN

Both contributions to the background current, oxygen evolution and SPS oxidation, are broadly constant over the disk potential scan. This allows the ring current to be corrected by subtracting them, leaving only the current arising from cuprous oxidation. Figure 6.12 shows the peak ring currents at +0.5 V (●) and +0.9 V (🟥) corrected for the background current as a function of SPS concentration in aerated solutions. In the absence of SPS, the peak currents at the two ring potentials are identical. This is expected, as the increase in potential at the ring from +0.5 V to +0.9 V shouldn't result in an increase in cuprous oxidation, as the driving force at +0.5 V is sufficient to oxidize all cuprous ions present. At 100 μM and 500 μM, the corrected currents are close, but not identical.

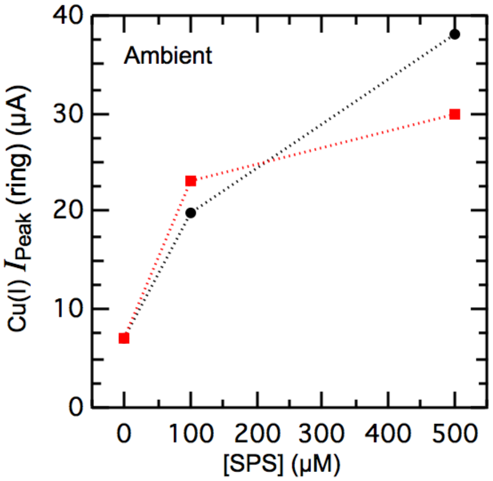

Figure 6.12: Plot of the peak ring currents measured during the forward scan corrected for the background current as a function of SPS concentration in a 0.55 M $CuSO_4$ + 0.46 M H_2SO_4 solution with the ring potential held at +0.5 V (●) and +0.9 V (🟥). The solution was *not* deaerated with nitrogen bubbling.

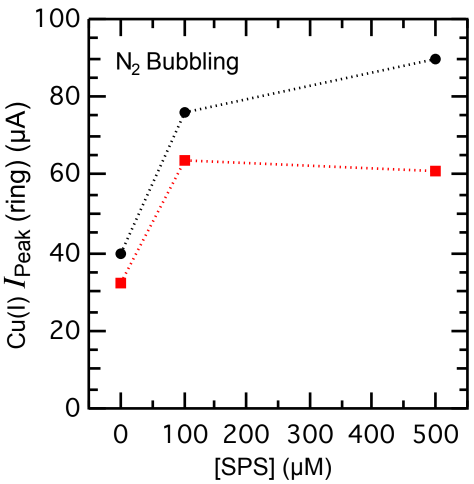

Figure 6.13: Plot of the peak ring currents measured during the forward scan corrected for the background current as a function of SPS concentration in a 0.55 M $CuSO_4$ + 0.46 M H_2SO_4 solution with the ring potential held at +0.5 V (●) and +0.9 V (🟥). The solution *was* deaerated with nitrogen bubbling.

Figure 6.13 is a similar plot of the peak ring currents at +0.5 V (●) and +0.9 V (🟥) corrected for the background current as a function of SPS concentration in solutions through which nitrogen was bubbled. As previously discussed, purging the system of oxygen removes one possible chemical pathway for the oxidation of cuprous ions to cupric ions, resulting in a higher cuprous concentration and a larger ring current from their oxidation. Hence the peak currents in Figure 6.13 are larger than those plotted in Figure 6.11. Also evident is that correcting for the background current leads to smaller peak ring currents with the ring held at +0.9 V than at +0.5 V. This result is unexpected and requires further discussion.

As stated above, the change in ring potential from +0.5 V to +0.9 V should not affect the oxidation of cuprous ions. An applied potential of +0.5 V is sufficient to oxidize all cuprous ions that pass over the surface of the ring. So the discrepancies in the currents shown in Figure 6.13 must have an alternate explanation. It is most likely that the assumptions made in correcting for the background current were not valid for all conditions. The correction assumes that the SPS oxidation current at +0.9 V that is broadly constant over the rest of the disk potential range is unaffected by the presence of the cuprous species created at the ring. Upon further examination, this assumption seems untenable.

Because cuprous ions complex with the SPS (or its derivatives) in solution, the formation of these species at the disk will lead to a drop in the free SPS concentration in the solution near the electrode surface. Because of this drop, the current due to the oxidation of SPS at the ring will be lower than in the absence of the cuprous species. This explanation does not exclude the possibility that the SPS cuprous complex is able to undergo a multi-step reaction involving the oxidation of both species, only that the overall combination of the currents from the two separate reactions is greater than that actually observed at the ring. Correcting for a background parasitic current that is higher than it is will lead to an artificially low value for the peak ring current due to cuprous oxidation, as shown in Figure 6.13.

COPPER UNDERPOTENTIAL DEPOSITION

Though primarily concerned with the bulk deposition of copper, these series of experiments also provide strong evidence for the adsorption of SPS onto copper. This can be seen by looking at the underpotential deposition (UPD) of copper onto the platinum disk electrode. It is well known that Cu forms a UPD layer on Pt [247], and this is confirmed in Figure 6.14. The figure is a plot of the disk current (dotted lines, left axis) and ring current (solid lines, right axis) plotted as a function of the disk potential as it is scanned in the negative direction.

SPS concentrations of 0 µM (**black**), 100 µM (**red**), and 500 µM (**blue**) are plotted. The ring is being held at a constant +0.9 V and the solution was deaerated with nitrogen. The plots of the ring currents for solutions containing 100 µM and 500 µM SPS have been offset to correct for the background SPS oxidation current. As the disk potential is scanned negative, a clear peak in the disk current around 0.0 V is evident. This current results from the formation of a monolayer of copper on the platinum surface at a potential positive of the equilibrium potential. As the potential is scanned more negative, the onset of bulk copper deposition is observed around -0.25 V.

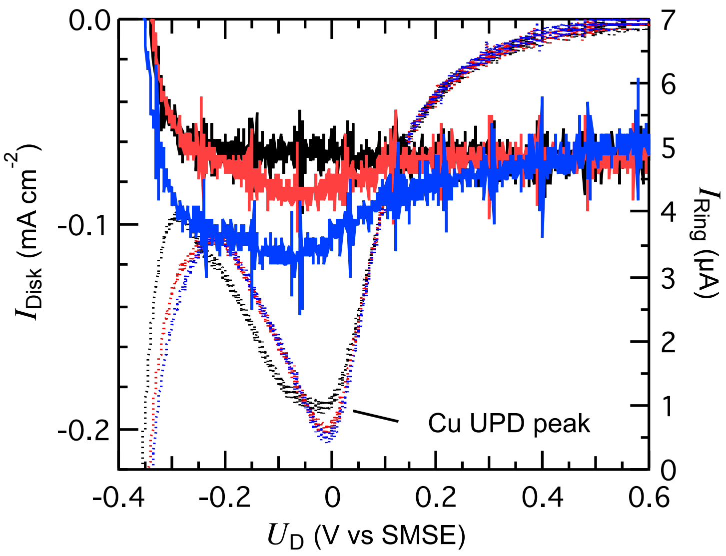

Figure 6.14: Cyclic Voltammograms of 0.55 M $CuSO_4$ + 0.46 M H_2SO_4 solution with SPS concentrations of 0 µM (**black**), 100 µM (**red**), and 500 µM (**blue**). The disk current is plotted on the left axis and the corresponding current for the ring held at +0.9 V is plotted on the right axis. The solution was deaerated with nitrogen bubbling.

As seen in the figure, the addition of SPS to the solution results in a UPD peak that is both narrower and more pronounced, indicating that a small amount of SPS is able to accelerate the copper reduction on the surface. However, increasing the SPS concentration from 100 µM to 500 µM does not noticeably provide a further increase in formation of the copper UPD layer. Commensurate with the current peak at the disk is a drop in the current at the ring for solutions containing SPS, but not in the solution without it. Though thiols adsorb very strongly to copper, they adsorb only weakly to platinum. Following the formation of the copper UPD layer, the SPS in solution quickly adsorbs to it. The drop in current at the ring in the SPS containing solutions results from the lowered SPS concentration that is swept to the ring as some of it is adsorbing at the disk. In effect, the formation of the copper UPD layer is temporarily shielding the ring.

Of particular interest in this series of experiments is the peak that is formed in the CV during the initial onset of copper deposition on the disk. Under all conditions, (panels (a) of

Figures 6.4, 6.5, 6.7, and 6.8) there is very little difference in the forward and reverse scans in solutions that do not contain SPS. With the addition of 100 µM SPS (panels (c)), a hysteresis is observed in which the current at the onset of copper deposition is temporarily greater than on the reverse scan. At 500 µM SPS, the peak is even more pronounced (panels (e)). In each case, the peak in the disk current corresponds with the peak in the ring current, clearly indicating that the increased deposition is concurrent with the presence of cuprous species.

It is the presence of the cuprous species that results in the increased deposition of copper on the disk [32]. Recall that the reduction of cupric ions to metallic copper proceeds in a stepwise manner with cuprous ions as an intermediate. However, the cuprous intermediate is not stable in the absence of a complexing agent and will rapidly be reduced to copper. This results in the first step, that of the reduction from cupric to cuprous ions being the rate-limiting step. The ability of SPS to stabilize the cuprous ion increases the rate at which cupric ions are reduced to cuprous ions, and hence increases the rate of the overall deposition reaction. This results in the increased current observed in solutions that contain SPS.

CONCLUSIONS AND RECOMMENDATIONS FOR FUTURE WORK

By conducting RRDE experiments with an acidified copper sulfate solution containing various concentrations of SPS, it was demonstrated that SPS is able to accelerate the reduction of copper. It does so by increasing the rate limiting step of cupric to cuprous reduction, stabilizing the unstable intermediate cuprous ions. It is clear that the cuprous ion formation is an important component of copper plating baths that exhibit superfilling.

In the CEAC model of trench filling, the accelerator is assumed to physically displace the suppressor from the surface, locally changing it from a blocked to an unblocked state [38]. No attempt is made to incorporate the chemistry of the additives on the overall reduction of copper. These results indicate that the chemistry of the solution in the trench may play a bigger part in superfilling than is currently thought [32, 126, 248].

This series of experiments brings up questions that lend themselves to future experiments. Most importantly is the lifetime of the cuprous species in the plating solutions. The time it takes for species to be transported from the disk to the ring is dependent upon the rotation rate of the electrode. Therefore, varying the rotation speed will vary the time cuprous ions take to get to the ring to be detected. If the current drops appreciably with a slower rotation rate, it may indicate that the transit time is on the order of the lifetime of the species. This lifetime could then be investigated as a function of SPS concentration, to see how it affects it [249]. Comparisons of experiments with nitrogen bubbling to those conducted in air could provide quantitative data on how fast cuprous ions are being removed from the solution by the oxygen. If cuprous species play as important a role in superfilling as this work suggests, then dissolved oxygen may as well, and that is worth investigating.

Also, Figures 6.12 and 6.13 indicated that the solution quickly becomes saturated with SPS. However, the range between 0 μM and 200 μM was understudied. Investigating additional concentrations in this range may provide more insight as to nature of the dependence of the cuprous ion concentration as a function of SPS concentration. As Chapter 3 of this work showed, sometimes there are sharp transitions in the behavior of systems that can provide researchers insight into the nature of the mechanics of a system. Investigation along this line may also clarify why no Cu(I) peak is seen at the ring when the potential is swept back in the positive direction.

Chapter 7

This work investigated two of the additives currently used by the semiconductor industry to electrochemically deposit copper during the manufacture of silicon-based integrated circuits (ICs). Two existing trends make this work of continuing value to materials engineers: the continuing march of Moore's Law which brings with it the constant shrinking of IC feature sizes and the near exponential proliferation of IC-containing devices into every nook and cranny of modern life. Neither trend shows any sign of near-term abatement, implying that IC manufacturing will remain an integral feature of the modern economy. Engineers will welcome further improvement in this process, and recommendations for future research are given in the text below.

It has been clearly shown that a copper-chloride-suppressor complex adsorbs to a copper surface in contact with the plating solutions used in semiconductor metallization. This complex desorbs from the surface at potentials negative of the Vereecken Potential. Concurrent with this desorption is a transition in the kinetics of copper deposition from a suppressed to unsuppressed state. This unsuppressed state is shown to be equivalent to the deposition of copper in solutions that did not contain the suppressor. This makes it clear that the adsorption of the suppressor complex is what gives rise to the inhibition of copper deposition in these plating baths. Figure 7.1 is a pictorial representation of the suppressor complex in the adsorbed and desorbed states. Suppressor molecules are shown in **green** and the chloride ions are **purple**.

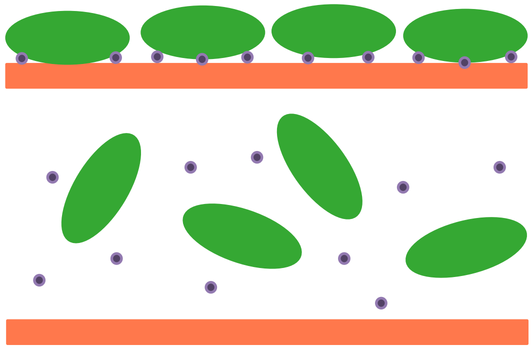

Figure 7.1: Suppressor complex: adsorbed to copper (top) and desorbed (bottom).

The Vereecken potential was shown to be dependent upon the concentration of the following solution species: cupric ions, chloride ions, hydrogen ions and suppressor molecules. These dependencies were investigated over a range of concentrations. From this data, a model of the complex was created which provided estimates for the stoichiometric concentration of the complex in its adsorbed state.

There are ways to further validate or invalidate the model painstakingly presented in Chapter 5. Recall from equations (5.4) and (5.12) the dependence of the Vereecken potential on temperature. Future researchers could investigate the desorption of the suppressor complex as a function of temperature, and confirm that it fits the model presented herein. If it does not, this would be a strong indication of a serious inadequacy in the explanation given for the observed behavior.

The suppressor investigated in this work was a proprietary Shipley additive whose exact composition and structure was not disclosed herein. A similar series of experiments using both PEG and PPG could clarify the differences between them. Because the slight difference in their structures is relatively well understood, comparing the two could provide insight into the molecular structure of the adsorbed suppressor complex, and well as hint at where various moieties are binding to the suppressor molecule [101]. A similar series of experiments could also be conducted for different molecular weight polyethers [107].

Another dependence that should be investigated is the effect of dissolved oxygen on suppression. In Chapter 6, it was shown that dissolved oxygen significantly reduces the amount of cuprous ions that are present in the solution near the surface during copper deposition. It was postulated in Chapter 5 that cuprous ions play an integral role in the adsorption of the suppressor to the surface. Conducting similar experiments in solutions that have been deaerated could provide strong experimental evidence for this. They could also indicate that oxygen is somehow involved in the formation of the suppressor complex independent of its effect of oxidizing copper, and hence reducing the concentration of, cuprous ions.

This could be further advanced by RRDE experiments of suppressor complex desorption. If Cu(I) is required for adsorption, does desorption occur when the Cu(I) concentration drops to zero during bulk deposition, like it does at very negative potentials shown in the experiments conducted on the SPS-containing solutions in Chapter 6. This could conceivably provide an alternate mechanism for the desorption of the suppressor complex than the one presented in

Chapter 5: i.e. the applied potential drives the Cu(I) concentration to zero; since it was a key component of the complex, the complex is no longer able to form on the surface, it desorbs and deposition returns to its unsuppressed state. It follows that if Cu(I) is necessary for suppression, and increasing the Cu(I) concentration leads to stronger suppression, deaerating the solution could lead to stronger suppression.

This could be very important when one considers the fact that the most important relationship in modeling superfilling is the rate at which the accelerator is able to displace the suppressor complex. In strict chemical terms, it is equivalent to the reaction listed in equation {10} in Vereecken, et al [32]. The speed with which a complete adlayer of suppressor complex is displaced by the accelerator is a key factor in determining the conditions under which the CEAC model will hold. Optimizing this parameter will allow deeper and/or narrower trenches to be filled using current electroplating techniques.

Other researchers have used EIS to investigate the effect of the additives used in the copper sulfate plating baths investigated here. In particular, Gabrielli, et al [222, 250] used EIS to investigate the aging of baths containing SPS or MPSA. They postulated that the accelerator slowly displaces and adsorbed suppressor complex. EIS measurements like the ones they conducted could be expanded to investigate the kinetics of this adsorbate substitution reaction. If the accelerator slowly displaced the suppressor, it should manifest itself as a continual increase in the interfacial capacitance, as the (average) distance between the metal and the electrolyte decreased as the portion of the surface covered by the suppressor decreased. Quantification of the kinetics of this reaction could lead to better modeling of superfilling plating baths and provide engineers the necessary tools to improve the characteristics of plating baths.

Previous EIS studies on a metal surface covered with an organic layer have shown that the simple model used in this investigation is insufficient to fully explain the system [181]. This was briefly expanded upon at the end of Chapter 3. It would seem there is significant room for improvement in the equivalent circuit used to model the deposition reaction. It may be possible for future researchers to build kinetic models that provide a full explanation of the adsorption/desorption and electroreduction reactions that occur during deposition [251].

The recent improvements in *in situ* surface measurements bring up the interesting possibility of using them to gain a better understanding of what is occurring at the surface during deposition. STM measurements on a Au surface with adsorbed PEG did not show the PEG, only the underlying gold surface structure [107]. However, this does not preclude other surface sensitive techniques from being tried. Methods developed in this work will also be able to assist researchers as they screen molecules as potential suppressors [252] to determine which may be of use in future semiconductor metallization steps.

Chapter 8

SYMBOLS, ABBREVIATIONS AND PHYSICAL CONSTANTS

Symbols

A	area	cm^2
a_i	activity in solution of species i	dimensionless
C	capacitance	F
C_D	capacitance of diffuse double layer	F
C_{dl}	double layer capacitance	F cm^{-2}
C_H	Helmholtz capacitance	F
C_P	capacitance of parallel element	F
c_i	concentration of species i	mol cm^{-3}
c_i^*	bulk concentration of species i	mol cm^{-3}
D_i	diffusion coefficient of i	cm^2 s^{-1}
d	distance	cm
e	charge on electron	C
e^-	electron	*n/a*
F	Faraday's constant	C mol^{-1}
f	frequency	s^{-1}
ΔG	Gibbs free energy change of a process	J mol^{-1}
ΔG^o	standard Gibbs free energy change of a process	J mol^{-1}
I	(a) current	A
	(b) Ionic concentration of solution	C mol L^{-1}
I_d	disk current	A
I_r	ring current	A
i	$\sqrt{-1}$	dimensionless

i	current density	A cm^{-2}
i_{ss}	steady-state current density	A cm^{-2}
K_{Cu}	equilibrium constant for Cu comproportionation	dimensionless
K_i	equilibrium constant for reaction i	dimensionless
k_B	Boltzmann's Constant	J K^{-1}
m_{Cu}	atomic mass of copper	g mol^{-1}
N	collection efficiency	dimensionless
N_A	Avogadro's number	mol^{-1}
n	number of repeat units in alkane chain	dimensionless
n	number of electrons in electrochemical reaction	dimensionless
Q	total charge	C
R	universal gas constant	J mol^{-1} K^{-1}
R	resistance	Ω
R_{ct}	charge transfer resistance	Ω
R_P	resistance of parallel element	Ω
R_S	resistance of series element	Ω
r	radius	cm
r_1	radius of RRDE disk	cm
r_2	inner radius of RRDE ring	cm
r_3	outer radius of RRDE ring	cm
t	time	s
T	temperature	K
U	potential	V
U^0	standard potential of an electrode or couple	V
U_{app}	applied potential	V
U_{eq}	equilibrium potential	V

U_D	potential applied disk on RRDE	V
U_OC	open circuit potential	V
U_R	potential applied ring on RRDE	V
U_V	Vereecken potential	V
U_Z	potential of zero charge	V
u_i	mobility of species i	$\mathrm{cm^2\ V^{-1}\ s^{-1}}$
V	voltage	V
v	deposition rate	$\mathrm{cm\ s^{-1}}$
Z	impedance	$\Omega\ \mathrm{cm^2}$
Z_Re	real portion of complex impedance	$\Omega\ \mathrm{cm^2}$
Z_Im	imaginary portion of complex impedance	$\Omega\ \mathrm{cm^2}$
z_i	charge of species i	C

Greek Symbols

α	charge transfer coefficient	dimensionless
α_A	anodic charge transfer coefficient	dimensionless
α_C	cathodic charge transfer coefficient	dimensionless
δ	diffusion layer thickness	cm
ε	dielectric constant	dimensionless
ε_0	permittivity of free space	$\mathrm{F\ cm^{-1}}$
η	overpotential	V
κ	conductivity of a solution	$\Omega^{-1}\ \mathrm{cm^{-1}}$
ν	(a) viscosity	$\mathrm{cm^2\ s^{-1}}$
	(b) sweep rate	$\mathrm{V\ s^{-1}}$
ρ	resistivity	$\Omega\ \mathrm{cm}$

ρ_{Cu}	density of copper	g cm^{-3}
ϕ	phase angle	degrees
ω	angular frequency	rad s^{-1}

Abbreviations

AC	Alternating Current
CE	Counter Electrode
CEAC	Curvature-Enhanced Accelerator Coverage
CMP	Chemical Mechanical Polishing
CPE	Constant Phase Element
CV	Cyclic Voltammogram
CVD	Chemical Vapor Deposition
CVP	Charles Village Pub
DC	Direct Current
DL	Double Layer
ECD	Electrochemical Deposition
EIS	Electrochemical Impedance Spectroscopy
EQCM	Electrochemical Quartz Crystal Microbalance
FCC	Face Centered Cubic
GCS	Gouy-Chapman-Stern
IHP	Inner Helmholtz Plane
JGB	Janus Green B
MPSA	3-mercapto-1-propanesulfonate
OHP	Outer Helmholtz Plane
PEG	Polyethylene glycol
PJ’S	PJ’s Pub
PPG	Polypropylene glycol
PSSV	Pseudo-Steady-State Voltammetry

PVD	Physical Vapor Deposition
RDE	Rotating Disk Electrode
RE	Reference Electrode
RF	Roughness Factor
RMS	Root Mean Square
RPM	Rotations Per Minute
RRDE	Rotating Ring-Disk Electrode
SEM	Scanning Electron Microscopy
SHE	Standard Hydrogen Electrode
SIMS	Secondary Ion Mass Spectroscopy
SMSE	Saturated Mercury/Mercury Sulfate Electrode
SPS	bis (3-sulfopropyl) disulfide
TBPS	3,3-thiobis(1-propanesulfonic acid)
TSV	Through-Silicon-Via
UPD	Underpotential Deposition
WE	Working Electrode
XPS	X-ray Photoelectron Spectroscopy

Physical Constants

e	elementary charge	1.60218×10^{-19} C
k_B	Boltzmann constant	1.38065×10^{-23} J K^{-1}
ε_0	permittivity of free space	8.85419×10^{-14} F cm^{-1}
F	Faraday’s constant	96,485 C mol^{-1}
m_{Cu}	atomic mass of copper	63.546 g mol^{-1}
N_A	Avogadro’s Constant	6.02214×10^{23} mol^{-1}
π	pi	3.14159265
ρ_{Cu}	density of copper	8.96 g cm^{-3}

R	Universal gas constant	8.31447 J mol^{-1} K^{-1}

Units

A	Amp
C	Coulomb
cm	Centimeter
F	Farad
g	Gram
h	Hour
J	Joule
K	Kelvin
L	Liter
M	Molarity (mol L^{-1})
m	Meter
mol	Mole
s	Second
V	Volt
Ω	Ohm

Citations

1. Bardeen, J. and W.H. Brattain, *The Transistor, A Semi-Conductor Triode.* Physical Review, 1948. **74**: p. 230-231.
2. Brattain, W.H. and J. Bardeen, *Nature of the Forward Current in Germanium Point Contacts.* Physical Review, 1948. **74**: p. 231-232.
3. Shockley, W. and G.L. Pearson, *Modulation of Conductance of Thin Films of Semi-Conductors by Surface Charges.* Physical Review, 1948. **74**: p. 232-233.
4. Li, J., T.E. Seidel, and J.W. Mayer, *Copper-Based Metallization in ULSI Structures Part II: Is Cu Ahead of Its Time as an On-Chip Interconnect Material?* MRS Bulletin, 1994: p. 15-18.
5. Gwynne, P., *Back to the Future: Copper Comes of Age.* IBM Research, 1997(4): p. 17-21.
6. Andricacos, P.C., et al., *Damascene copper electroplating for chip interconnections.* IBM Journal of Research and Development, 1998. **42**(5): p. 567-574.
7. Datta, M., *Electrochemical processing technologies in chip fabrication: challenges and opportunities.* Electrochimica Acta, 2003. **48**: p. 2975-2985.
8. Kuo, Y.-L., et al., *Diffusion of Copper in Titanium Zirconium Nitride Thin Films.* Electrochemical and Solid-State Letters, 2004. **7**(3): p. C35-C37.
9. Josell, D., et al., *Iridium Barriers for Direct Copper Electrodeposition in Damascene Processing.* Electrochemical and Solid-State Letters, 2006. **1**(10): p. 57-61.
10. Josell, D., C. Witt, and T.P. Moffat, *Osmium Barriers for Direct Copper Electrodeposition in Damascene Processing.* Electrochemical and Solid-State Letters, 2006. **9**(2): p. C41-C43.
11. Bjelkevig, C. and J. Kelber, *Stability of iodine on ruthenium during copper electrodeposition and its effects on the nucleation behavior of electrodeposited copper.* Electrochimica Acta, 2009. **54**(15): p. 3892-3898.
12. Cabral, C., Jr., et al. *Advance Metallization Conference Proceedings*. in *ULSI XIV*. 1998.

13. Jiang, Q.-T. and M.E. Thomas, *Recrystallization effects in Cu electrodeposits used in fine line damascene strucures.* Journal of Vacuum Science and Technology B, 2001. **19**(3): p. 762-766.

14. Edelstein, D.C., in *IBM Research Magazine*. 1997. p. 16.

15. Edelstein, D.C., et al., *Full Copper Wiring in a Sub-0.25 mm CMOS ULSI Technology.* IEEE IEDM, 1997: p. 773-776.

16. Radisic, A., et al., *Direct Copper Electrodeposition on TaN Barrier Layers.* Journal of the Electrochemical Society, 2003. **150**(5): p. C362-C367.

17. Radisic, A., et al., *Nucleation and Growth of Copper on TiN from Pyrophospate Solution.* Journal of the Electrochemical Society, 2001. **148**(1): p. C41-C46.

18. Radisic, A., G. Oskam, and P.C. Searson, *Influence of Oxide Thickness on Nucleation and Growth of Copper on Tantalum.* Journal of the Electrochemical Society, 2004. **151**(6): p. C369-C374.

19. Radisic, A., A.C. West, and P.C. Searson, *Influence of Additives on Nucleation and Growth of Copper on n-Si(111) from Acidic Sulfate Solutions.* Journal of the Electrochemical Society, 2002. **149**(2): p. C94-C99.

20. Oskam, G., et al., *Electrochemical deposition of metals onto silicon.* Journal of Physics D, 1998. **31**: p. 1927-1949.

21. Oskam, G. and P.C. Searson, *Electrochemical nucleation and growth of gold on silicon.* Surface Science, 2000. **446**: p. 103-111.

22. Oskam, G., P.M. Vereecken, and P.C. Searson, *Electrochemical Deposition of Copper on n-Si/TiN.* Journal of the Electrochemical Society, 1999. **146**(4): p. 1436-1441.

23. Vereecken, P.M., K. Strubbe, and W.P. Gomes, *An improved procedure for the processing of chronoamperometric data: application to the electrodeposition of Cu upon (100) n-GaAs.* Journal of Electroanalytical Chemistry, 1997. **433**: p. 19-31.

24. Zheng, M., M. Willey, and A.C. West, *Electrochemical Nucleation of Copper on Ruthenium.* Electrochemical and Solid-State Letters, 2005. **8**(10): p. C151-C154.

25. Lizama-Tzec, F.I., L. Canché-Canul, and G. Oskam, *Electrodeposition of copper into trenches from a citrate plating bath.* Electrochimica Acta, 2011. **56**(25): p. 9391-9396.

26. Hu, J.C., et al., *Effects of a new combination of additives in electroplating solution on the properties of Cu films in ULSI applications.* Journal of Vacuum Science and Technology A, 2000. **18**(4): p. 1207-1210.

27. Kang, M., M.E. Gross, and A.A. Gewirth, *Atomic Force Microscopy Examination of Cu Electrodeposition in Trenches.* Journal of the Electrochemical Society, 2003. **150**(5): p. C292-C301.

28. Willey, M.J. and A.C. West, *SPS Adsorption and Desorption during Copper Electrodeposition and Its Impact on PEG Adsorption.* Journal of The Electrochemical Society, 2007. **154**(3): p. D156-D162.

29. Yang, L., et al., *Modeling the Bottom-Up Filling of Through-Silicon vias Through Suppressor Adsorption/Desorption Mechanism.* Journal of The Electrochemical Society, 2013. **160**(12): p. D3051-D3056.

30. Akolkar, R. and U. Landau, *A Time-Dependent Transport-Kinetics Model for Additive Interactions in Copper Interconnect Metallization.* Journal of the Electrochemical Society, 2004. **151**(11): p. C702-C711.

31. Healy, J.P., D. Pletcher, and M. Goodenough, *The chemistry of the additives in an acid copper electroplating bath Part II. The instability of 4,5-dithiaoctane-1,8-disulphonic acid in the bath on open circuit.* Journal of Electroanalytical Chemistry, 1992. **338**: p. 167-177.

32. Vereecken, P.M., et al., *The chemistry of additives in damascene copper plating.* IBM Journal of Research and Development, 2005. **49**(1): p. 3-18.

33. Kim, J.J., S.-K. Kim, and Y.S. Kim, *Catalytic behavior of 3-mercapto-1-propane sulfonic acid on Cu electrodeposition and its effect on Cu film properties for CMOS device metallization.* Journal of Electroanalytical Chemistry, 2003. **542**: p. 61-66.

34. Kim, S.-K. and J.J. Kim, *Superfilling Evolution in Cu Electrodeposition.* Electrochemical and Solid-State Letters, 2004. **7**(9): p. C98-C100.

35. Moffat, T.P., et al., *Accelerator Aging Effects During Copper Electrodeposition.* Electrochemical and Solid-State Letters, 2003. **6**(4): p. C59-C62.

36. Teerlinck, I., *Electrochemical Copper Deposition in IC Manufacturing*. 2002, University of Ghent: Leuven.

37. Long, J.G., P.C. Searson, and P.M. Vereecken, *Electrochemical Impedance Spectroscopy Study of Suppressor-Chloride Complex Adsorption and Desorption on Copper Surfaces.* in preparation, 2005.

38. Jin, Y., et al., *Competitive Adsorption of PEG and SPS on Copper Surface in Acidic Electrolyte Containing Cl−.* Journal of The Electrochemical Society, 2013. **160**(1): p. D20-D27.

39. Lin, K.-C., et al., *Electroplating Copper in Sub-100nm Gaps by Additives with Low Consumption and Diffusion Ability.* Journal of Vacuum Science and Technology B, 2002. **20**: p. 940-945.

40. Deligianni, H., et al. *Electrochemical Processing in ULSI Fabrication III*. 2000. Toronto.

41. West, A.C., *Theory of Filling of High-Aspect Ratio Trenches and Vias in Presence of Additives.* Journal of the Electrochemical Society, 2000. **147**(1): p. 227-232.

42. Georgiadou, M., et al., *Simulation of Shape Evolution during Electrodeposition of Copper in the Presence of Additive.* Journal of the Electrochemical Society, 2001. **148**(1): p. C54-C58.

43. Kang, M. and A.A. Gewirth, *Influence of Additives on Copper Electrodeposition on Physical Vapor Deposited (PVD) Copper Substrates.* Journal of the Electrochemical Society, 2003. **150**(6): p. C426-C434.

44. Cao, Y., et al., *Three-Additive Model of Superfilling of Copper.* Journal of the Electrochemical Society, 2001. **148**(7): p. C466-C472.

45. Taephaisitphongse, P., Y. Cao, and A.C. West, *Electrochemical and Fill Studies of a Multicomponent Additive Package for Copper Deposition.* Journal of the Electrochemical Society, 2001. **148**(7): p. C492-C497.

46. West, A.C., S. Mayer, and J. Reid, *A Superfilling Model that Predicts Bump Formation.* Electrochemical and Solid-State Letters, 2001. **4**(7): p. C50-C53.

47. Josell, D., T.P. Moffat, and D. Wheeler, *An Exact Algebraic Solution for the Incubation Period of Superfill.* Journal of the Electrochemical Society, 2004. **151**(1): p. C19-C24.

48. Josell, D., et al., *A Simple Equation for Predicting Superconformal Electrodeposition in Submicrometer Trenches.* Journal of the Electrochemical Society, 2001. **148**(12): p. C767-C773.

49. Wheeler, D., D. Josell, and T.P. Moffat, *Modeling Superconformal Electrodeposition Using The Level Set Method.* Journal of the Electrochemical Society, 2003. **150**(5): p. C302-C310.

50. Atanasova, T.A., et al., *Ultra-Low Copper Baths for Sub-35 nm Copper Interconnects.* Journal of The Electrochemical Society, 2013. **160**(12): p. D3255-D3259.

51. Pourbaix, M.J.N. and J.A. Franklin, *Atlas of electrochemical equilibria in aqueous solutions. By Marcel Pourbaix. Translated by James A. Franklin, etc*. 1966, Pergamon Press: Oxford.

52. Cho, S.K., S.-K. Kim, and J.J. Kim, *Superconformal Cu Electrodeposition Using DPS.* Journal of the Electrochemical Society, 2005. **152**(5): p. C330-C333.

53. Hazlebeck, D.A. and J.B. Talbot, *Modeling of Additive Effects on the Electroplating of a Through-Hole.* American Institute of Chemical Engineers Journal, 1990. **36**(8): p. 1145-1155.

54. Farndon, E.E., F.C. Walsh, and S.A. Campbell, *Effect of thiourea, benzotriazole and 4,5-dithiaoctance-1,8-disulphonic acid on the kinetics of copper deposition from dilute acid sulphate solutions.* Journal of Applied Electrochemistry, 1995. **25**: p. 574-583.

55. Ke, B., et al., *Role of Thiourea in the Electrodeposition of Copper.* Journal of The Electrochemical Society, 1959. **106**(5): p. 382-388.

56. Turner, D.R. and G.R. Johnson, *The Effect of Some Addition Agents on the Kinetics of Copper Electrodeposition from a Sulfate Solution: I . Cathode Potential-Current Density Relation.* Journal of The Electrochemical Society, 1962. **109**(9): p. 798-804.

57. Oniciu, L. and L. Mureşan, *Some fundamental aspects of levelling and brightening in metal electrodeposition.* Journal of Applied Electrochemistry, 1991. **21**(7): p. 565-574.

58. Armstrong, M.J. and R.H. Muller, *In Situ Scanning Tunneling Microscopy of Copper Deposition with Benzotriazole.* Journal of The Electrochemical Society, 1991. **138**(8): p. 2303-2307.

59. Delhez, R., 1961. **30**: p. 446.

60. Miller, B., *Split-Ring Disk Study of the Anodic Processes at a Copper Electrode in Alkaline Solution.* Journal of the Electrochemical Society, 1969. **116**: p. 1675-1680.

61. Tindall, G.W. and S. Bruckenstein, *Determination of Heterogeneous Equilibrium Constants by Chemical Stripping at a Ring-Disk Electrode.* Analytical Chemistry, 1968. **40**(10): p. 1402-1404.

62. Miller, R.W. 1961, University of Illinois: Urbana.

63. deBethune, A.J., T.S. Licht, and N. Swendeman, *The Temperature Coefficients of Electrode Potentials.* Journal of the Electrochemical Society, 1959. **106**(7): p. 616-625.

64. Latimer, W.M., *Oxidation Potentials*. 2nd ed. 1952, New York: Prentice-Hall.

65. Bard, A.J., ed. *Encyclopedia of Electrochemistry of the Elements*. Vol. 2. 1974, Marcel Dekker, Inc.: New York.

66. Getman, F.H., *A Study of the Potential of the Copper Electrode.* Journal of Physical Chemistry, 1930. **34**: p. 1454-1465.

67. Leidheiser, H. and A.T. Gwathmey, Transactions of the Electrochemical Society, 1947. **91**: p. 97.

68. Tragert, W.E. and W.D. Robertson, *The Crystallographic Dependence of the Oxidation Potential of Solid Copper.* Journal of the Electrochemical Society, 1955. **102**: p. 86-94.

69. Jenkins, L.H. and U. Bertocci, *On the Equilibrium Properties of Single Crystalline Copper Electrodes.* Journal of the Electrochemical Society, 1965. **112**(5): p. 517-520.

70. Jenkins, L.H. and U. Bertocci, *On the Equilibrium Properties of Single Crystalline Copper Electrodes.* Journal of the Electrochemical Society, 1965. **112**(12): p. 1262-1263.

71. Bockris, J.O.M. and M. Enyo, *Mechanism of Electrodeposition and Dissolution Processes of Copper in Aqueous Solutions.* Transactions of the Faraday Society, 1962. **58**: p. 1187-1202.

72. Hampson, N.A. and R.J. Latham, *Cu(II)/Cu Exchange Reaction In Nitrate Electrolyte.* Transactions of the Faraday Society, 1970. **66**: p. 3131-3142.

73. Hillson, P.J., *The Mechanism of the Reaction at a Cu/Cu*$^{2+}$ *Electrode.* Transactions of the Faraday Society, 1954. **50**: p. 385-393.

74. Hampson, N.A. and R.J. Latham, *Cu(II)/Cu Exchange Reaction in Sulphate Electrolyte.* Transactions of the Faraday Society, 1971. **67**: p. 1440-1446.

75. Lecoeur, J. and J.P. Bellier, *Potentiels de charge nulle d'electrodes monocristallines de cuivre d'orientation (111) et (100) au contact de solutions aqueuses de perchlorate de potassium.* Electrochimica Acta, 1985. **30**(8): p. 1027-1033.

76. Hori, Y., et al., *Adsorption of CO accompanied with simultaneous charge transfer on copper single crystal electrodes related with electrochemical reduction of CO2 to hydrocarbons.* Surface Science, 1995. **335**(0): p. 258-263.

77. Trasatti, S., *Work Function, Electronegativity, and Electrochemical Behaviour of Metals.* Journal of Electroanalytical Chemistry, 1971. **33**: p. 351-378.

78. Armstrong, D., N.A. Hampson, and R.J. Latham, *The Differential Capacitance of Polycrystalline Copper in Aqueous Solution.* Journal of Electroanalytical Chemistry, 1969. **23**: p. 361-367.

79. Yao, Y.L., Transactions of the Electrochemical Society, 1944. **86**: p. 371.

80. Gauvin, W.H. and C.A. Winkler, *The Effect of Chloride Ions on Copper Deposition.* Journal of the Electrochemical Society, 1952. **99**(2): p. 71.

81. Kelly, J.J. and A.C. West, *Copper Deposition in the Presence of Polyethylene Glycol I. Quartz Crystal Microbalance Study.* Journal of the Electrochemical Society, 1998. **145**(10): p. 3472-3476.

82. Yoon, S., M. Schwartz, and K. Nobe, Plating and Surface Finishing, 1994. **81**: p. 65.

83. Jovic, V.D. and B.M. Jovic, *Copper electrodeposition from a copper acid baths in the presence of PEG and NaCl.* Journal of the Serbian Chemical Society, 2001. **66**(11-12): p. 935-952.

84. Moffat, T.P., et al., *Superconformal Electrodeposition of Copper in 500-90 nm Features.* Journal of the Electrochemical Society, 2000. **147**(12): p. 4524-4535.

85. Moffat, T.P., et al., *Superconformal Electrodeposition of Copper.* Electrochemical and Solid-State Letters, 2001. **4**(4): p. C26-C29.

86. Moffat, T.P., et al., *Superconformal Electrodeposition Using Derivitized Substrates.* Electrochemical and Solid-State Letters, 2002. **5**(12): p. C110-C112.

87. Denaro, A.R., *Elementary Electrochemistry*. 1975, London: Butterworths.

88. Sillén, L.G., ed. *Stability Constants of Metal-Ion Complexes. Section I: Inorganic Ligands*. Stability Constants of Metal-Ion Complexes. 1964, The Chemical Society: London.

89. Högfelat, E., ed. *Stability Constants of Metal-Ion Complexes. Supplement #2 Part A*. Stability Constants of Metal-Ion Complexes. 1982, Pergamon Press: Oxford.

90. Fonsati, M., F. Zucchi, and G. Trabanelli, *Study of corrosion inhibition in 0.1 M NaCl using the EQCM technique.* Electrochimica Acta, 1998. **44**: p. 311-322.

91. Soares, D.M., et al., *Copper ion reduction catalyzed by chloride ions.* Journal of Electroanalytical Chemistry, 2002. **532**: p. 353-358.

92. Gileadi, E. and V. Tsionsky, *Studies of Electroplating Using an EQCM I. Copper and Silver on Gold.* Journal of the Electrochemical Society, 2000. **147**(2): p. 567-574.

93. Crousier, J. and I. Bimaghra, *Electrodeposition of copper from sulphate and chloride solutions.* Electrochimica Acta, 1989. **34**(8): p. 1205-1211.

94. Láng, G.G., M. Ujvári, and G. Horányi, *New EQCM voltammetric and radiotracer evidences proving the role of Cu^+ ions in the behavior of the Cu^{2+}-Cu system.* Journal of Electroanalytical Chemistry, 2002. **522**: p. 179-188.

95. Scendo, M. and J. Malyszko, *The Influence of Benzotriazole and Tolyltriazole on the Copper Electrodeposition on Polycrystalline Platinum from Acidic Chloride Solutions.* Journal of the Electrochemical Society, 2000. **147**(5): p. 1758-1762.

96. Bonou, L., et al., *Influence of additives on Cu electrodeposition mechanisms in acid solution: direct current study supported by non-electrochemical measurements.* Electrochimica Acta, 2002. **47**: p. 4139-4148.

97. Stoychev, D. and C. Tsvetanov, *Behaviour of poly(ethylene glycol) during electrodeposition of bright copper coatings in sulfuric acid electrolytes.* Journal of Applied Electrochemistry, 1996. **26**: p. 741-749.

98. Stoychev, D., et al., *Effect of some diakyl-, diaryl-, and diaryalkyl-disulphide derivatives on copper electrodeposition.* Journal of Applied Electrochemistry, 1992. **22**: p. 978-986.

99. Walker, M.L., L.J. Richter, and T.P. Moffat, *Competitive Adsorption of PEG, Cl−, and SPS/MPS on Cu: An In Situ Ellipsometric Study.* Journal of The Electrochemical Society, 2006. **153**(8): p. C557-C561.

100. Hebert, K.R., *Role of Chloride Ions in Suppression of Copper Electrodeposition by Polyethylene Glycol.* Journal of The Electrochemical Society, 2005. **152**(5): p. C283-C287.

101. Yang, L., et al., *Stochastic Modeling of Polyethylene Glycol as a Suppressor in Copper Electroplating.* Journal of The Electrochemical Society, 2014. **161**(5): p. D269-D276.

102. Fabricius, G., K. Kontturi, and G. Sundholm, *Influence of thiourea on the nucleation and growth of copper from acid sulphate solutions.* Electrochimica Acta, 1994. **39**(16): p. 2353-2357.

103. Leung, T.Y.B., et al., *Benzotriazole as an Additive for Copper Electrodeposition: Influence of Triazole Ring Substitution.* Journal of the Electrochemical Society, 2000. **147**(9): p. 3326-3337.

104. Ryan, K., et al., *Properties of PEG, PPG and Their Copolymers: Influence on Copper Filling of Damascene Interconnects.* Journal of The Electrochemical Society, 2013. **160**(12): p. D3186-D3196.

105. Atanasova, T.A., K. Strubbe, and P.M. Vereecken, *Adsorption/Desorption of Suppressor Complex on Copper: Description of the Critical Potential.* ECS Transactions, 2011. **33**(37): p. 13-26.

106. Chang, S.-C., et al., *Investigations of effects of bias polarization and chemical parameters on morphology and filling capability of 130 nm damascene electroplated copper.* Journal of Vacuum Science and Technology B, 2001. **19**(3): p. 767-773.

107. Petri, M., et al., *Adsorption of PEG on Au(111) Single-Crystal Electrodes and Its Influence on Copper Deposition.* Journal of the Electrochemical Society, 2004. **151**(12): p. C793-C797.

108. Feng, Z.V., X. Li, and A.A. Gewirth, *Inhibition Due to the Interaction of Polyethylene Glycol, Chloride, and Copper in Plating Baths: A Surface-Enhanced Raman Spectroscopy.* Journal of Physical Chemistry B, 2003. **107**(35): p. 9415-9423.

109. Reid, J.D. and A.P. David, *Effects of Polyethylene Glycol on the Electrochemical Characteristics of Copper Cathodes In An Acid Copper Medium.* Plating and Surface Finishing, 1987. **74**: p. 66-70.

110. Dow, W.-P., et al., *Influence of Molecular Weight of Polyethylene Glycol on Microvia Filling by Copper Electroplating.* Journal of The Electrochemical Society, 2005. **152**(11): p. C769-C775.

111. Goldbach, S., et al., *Coupled effects of chloride ions and branch chained polypropylene ether LP-1 on the electrochemical deposition of copper from sulfate solutions.* Electrochimica Acta, 1998. **44**(2-3): p. 323-335.

112. Takahashi, K.M. and M.E. Gross, *Transport Phenomena That Control Electroplated Copper Filling of Submicron Vias and Trenches.* Journal of the Electrochemical Society, 1999. **146**(12): p. 4499-4505.

113. Chiu, S.-Y., et al., *Characterization of additive systems for damascene Cu electroplating by the superfilling profile monitor.* Journal of Vacuum Science and Technology B, 2000. **18**(6): p. 2835-2841.

114. Natter, H. and R. Hempelmann, *Nanocrystalline Copper by Pulsed Electrodeposition: The Effects of Organic Additives, Bath Temperature, and pH.* Journal of Physical Chemistry, 1996. **100**: p. 19525-19532.

115. Osborn, T., N. Galiba, and P.A. Kohl, *Electroless Copper Deposition with PEG Suppression for All-Copper Flip-Chip Connections.* Journal of The Electrochemical Society, 2009. **156**(7): p. D226-D230.

116. Hasegawa, M., et al., *Evidence for "superfilling" of submicrometer trenches with electroless copper deposit.* Applied Physics Letters, 2007. **90**(10): p. -.

117. Josell, D., et al., *Gold Superfill in Sub-Micrometer Trenches.* Electrochemical and Solid-State Letters, 2005. **8**(3): p. C54.

118. Josell, D., et al., *Interconnect Fabrication by Superconformal Iodine-Catalyzed Chemical Vapor Deposition of Copper.* Journal of the Electrochemical Society, 2003. **150**(5): p. C368-C373.

119. Baker, B.C., et al., *Superconformal Electrodeposition of Silver from a* $KAg(CN)_2$*-KCN-KSeCN Electrolyte.* Journal of the Electrochemical Society, 2003. **150**(2): p. C61-C66.

120. Baker, B.C., et al., *Superconformal Silver Deposition Using KSeCN Derivatized Substrates.* Electrochemical and Solid-State Letters, 2003. **6**(5): p. C67-C69.

121. Moffat, T.P., et al., *Superconformal Electrodeposition of Silver in Submicrometer Features.* Journal of the Electrochemical Society, 2002. **149**(8): p. C423-C428.

122. Hayase, M. and K. Otsubo, *Copper Deep Via Filling with Selective Accelerator Deactivation by a Reverse Pulse.* Journal of The Electrochemical Society, 2010. **157**(12): p. D628-D632.

123. Moffat, T.P., et al., *Curvature enhanced adsorbate coverage mechanism for bottom-up superfilling and bump control in damascene processing.* Electrochimica Acta, 2007. **53**(1): p. 145-154.

124. Radisic, A., et al., *Copper plating for 3D interconnects.* Microelectronic Engineering, 2011. **88**(5): p. 701-704.

125. Tzu-Hsuan, T. and H. Jui-Hsiung, *Copper electrodeposition in a through-silicon via evaluated by rotating disc electrode techniques.* Journal of Micromechanics and Microengineering, 2010. **20**(11): p. 115023.

126. Lühn, O., et al., *Monitoring the Superfilling of Blind Holes with Electrodeposited Copper.* Journal of The Electrochemical Society, 2010. **157**(4): p. D242-D247.

127. Tan, M., et al., *The Role of SPS, MPSA, and Chloride in Additive Systems for Copper Electrodeposition.* Journal of The Electrochemical Society, 2007. **154**(2): p. D78-D81.

128. Pasquale, M.A., L.M. Gassa, and A.J. Arvia, *Copper electrodeposition from an acidic plating bath containing accelerating and inhibiting organic additives.* Electrochimica Acta, 2008. **53**(20): p. 5891-5904.

129. Dow, W.-P. and M.-Y. Yen, *Microvia Filling over Self-Assembly Disulfide Molecule on Au and Cu Seed Layers: A Morphological Study of Copper Deposits.* Electrochemical and Solid-State Letters, 2005. **8**(11): p. C161-C165.

130. Zhang, W., et al., *Geometry Effect on Impurity Incorporation and Grain Growth in Narrow Copper Lines.* Journal of The Electrochemical Society, 2005. **152**(12): p. C832-C837.

131. Chiu, Y.-D. and W.-P. Dow, *Accelerator Screening by Cyclic Voltammetry for Microvia Filling by Copper Electroplating.* Journal of The Electrochemical Society, 2013. **160**(12): p. D3021-D3027.

132. Kim, S.-K., D. Josell, and T.P. Moffat, *Cationic Surfactants for the Control of Overfill Bumps in Cu Superfilling.* Journal of The Electrochemical Society, 2006. **153**(12): p. C826-C833.

133. Schultz, Z.D., et al., *Vibrational Spectroscopic and Mass Spectrometric Studies of the Interaction of Bis(3-sulfopropyl)-disulfide with Cu Surfaces.* Journal of The Electrochemical Society, 2006. **153**(2): p. C97-C107.

134. Guymon, C.G., et al., *MPSA effects on copper electrodeposition investigated by molecular dynamics simulations.* The Journal of Chemical Physics, 2008. **128**(4): p. -.

135. Bain, C.D., et al., *Formation of Monolayer Films by the Spontaneous Assembly of Organic Thiols from Solution onto Gold.* Journal of the American Chemical Society, 1989. **111**: p. 321-335.

136. Brito, R., et al., *Adsorption of 3-mercaptopropyltrimethoxysilane and 3-aminopropylmethoxysilane at platinum electrodes.* Journal of Electroanalytical Chemistry, 2002. **520**: p. 47-52.

137. Dubois, L.H. and R.G. Nuzzo, *Synthesis, Structure, and Properties of Model Organic Surfaces.* Annual Review of Physical Chemistry, 1992. **43**: p. 437-463.

138. Poirier, G.E., *Characterization of Organosulfur Molecular Monolayers on Au(111) using Scanning Tunneling Microscopy.* Chemical Reviews, 1997. **97**(4): p. 1117-1127.

139. Poirier, G.E., *Mechanism of Formation of Au Vacancy Islands in Alkanethiol Monolayers on Au(111).* Langmuir, 1997. **13**(7): p. 2019-2026.

140. Schlenoff, J.B., M. Li, and H. Ly, *Stability and Self-Exchange in Alkanethiolate Monolayers.* Journal of the American Chemical Society, 1995. **117**(50): p. 12528-12536.

141. Laibinis, P.E., et al., *Comparison of the Structures and Wetting Properties of Self-Assembled Monolayers of n-Alkanethiols on the Coinage Metal Surfaces, Cu, Ag, Au.* Journal of the American Chemical Society, 1991. **113**: p. 7152-7167.

142. Lee, Y.J., et al., *Self-Assembly of 1,2-Benzenedithiol on Gold and Silver: Fourier Transform Infrared Spectroscopy and Quartz Crystal Microbalance Study.* Langmuir, 1996. **12**(24): p. 5830-5837.

143. Rieley, H. and G.K. Kendall, *X-ray Studies of Self-Assembled Monolayers on Coinage Metals. 3. Angularly Resoved Near Edge X-ray Absorption Fine Structure Determination of the Orientation in 1-Octanethiol SAMs on Ag(111) and Cu(111).* Langmuir, 1999. **15**: p. 8867-8875.

144. Walczak, M.M., et al., *Structure and Interfacial Properties of Spontaneously Adsorbed n-Alkanethiolate Monolayers on Evaporated Silver Surfaces.* Journal of the American Chemical Society, 1991. **113**: p. 2370-2378.

145. Keller, H., et al., *Surface chemistry of thiols on copper: an efficient way of producing multilayers.* Thin Solid Films, 1994. **244**: p. 799-805.

146. Laibinis, P.E. and G.M. Whitesides, *Self-Assembled Monolayers of n-Alkanethiolates on Copper Are Barrier Films That Protect the Metal against Oxidation by Air.* Journal of the American Chemical Society, 1992. **114**: p. 9022-9028.

147. Sung, M.M., et al., *Self-Assembled Monolayers of Alkanethiols on Oxidized Copper Surfaces.* Journal of Physical Chemistry B, 2000. **104**: p. 2273-2277.

148. Yamamoto, Y., H. Nishihara, and K. Aramaki, *Self-Assembled Layers of Alkanethiols on Copper for Protection Against Corrosion.* Journal of the Electrochemical Society, 1993. **140**(2): p. 436-443.

149. Clavilier, J., V. Svetlicic, and V. Zutic, *Self-Assembly of methylene blue at single-crystal platinum electrodes modified by sulphur adlayer.* Journal of Electroanalytical Chemistry, 1996. **402**: p. 129-135.

150. Berezin, M.Y., et al., *Thiol protected platinum black and palladium black catalysts in oxidation catalysis.* Journal of Molecular Catalysis A: Chemical, 2000. **158**: p. 567-576.

151. Brito, R., et al., *Chemical derivatization of self-assembled 3-mercaptopropionic and 16-mercatohexadecanoic acids at platinum surfaces with 3-aminopropyltrimethoxysilane: a spectroscopic and electrochemical study.* Journal of Electroanalytical Chemistry, 2003. **540**: p. 53-59.

152. Hickman, J.J., et al., *Toward Orthogonal Self-Assembly of Redox Active Molecules on Pt and Au: Selective Reaction of Disulfide with Au and Isocyanide with Pt.* Langmuir, 1992. **8**(2): p. 357-359.

153. Lang, P., et al., *Self-assembled alkylthiols monolayers onto platinum; influence of the adsorbed oxygen.* Journal of Electroanalytical Chemistry, 1998. **441**: p. 83-93.

154. Demoz, A. and D.J. Harrison, *Characterization of Extremely Low Defect Density Hexadecanethiol Monolayers on Hg Surfaces.* Langmuir, 1993. **9**(4): p. 1046-1050.

155. Dannenberger, O., M. Buck, and M. Grunze, *Self-Assembly of n-Alkanethiols: A Kinetic Study by Second Harmonic Generation.* Journal of Physical Chemistry B, 1999. **103**: p. 2202-2213.

156. Schweizer, M. and D.M. Kolb, *Electrochemical and structure studies of ethanethiol self-assembled monolayers on Ag single crystal electrodes.* Journal of Electroanalytical Chemistry, 2004. **564**: p. 85-91.

157. Buck, M., O. Dannenberger, and J.J. Wolff, *Formation of organic thin films at the liquid-solid interface studied by second harmonic spectroscopy.* Thin Solid Films, 1996. **284-285**: p. 396-399.

158. Yamada, R. and K. Uosaki, *In Situ Scanning Tunneling Microscopy Observation of the Self-Assembly Process of Alkanethiols on Gold(111) in Solution.* Langmuir, 1998. **14**(4): p. 855-861.

159. Weisshaar, D.E., B.D. Lamp, and M.D. Porter, *Thermodynamically Controlled Electrochemical Formation of Thiolate Monolayers at Gold: Characterization and Comparison to Self-Assembled Analogs.* Journal of the American Chemical Society, 1992. **114**: p. 5860-5862.

160. Schönenberger, C., et al., *Domain Structure of Self-Assembled Alkanethiol Monolayers on Gold.* Journal of Physical Chemistry, 1995. **99**(10): p. 3259-3271.

161. Nuzzo, R.G., E.M. Korenic, and L.H. Dubois, *Studies of the temperature-dependent phase behavior of long chain n-alkyl thiol monolayers on gold.* Journal of Chemical Physics, 1990. **93**(1): p. 767-773.

162. Matsuoka, T., et al., *Inverse analysis of accelerator distribution in copper through silicon via filling.* Electrochimica Acta, 2012. **82**(0): p. 356-362.

163. Ulman, A., et al., *Concentration-Driven Surface Transition in the Wetting of Mixed Alkanethiol Monolayers on Gold.* Journal of the American Chemical Society, 1991. **113**: p. 1499-1506.

164. Whitesides, G.M. and P.E. Laibinis, *Wet Chemical Approaches to the Characterization of Organic Surfaces: Self-Assembled Monolayers, Wetting, and the Physical-Organic Chemistry of the Solid-Liquid Interface.* Langmuir, 1990. **6**(1): p. 87-96.

165. Finklea, H.O. and D.D. Hanshew, *Electron-Transfer Kinetics in Organized Thiol Monolayers with Attached Pentaammine(pyridine)ruthenium Redox Centers.* Journal of the American Chemical Society, 1992. **114**(9): p. 3173-3181.

166. Hong, H.-G. and W. Park, *Electrochemical Characteristics of Hydroquinone-Terminated Self-Assembled Monolayers on Gold.* Langmuir, 2001. **17**(8): p. 2485-2492.

167. Chidsey, C.E.D., *Free Energy and Temperature Dependence of Electron Transfer at the Metal-Electrolyte Interface.* Science, 1991. **251**: p. 919-922.

168. Nishizawa, M., T. Sunagawa, and H. Yoneyama, *Underpotential Deposition of Copper on Gold Electrodes through Self-Assembled Monolayers of Propanethiol.* Langmuir, 1997. **13**: p. 5215-5217.

169. Sondag-Huethorst, J.A.M. and L.G.J. Fokkink, *Galvanic Copper Deposition on Thiol-Modified Gold Electrodes.* Langmuir, 1995. **11**(12): p. 4823-4831.

170. Finklea, H.O., D.A. Snider, and J. Fedyk, *Passivation of Pinholes in Octadecanethiol Monolayers on Gold Electrodes by Electrochemical Polymerization of Phenol.* Langmuir, 1990. **6**: p. 371-376.

171. Iwami, Y., et al., *Determination of the potential of zero charge of Au(111) electrodes modified with thiol self-assembled monolayers using a potential-controlled sessile drop method.* Journal of Electroanalytical Chemistry, 2004. **564**: p. 77-83.

172. Finklea, H.O., et al., *Effect of the Metal on Electron Transfer across Self-Assembled Monolayers.* Journal of Physical Chemistry B, 2001. **105**(15): p. 3088-3092.

173. Helmholtz, H.L.F.v., Ann. Physik., 1853. **89**: p. 211.

174. Helmholtz, H.L.F.v., Ann. Physik., 1879. **7**: p. 337.

175. Gouy, G., J Phys Radium, 1910. **9**: p. 457.

176. Gouy, G., Compt Rend, 1910. **149**: p. 654.

177. Chapman, D.L., Phil Mag, 1913. **25**: p. 475.

178. Stern, O., Z Elektrochem, 1924. **30**: p. 508.

179. Sondag-Huethorst, J.A.M. and L.G.J. Fokkink, *Electrical double layers on thiol-modified polycrystalline gold electrodes.* Journal of Electroanalytical Chemistry, 1994. **367**: p. 49-57.

180. Rampi, M.A., O.J.A. Schueller, and G.M. Whitesides, *Alkanethiol self-assembled monolayers as the dielectric of capacitors with nanoscale thickness.* Applied Physics Letters, 1998. **72**(14): p. 1781-1783.

181. Janek, R.P., W.R. Fawcett, and A. Ulman, *Impedance Spectroscopy of Self-Assembled Monolayers on Au(111): Evidence for Complex Double Layer Structure in Aqueous* $NaClO_4$ *at the Potential of Zero Charge.* Journal of Physical Chemistry B, 1997. **101**: p. 8550-8558.

182. Protsailo, L.V. and W.R. Fawcett, *Studies of electron transfer through self-assembled monolayers using impedance spectroscopy.* Electrochimica Acta, 2000. **45**(21): p. 3497-3505.

183. Diao, P., et al., *Studies of structural disorder of self-assembled thiol monolayers on gold by cyclic voltammetry and ac impedance.* Journal of Electroanalytical Chemistry, 1999. **464**: p. 61-67.

184. Finklea, H.O., S. Avery, and M. Lynch, *Blocking Oriented Monolayers of Alkyl Mercaptans on Gold Electrodes.* Langmuir, 1987. **3**: p. 409-413.

185. Love, J.C., et al., *Self-Assembled Monolayers of Thiolates on Metals as a Form of Nanotechnology.* Chemical Reviews, 2005. **105**(4): p. 1103-1170.

186. Kondo, T., T. Sumi, and K. Uosaki, *A rotating ring-gold disk electrode study on electrochemical reductive desorption and oxidative readsorption of a self-assembled monolayer of dodecanethiol.* Journal of Electroanalytical Chemistry, 2002. **538**: p. 59-63.

187. Widrig, C.A., C. Chung, and M.D. Porter, *The electrochemical desorption of n-alkanethiol monolayers from polycrystalline Au and Ag electrodes.* Journal of Electroanalytical Chemistry, 1991. **310**: p. 335-359.

188. Wong, S.-S. and M.D. Porter, *Origin of the multiple voltammetric desorption waves of long-chain alkanethiolate monolayers chemisorbed on annealed gold electrodes.* Journal of Electroanalytical Chemistry, 2000. **485**: p. 135-143.

189. Walczak, M.M., et al., *Electrochemical and X-ray photoelectron spectroscopic evidence for differences in the binding sites of alkanethiolate monolayers chemisorbed at gold.* Journal of Electroanalytical Chemistry, 1995. **396**: p. 103-114.

190. Walczak, M.M., et al., *Reductive Desorption of Alkanethiolate Monolayers at Gold: A Measure of Surface Coverage.* Langmuir, 1991. **7**: p. 2687-2693.

191. Kawaguchi, T., et al., *Electrochemical Quartz Crystal Microbalance Investigation of the Reductive Desorption of Self-Assmbled Monolayers of Alkanethiols and Mercaptoalkanoic Acids on Au.* Langmuir, 2000. **16**(25): p. 9830-9840.

192. Kreevoy, M.M., et al., *Inductive Effects on the Acid Dissociation Constants of Mercaptans1.* Journal of the American Chemical Society, 1960. **82**(18): p. 4899-4902.

193. Schneewiess, M.A., et al., *Electrolytic metal deposition onto chemically modified electrodes.* Applied Physics A, 1999. **69**: p. 537-551.

194. Eliadis, E.D., et al., *Copper Deposition in the Presence of Surface-Confined Additives.* Journal of the Electrochemical Society, 1997. **144**(1): p. 96-105.

195. Cavalleri, O., S.E. Gilbert, and K. Kern, *Electrochemical Cu deposition on thiol covered Au(111) surfaces.* Surface Science, 1997. **377–379**(0): p. 931-936.

196. Ohtani, M., et al., *Preparation of a microelectrode array using desorption of a self-assembled monolayer of hexadecylthiolate on a gold electrode in cyanide solution.* Journal of Electroanalytical Chemistry, 1997. **429**: p. 75-80.

197. Lühn, O., et al. *Reducing the electrodeposition time for filling microvias with copper for 3D technology*. in *Electronic Components and Technology Conference, 2008. ECTC 2008. 58th*. 2008.

198. Bertocci, U., *Applications of a Low Noise Potentiostat in Electrochemical Measurements.* Journal of the Electrochemical Society, 1980. **127**(9): p. 1931-1934.

199. Long, J.G., P.C. Searson, and P.M. Vereecken, *Electrochemical Characterization of Adsorption-Desorption of the Cuprous-Suppressor-Chloride Complex during Electrodeposition of Copper.* Journal of The Electrochemical Society, 2006. **153**(4): p. C258-C264.

200. Tsai, W.-C., C.-C. Wan, and Y.-Y. Wang, *Pulsed Current and Potential Response of Acid Copper System with Additives and the Double Layer Effect.* Journal of the Electrochemical Society, 2002. **149**(5): p. C229-C236.

201. Gabrielli, C., et al., *Mechanism of copper deposition in a sulphate bath containing chlorides.* Journal of Electroanalytical Chemistry, 2004. **572**(2): p. 367-375.

202. Bongenaar, C.P.M., et al., *On the selection of the most probable mechanism of the Cd(II) reduction at mercury from 1 M KF solution.* Journal of Electroanalytical Chemistry, 1980. **111**: p. 139-153.

203. Sluyters-Rehbach, M. and J.H. Sluyters, *Chapter 4*, in *Comprehensive Treatise of Electrochemistry, Volume 9*, E. Yeager, et al., Editors. 1984, Springer: New York.

204. Hurtado, M.R.F., P.T.A. Sumodjo, and A.V. Benedetti, *Electrochemical studies with a Cu-5wt.%Ni alloy in 0.5 M* H_2SO_4*.* Electrochimica Acta, 2003. **48**(19): p. 2791-2798.

205. Gabrielli, C., et al., *A Model for Copper Deposition in the Damascene Process: Application to the Aging of the Deposition Bath.* Journal of The Electrochemical Society, 2007. **154**(1): p. D13-D20.

206. Blajiev, O. and A. Hubin, *Inhibition of copper corrosion in chloride solutions by amino-mercapto-thiadiazol and methyl-mercapto-thiadiazol: an impedance spectroscopy and quantum-chemical investigation.* Electrochimica Acta, 2004. **49**: p. 2761-2770.

207. Ji, C., G. Oskam, and P.C. Searson, *Electrodeposition of Copper on Silicon from Sulfate Solution.* Journal of the Electrochemical Society, 2001. **148**(11): p. C746-C752.

208. Tantavichet, N. and M.D. Pritzker, *Low and High Frequency Pulse Current Plating of Copper onto a Rotating Disk Electrode.* Journal of the Electrochemical Society, 2002. **149**(5): p. C289-C299.

209. Diard, J.P. and C. Montella, *Unusual concentration impedance for catalytic copper deposition.* Journal of Electroanalytical Chemistry, 2006. **590**(2): p. 126-137.

210. Drews, T.O., J.C. Ganley, and R.C. Alkire, *Evolution of Surface Roughness during Copper Electrodeposition in the Presence of Additives.* Journal of the Electrochemical Society, 2003. **150**(5): p. C325-C334.

211. Mansfeld, F., et al., *Minimization of High-Frequency Phase Shifts in Impedance Measurements.* Journal of The Electrochemical Society, 1988. **135**(4): p. 906-907.

212. Healy, J.P., D. Pletcher, and M. Goodenough, *The chemistry of the additives in an acid copper electroplating bath Part I. Polyethylene glycol and chloride ion.* Journal of Electroanalytical Chemistry, 1992. **338**: p. 155-165.

213. Kelly, J.J. and A.C. West, *Copper Deposition in the Presence of Polyethylene Glycol II. Electrochemical Impedance Spectroscopy.* Journal of the Electrochemical Society, 1998. **145**(10): p. 3477-3481.

214. Moffat, T.P., et al., *Superconformal film growth: Mechanism and quantification.* IBM Journal of Research and Development, 2005. **49**(1): p. 19-36.

215. Pauwels, L., et al., *Key issues for reproducible impedance measurements and their well-founded error analysis in a silver electrodeposition system.* Electrochimica Acta, 2002. **47**: p. 2135-2141.

216. Krzewska, S., *Impedance investigation of the mechanism of copper electrodeposition from acidic perchlorate electrolyte.* Electrochimica Acta, 1997. **42**(23-24): p. 3531-3540.

217. Armstrong, R.D. and R.E. Firman, *Impedance plane display of a reaction with a solution soluble intermediate.* Journal of Electroanalytical Chemistry, 1973. **45**: p. 3-10.

218. Slaiman, Q.J.M. and W.J. Lorenz, *Investigations of the kinetics of Cu/Cu^{2+} electrode using the galvanostatic double pulse method.* Electrochimica Acta, 1974. **19**(12): p. 791-798.

219. Mattsson, E. and J.O.M. Bockris, *Galvanostatic studies of the kinetics of deposition and dissolution in the copper + copper sulphate system.* Transactions of the Faraday Society, 1959. **55**: p. 1586-1601.

220. Survila, A., Z. Mockus, and S. Kanapeckaite, *Effect of halides on adsorption properties of polyether laprol 2402 C on copper and tin electrodes.* Journal of Electroanalytical Chemistry, 2003. **552**: p. 97-103.

221. Survila, A., et al., *Codeposition of copper and tin from acid sulphate solutions containing polyether sintanol DS-10 and micromolar amounts of halides.* Electrochimica Acta, 2007. **52**(9): p. 3067-3074.

222. Gabrielli, C., et al., *A model for copper deposition in the damascene process.* Electrochimica Acta, 2006. **51**(8–9): p. 1462-1472.

223. Cachet, C., et al., *EIS investigation of zinc dissolution in aerated sulphate medium. Part II: zinc coatings.* Electrochimica Acta, 2002. **47**: p. 3409-3422.

224. Cachet, C., et al., *EIS investigation of zinc dissolution in aerated sulfate medium. Part I: bulk zinc.* Electrochimica Acta, 2001. **47**(3): p. 509-518.

225. Cachet, C. and R. Wiart, *The kinetics of zinc dissolution in chloride electrolytes: impedance measurements and electrode morphology.* Journal of Electroanalytical Chemistry, 1980. **111**: p. 235-246.

226. Betova, I., et al., *Mechanism of transpassive dissolution of nickel-based alloys studied by impedance spectroscopy and rotating ring-disc voltammetry.* Electrochimica Acta, 2002. **47**(13–14): p. 2093-2107.

227. Pilla, A.A. and G.S. Margules, *Dynamic Interfacial Electrochemical Phenomena at Living Cell Membranes: Application to the Toad Urinary Bladder Membrane System.* Journal of The Electrochemical Society, 1977. **124**(11): p. 1697-1706.

228. Subbaiah, T. and S.C. Das, *Physico-chemical properties of copper electrolytes.* Metallurgical Transactions B, 1989. **20**(3): p. 375-380.

229. Deligianni, H., et al., *Electrochemical Processing in ULSI Fabrication and Semiconductor/Metal Deposition II*, in *The Electrochemical Society Proceedings Series*. 1999, The Electrochemical Society: Pennington, NJ. p. 83.

230. Fang, R., et al., *Electrochemical Processing in ULSI and MEMS*, in *The Electrochemical Society Proceedings Series*. 2004, The Electrochemical Society: Pennington, NJ. p. 193.

231. Gallaway, J.W. and A.C. West, *The effect of acid on superconformal filling in 100 nm trenches.* Journal of Vacuum Science & Technology B, 2009. **27**(5): p. 2200-2205.

232. Atanasova, T.A., et al., *Ultra-Low Copper Baths for Sub-35nm Copper Interconnects.* ECS Transactions, 2012. **41**(35): p. 83-97.

233. Debye, P. and E. Hückel, *ON THE THEORY OF ELECTROLYTES. I. FREEZING POINT DEPRESSION AND RELATED PHENOMENA.* Physikalische Zeitschrift, 1923. **29**(9): p. 185-206.

234. Galceran, J., et al., *AGNES: a new electroanalytical technique for measuring free metal ion concentration.* Journal of Electroanalytical Chemistry, 2004. **566**: p. 95-109.

235. Atanasova, T.A., K. Strubbe, and P.M. Vereecken, *Electrochemical Determination of the Cupric Ion Activity in Aqueous Acidic Cupric Sulfate Electrolytes.* Journal of The Electrochemical Society, 2013. **160**(2): p. D60-D65.

236. West, A.C., C.-C. Cheng, and B.C. Baker, *Pulse Reverse Copper Electrodeposition in High Aspect Ratio Trenches and Vias.* Journal of the Electrochemical Society, 1998. **145**(9): p. 3070-3074.

237. Halsey, T.C., *Stability of a flat interface in electrodeposition without mixing.* Physical Review A, 1987. **36**(7): p. 3512-3514.

238. Stoychev, D., et al., *Effect of the structure of aromatic disulphides on some physico-mechanical properties of electrodeposited copper coatings.* Journal of Applied Electrochemistry, 1992. **22**: p. 987-990.

239. Kelly, J.J., C. Tian, and A.C. West, *Leveling and Microstructural Effects of Additives for Copper Electrodeposition.* Journal of the Electrochemical Society, 1999. **146**(7): p. 2540-2545.

240. Kondo, K., et al., *Copper damascene electrodeposition and additives.* Journal of Electroanalytical Chemistry, 2003. **559**: p. 137-142.

241. Luo, Y.-R., *Comprehensive Handbook of Chemical Bond Energies*. 2007, Boca Raton, FL: CRC Press.

242. Bockris, J.O.M. and M. Enyo, *Mechanism of Electrodeposition and Dissolution Processes of Copper in Aqueous Solutions.* Transactions of the Faraday Society, 1961. **57**: p. 1187-1202.

243. Bockris, J.O.M. and H. Kita, *The dependence of Charge Transfer and Surface Diffusion Rates on the Structure and Stability of an Electrode Surface: Copper.* Journal of the Electrochemical Society, 1962. **109**(10): p. 928-939.

244. Healy, J.P., D. Pletcher, and M. Goodenough, *The chemistry of the additives in an acid copper electroplating bath Part III. The mechanism of brightening by 4,5-dithiaoctane-1,8-disulphonic acid.* Journal of Electroanalytical Chemistry, 1992. **338**: p. 179-187.

245. Albery, W.J. and M.L. Hitchman, *Ring-disc Electrodes*. 1971, Oxford: Oxford University Press. 175.

246. Pell, W.G., A. Zolfaghari, and B.E. Conway, *Capacitance of the double-layer at polycrystalline Pt electrodes bearing a surface-oxide film.* Journal of Electroanalytical Chemistry, 2002. **532**: p. 13-23.

247. Wu, Z.-L., Z.-H. Zang, and S.-L. Yau, *Electrodeposition of Copper at Well-Defined Pt(111) and Rh(111) Electrodes in Sulfuric Acid Solutions: Studying with In Situ Scanning Tunneling Microscopy.* Langmuir, 2000. **16**(7): p. 3522-3528.

248. Frank, A. and A.J. Bard, *The Decomposition of the Sulfonate Additive Sulfopropyl Sulfonate in Acid Copper Electroplating Chemistries.* Journal of the Electrochemical Society, 2003. **150**(4): p. C244-C250.

249. Choe, S., et al., *Degradation of Bis(3-sulfopropyl) Disulfide and Its Influence on Copper Electrodeposition for Feature Filling.* Journal of The Electrochemical Society, 2013. **160**(12): p. D3179-D3185.

250. Gabrielli, C., et al., *Electrochemical Impedance Spectroscopy Investigation of Bath Aging in Damascene Process Chemistries.* Electrochemical and Solid-State Letters, 2004. **7**(3): p. C31-C34.

251. Boukamp, B.A., *A nonlinear least squares fit procedure for analysis of immittance data of electrochemical systems.* Solid State Ionics, 1986. **20**: p. 31-44.

252. Huang, Q., J. Liu, and B. Baker-O'Neal, *An Electrochemical Method of Suppressor Screening for Cu Plating in Sub-100 nm Lines.* Journal of The Electrochemical Society, 2014. **161**(5): p. D207-D213.

Curriculum Vitae

Born in Honolulu, Hawai'i in 1976, the author attended Holy Nativity, Iolani, Western Middle and Greenwich High Schools, graduating in the spring of 1994. He matriculated as an undergraduate at Johns Hopkins University that fall, where he was awarded a Bachelor of Science in Materials Science and Engineering and a Bachelor of Arts in Political Science, graduating with both Departmental and University Honors. From then until 2005, he worked in the Searson Lab at Johns Hopkins, with internships at IBM's T.J. Watson Research Center in Yorktown Heights, New York in the summers of 2002 and 2003. In October of 2005, he left Johns Hopkins to attend the United States Marine Corps' Officer Candidate School in Quantico, Virginia, being commissioned as a Second Lieutenant in December of that year. In October of 2006, he entered the Fleet Marine Force as an officer in the 1st Marine Division. Over the next seven years, he completed 6 combat deployments to Iraq, Afghanistan and other Middle East countries. He is a graduate of Expeditionary Warfare School and Command and Staff College. He left active duty as a Captain in the fall of 2013, and matriculated at the University of Oxford's Saïd Business School, graduating with Distinction the following fall with a Masters in Business Administration. He is currently a Fellow at the University of Oxford, working on technology transfer at Isis Innovation and helping to build a university wide innovation ecosystem.